HOT WORKABILITY OF IRON ALUMINUM INTERMETALLICS IN COMPARISON TO FERRITIC STEELS

ANI SHEN

A Thesis in

The Department of Mechanical and Industrial Engineering

Presented in Partial Fulfillment of the Requirements

For the Degree of Master of Applied Science (Mechanical Engineering)

at

Concordia University

Montreal, Quebec, Canada

March 2008

Your file Votre référence
ISBN: 978-0-494-40923-7
Our file Notre référence
ISBN: 978-0-494-40923-7

ABSTRACT

Hot Workability of Iron Aluminum Intermetallics in Comparison to Ferritic Steels

Ani Shen

In this project, torsion tests on hot-rolled and annealed Fe_3Al (Fe-15.5Al-5.8Cr-1.0Nb-0.05C) were carried out over the ranges 750-950°C and 0.01~1s^{-1}. The experimental results showed that when peak stress σ_P>90MPa (LogZ>16s^{-1}, Z: temperature-compensated strain rate, $Z = \dot{\varepsilon}\exp(Q_{HW}/RT)$, R: universal gas constant; Q_{HW} :activation energy; T: absolute temperature), specimens cracked at randomly low strains. Optical microscopy exhibited original elongated grains and many grain boundary cracks associated with segregation. With $\sigma_P \leq$40MPa (LogZ$\leq$16s^{-1}), specimens deformed with low random σ_P but considerably high fracture strains; slowly propagating cracks may explain the reduced flow stress. Optical microscopy showed both elongated grains and equiaxed subgrains with some indications of geometric dynamic recrystallization (gDRX) and of static recrystallization (SRX). Compression tests gave higher stress with little effect of the preexisting cracks. Q_{HW} of current material in satisfactory torsion and compression tests is about 10% higher than previously published results.

Fe_3Al has body-centered cubic structure in the experimental range, so it was compared with ferritic steel 434C (Fe- 16.55Cr-0.96Mo-0.21Ni, wt%). Ferritic steels with approximately 3.0wt%Si are of great interest in transformer applications. Isothermal continuous deformation of Fe-2.7Si-0.06C was analyzed and compared with 434C and 409C (11.0Cr-0.01Mo-0.16Ni-0.19Ti, wt%). Multi-stage deformation of the material was investigated to determine the relative softening and relative stress reduction during the intervals between successive stages. Constitutive constants and restoration mechanism were compared between the materials.

AKNOWLEDGEMENT

I would like to attribute all my success and fulfillment in both life and research to my great parents, wonderful brother and sister-in-law as well as my smart and lovely nephew. Their love and support are always the most important source of my courage of going forward.

I would like to attribute the success in my experiments and thesis writing to my supervisor Prof. Hugh J. McQueen. His huge storage of knowledge, great intelligence and ambition of perfection ground all the fulfillments of my projects. Special thanks are given to his family for their kindness.

I appreciate the generous help of Dr. Benoit Voyzelle from CANMET, Ottawa on the project of Fe_3Al; I appreciate the wonderful cooperation of Prof. Mohieldeen Abdel-Rahman from Minia University, Egypt for his providing experimental data of Fe-2.7Si. The research was funded by grant from the Natural Science and Engineering Council of Canada and assistance also came from Faculty Program in Support of Thesis of Concordia University.

Special thanks are also given to Rev. Linda Borden Taylor and her family for their consistent love, care and generosity; to those who care and love me inside and outside St. James the Apostle, Montreal.

TABLE OF CONTENTS

LIST OF FIGURES

LIST OF TABLES

LIST OF SYMBOLS

a	material constant
a'	material constant
A	a constant
b	material constant
b'	material constant
d_S	equilibrium subgrain size (μm)
D_O	original grain size (μm)
D_s	grain size of DRX grains at steady state (μm)
DRV	dynamic recovery
DRX	dynamic recrystallization
FS	fractional softening
G	average grain growth rate during the progress of recrystallization
G'	material constant
G''	material constant
GB	grain boundary
gDRX	geometric dynamic recrystallization
GG	grain growth
H	material constant
H'	material constant
i	pass number in multi-stage tests
MFS	mean flow stress in a pass (MPa)

n	stress exponent
n'	strain-hardening coefficient
P	a constant usually close to unity
q	a constant usually close to 0.8
Q_{HW}	activation energy of hot working (kJ/mol)
r_{gage}	radius of the gage section of torsion specimens (m)
R	universal gas constant (8.314J/mol-K)
RS	relative softening
RRS	relative reduction of stress
SFE	stacking fault energy
S_i	retained strain energy at the end of pass i
$S_{O(i+1)}$	residual hardening at the start of pass $i+1$
SRV	static recovery
SRX	static recrystallization
t	time of holding (second)
t_i	interval between two neighboring passes (second)
T	temperature (°C)
T_i	temperature in pass i (°C)
T_{nr}	temperature below which SRX stops to be complete in multi-stage tests (°C)
T_M	melting temperature (K)
T_{SRV}	the temperature below which SRX stops and only SRV occurs during the intervals (°C)

TEM	transmission electron microscopy
X_S	fraction of SRX
Z	Zener-Holloman parameter (s^{-1})
α	stress multiplier taken as $0.017MPa^{-1}$
ε	strain
ε_f	fracture strain
ε_i	strain in pass i
ε_S	critical strain to steady state
$\dot{\varepsilon}$	strain rate (s^{-1})
$\dot{\varepsilon}_i$	strain rate in pass i (s^{-1})
θ	strain hardening rate
ρ_d	dislocation density
σ	stress (MPa)
σ_{mi}	maximum stress of pass i (MPa)
σ_P	peak stress (MPa)
σ_{Pi}	peak stress in isothermal-continuous deformation under T_i and $\dot{\varepsilon}_i$ (MPa)
σ_{ri}	reloading stress of pass i (MPa)
σ_S	steady-state stress (MPa)
σ_{yi}	actual yielding stresses at T_i (MPa)
σ'_{yi}	yielding stress of the recrystallized material at T_i (MPa)

CHAPTER ONE

INTRODUCTION

1.1 Objective of hot working

Hot working refers to mechanical processes during which metal materials undergo substantial shape change at 0.5~0.9 T_M (melting temperature). The objective is to realize substantial shape change, therefore, it is important to decrease the stress and increase the ductility of the components during straining [1, 2].

1.2 Fe_3Al and Silicon steels

As potential candidates in hot structural applications, iron aluminum intermetallics exhibit advantages such as low cost, availability of raw materials, conservation of strategic materials such as chromium, high strength-to-weight ratio compared with steels and remarkable oxidation, corrosion and sulfidation resistance. They are used to substitute for commercial stainless steels and Ni-base superalloys. Their potential applications include wear/erosion/corrosion-resistant coatings, heat-exchanger piping, industrial valve components, furnace elements and components, steam turbine parts, automotive exhaust systems, components in sulfidizing environments such as molten salts and hot-gas cleanup filters [2, 3].

In the past several decades, Fe_3Al has been extensively tested in tension and compression tests. In this project, torsion and compression tests on hot-rolled and annealed Fe_3Al were carried out over the range of 750-950°C with strain rate either 0.01, 0.1 or $1s^{-1}$, the mechanical properties and microstructures were analyzed and compared to those from compression tests of previously published results [4, 5].

Moreover, Fe_3Al shows similar crystal structure to those of ferritic stainless steels such as 434C (Fe-16.55Cr-0.96Mo-0.21Ni) [6] over the experimental temperature range. Consequently, the mechanical properties and microstructure of Fe_3Al were also compared to those of 434C.

Silicon steels are mainly used in transformers, power generators and motors, those with well-oriented grains in transformers and those with non-oriented grains in power generators and motors. Steels with 3%Si are mainly used as cores in transformers, and their ferromagnetic and electrical properties have been extensively studied [7, 8]. In this project, the hot torsion properties of Fe-2.7Si-0.06C [9] in isothermal-continuous tests are analyzed and compared to previously published results [10, 11, 12]. Moreover, this steel is also a ferritic steel, therefore, it is compared to 434C and 409C (11.0Cr-0.01Mo-0.16Ni-0.19Ti, wt%, ferritic stainless steel) [13]. Multi-stage experiments with different pass strain, pass interval were carried out when temperature declined but strain rate kept constant. The effects of these parameters on static recrystallization and softening are analyzed. Fractional softening (FS) has been investigated with ferritic and austentic stainless steels as well as Al alloys to analyze the effect of dynamic and static restoration on multi-stage deformation. However, in this project, fractional softening is difficult to calculate because of the solute effect on yielding stress, therefore, relative softening (RS) and relative stress reduction (RRS) are calculated.

CHAPTER TWO

REVIEW OF PREVIOUS WORK

2.1 Characteristics of hot working

An industrial process usually consists of preheating, several different stages of deformation and the intervals between them. High productivity is expected with low cost. Table 2.1 summarizes the characteristics of hot working [1].

2.2 Flow curves and restoration mechanisms in hot working

Restoration, i.e., softening compared to cold working at 20°C, occurs dynamically during straining but statically after straining. Metals with high stacking fault energy (SFE) such as ferritic steels and alloys, Al and alloys have a strong tendency to dynamic recovery (DRV), but those with low SFE such as Ni, Ni-base superalloys, austenitic steels and alloys, Cu, bronze and brass have a strong tendency to dynamic recrystallization (DRX). After deformation, static restoration occurs including recovery (SRV) and recrystallization (SRX) [14, 15, 16].

2.2.1 Dynamic recovery (DRV)

In hot working, DRV proceeds through cross-slip of screw dislocations below $0.5\,T_M$ but also climb of edge dislocations from vacancy migration above $0.5\,T_M$.

2.2.1.1 Flow curve and microstructural development

Fig.2.1 shows schematic flow curves of high-SFE metals and alloys when deformed at constant $\dot{\varepsilon}$ and temperature T respectively. For one curve, during the initial strain-hardening

Table 2.1 Characteristics of hot working [1]

Objective	Stress σ, temperature T, grain size D_s	Minimize preheating: homogenize, control D_O; limit σ within force and power limits of equipment; protect tooling, reduce energy;
	Strain rate ε̇ and strain ε	Increase forming rate and productivity;
	Reduction	Increase reduction, reducing stages;
	Product quality	Maintain surface, shape, dimensions tolerance;
		Avoid defect formation, reducing scrap
Deformation	ε̇	10^{-3}--10^{3} s^{-1}
	T	0.5-0.9 T_M
	ε	Substantial shape change
Operation	T	Non-uniform: decreasing due to cold tooling, increasing by deformation heating
	ε̇	Varies non-uniformly in each stage, changes from stage to stage
	σ	Non-uniform due to tool geometry, blank shape and friction
Microstructure	Preheating	homogenize as-cast grain structure, segregation; dissolves precipitates, control grain size
	Grains and substructure	Substructure strengthens the product; Recrystallization refines grains and lowers strength but increases ductility;
	Precipitates	Coarsen or dissolve repetitively;
	Defects	Second phase breaks up and disperses; Rigid particles cause voids and failure; Surface cast defects eliminated by scarfing Internal voids closed by compressive stress
Testing techniques	Tension	Poor because of necking
	Compression	Strain limited by friction
	Torsion	High strain, multistage simulation
	Lab rolling, extrusion	Not easily scaled to σ, ε ranges in industry; Multistage tests to simulate processing

phase, the flow stress σ increases with a diminishing rate, indicating a continuously decreasing strain hardening rate θ $(d\sigma/d\varepsilon)$ [14, 15, 16]. Dislocations accumulate into irregular tangles with a decreasing rate as the rate of annihilation increases. θ decreases linearly with rising σ but then slows down to a second linear relationship. The dislocations

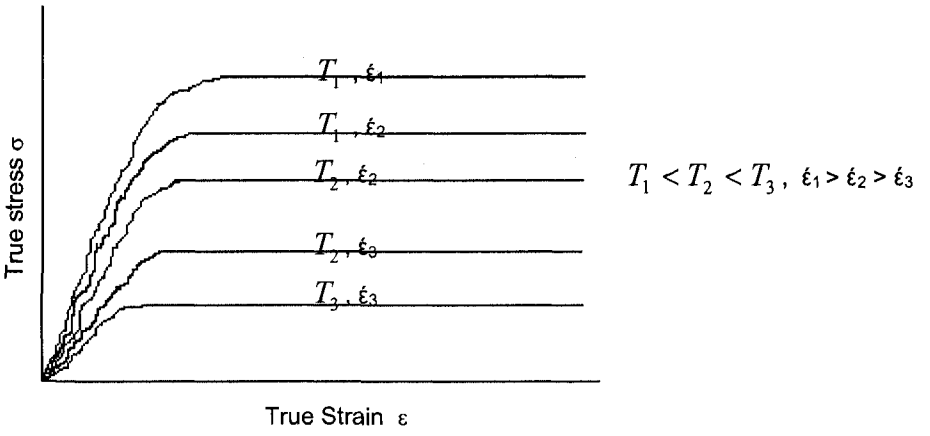

Fig. 2.1 Schematic flow curve in hot working for high-SFE metals and alloys

combine with and annihilate each other as well as rearrange, and the tangles convert into polygonized subboundaries within the elongating grains. At steady state, θ approaches zero because the rate of dislocation generation is equal to that of annihilation. During steady state, the subboundaries keep migrating, and those with less dense arrays disintegrate; they can finally rearrange into more stable equaxied subgrains that are maintained throughout the steady state. The steady-state stress σ_S, equilibrium subgrain size d_S and dislocation density ρ_d remain constant throughout the whole stage [14, 15, 16].

2.2.1.2 Constitutive equations

As shown in Figure 2.1, when deformation T rises or $\dot{\varepsilon}$ decreases, σ_S decreases and the critical strain ε_S to steady state decreases. The Zener-Holloman parameter, a temperature-compensated strain rate Z correlates the effect of $\dot{\varepsilon}$ and T on deformation and σ_S:

$$Z = \dot{\varepsilon} \exp(Q_{HW} / RT) = A(\sinh \alpha\sigma_s)^n \qquad (2.1)$$

Here, Q_{HW} is activation energy, R is gas constant, A is a constant, α is stress multiplier taken as 0.017MPa^{-1} in this project, n is stress exponent.

The steady-state subgrain size depends on the deformation condition and is related to steady-state stress [14, 15, 16]:

$$d_S^{-1} = G'' + H \log Z \qquad (2.2)$$

$$\sigma_S = a + b d_S^{-P} \qquad (2.3)$$

Here, a, b, G'' and H are material constants, P is a constant usually close to unity.

When Z is decreased, or in other words, T rises or $\dot{\varepsilon}$ decreases, the steady-state subgrains become larger and more perfect. Fig. 2.2 exhibits the subgrain development inside one grain from the start of deformation to steady-state during DRV hot working [14, 15]:

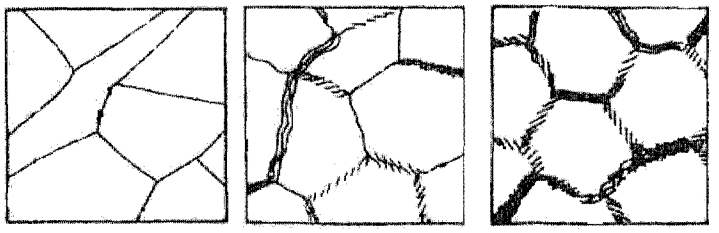

a b c

Fig.2. 2 DRV in hot working: a) undeformed, individual dislocations; b) ε=0.1, subbondaries appear; c) $\varepsilon > 0.5$, subgrains form, maintaining size and equiaxed character during steady state[14, 15].

2.2.1.3 Ductility

In hot working, fracture is generally caused by the linking of fissures known as W cracks originating from differential sliding of grain boundaries (GBs) due to the orientation of the shear stresses at the triple junctions. DRV generally improves the ductility by softening the lattice that accommodates the nonuniform GB sliding at the triple junctions, relieving stress concentrations. In solid solutions, solutes may segregate to the dislocations, slowing down the cross-slip and climb of dislocations so that DRV is retarded. Second phase particles

also pin the subgrain boundaries, decreasing the subgrain size and increasing its stability thus retarding DRV, and ductility deceases [14].

2.2.2 Discontinuous dynamic recrystallization (DRX)

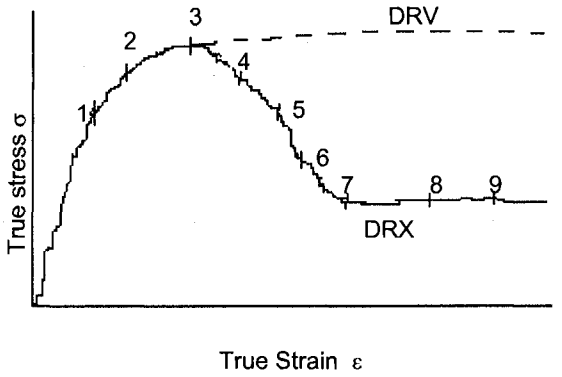

Fig. 2.3 Schematic flow curve in hot working for low-SFE metals and alloys

Fig.2.3 is a schematic flow curve for low-SFE metals and alloys such as Cu, Ni, Brass and austenitic steels. Dislocations in these materials cannot cross-slip or climb easily so that DRV is substantially retarded. The dislocation density increases to such a degree that high-angle GBs form and DRX starts at point 2. New strain-free grains nucleate along the original GBs, and they form necklaces and grow inward. In the meanwhile, dislocation density keeps increasing and reaches a peak at point 3, and approximately 35% of the total recrystallization is accomplished. After the peak, DRX continues and proceeds rapidly designated as points 4, 5 and 6, causing softening until 100% of recrystallization is achieved at point 7. The old grains are completely consumed, and the new grains distribute uniformly all over the material with time or strain. A steady state appears and is maintained at points 8 and 9. These new grains are deformed again, and low-angle boundaries migrate inside them to form a dynamically recovered low-energy substructure, which continuously renews; the renewed structure gives rise to the

additional DRX. A DRX grain stops growing when substructure is fully developed inside the new grains [14, 15]. The grain size and flow stress at steady state are measured according to equations 2.4 and 2.5:

$$\sigma_S = a' + b' D_S^{-q} \qquad (2.4)$$

$$D_S^{-1} = G' + H' \log Z \qquad (2.5)$$

Here, σ_S is the stress at steady state, a', b', G' and H' are material constants, q is a constant whose value is usually close to 0.8, D_S is the diameter of the DRX grains at steady state. The subgrain size is still defined by equations 2.2 [14].

In alloys, solutes segregate at the GBs and decrease their mobility so that DRX is retarded. Second phase particles have different effects on DRX according to their sizes, amounts and distribution. A low amount of small particles all over the grains pin subgrain boundaries and retard DRX moderately. A high amount of small to medium particles retard DRX substantially by pinning GBs. Big hard particles generally increase dislocation density greatly near them and create the nuclei of DRX [14, 15, 16].

2.2.3 Geometric DRX (gDRX)

Geometric DRX is reported to occur in Al, Al-Mg alloys and some ferritic steels [14]. After straining with DRV starts, serrations begin to form in GBs at ε about 0.2 to absorb the dislocations in subgrain boundaries and balance the energy between GBs and subgrain boundaries. When straining reaches a high ε such that grains thin down to almost subgrain size $2d_S$, serrations on opposite GBs with amplitude of about d_s come into contact and pinch off the grains. The grains stop growing thinner but become shortened into several segments. Eventually, the subgrains attain 1/3 to 1/2 of the

perimeters having high misorientation, and they are now called crystallites. This process proceeding by DRV produces fine grains quite similar to those from DRX without either nucleation or increase in average subboundary misorientation; it is termed geometric DRX [14, 17].

2.2.4 Static recovery SRV and static recrystallization SRX

Static restoration occurs in annealing after cold working, in holding after hot working and in intervals between stages of multistage hot deformation. At the end of deformation, the metal contains a substructure with a stored energy. During holding, SRV occurs rapidly at first, and if the energy is below the critical energy required for SRX, only SRV occurs. If the stored energy is above the critical energy for the nucleation of SRX, SRX starts after some delay and proceeds rapidly.

2.2.4.1 Static recovery SRV

SRV occurs when the hot-worked structure is held at a high temperature. The stored energy and thermal activation drive the dislocations to annihilate with neighboring opposite dislocations; the dislocation density inside the subgrains decreases and the walls

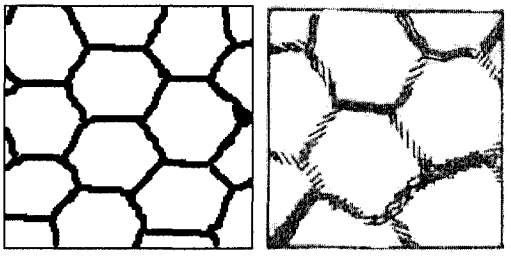

(4a) (4b)

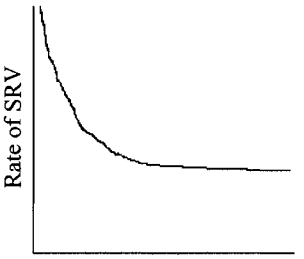

(5)

Fig.2. 4 SRV after hot working: a) quenched hot-worked substructure; b) SRV substructure [14, 15].

Fig.2.5 Relationship between SRV rate and holding time [14].

become more regular. The stored energy decreases. With increase of time, some walls disintegrate so that the subgrains grow larger. No new grains nucleate, the grain structure does not change, and the texture of the material is maintained throughout the process [14, 15, 16]. Fig.2.4 shows the process of SRV: when a hot-worked substructure is held, the equiaxed subgrains transform into larger ones. SRV proceeds quickly in metals with high SFE such as α-Fe and Al and accounts for considerable stress decrease, possibly 50% of softening. Fig.2.5 shows the relationship between SRV rate and holding time.

2.2.4.2 Static recrystallization SRX

SRX occurs when the hot-worked material is held at a high T. It proceeds by nucleation of new grains from dense dislocation regions or high-angle subboundaries through different mechanisms. In high SFE metals such as α-Fe, Al and their alloys, coalescence of clusters of subgrains gradually develop and walls inside the cluster disintegrate. The dislocations are added to the perimeter of the coalesced cells, which raises the cluster misorientation ψ. When a high-angle subgrain boundary relaxes into a GB through thermal activation of the adjacent atoms, it is able to migrate rapidly absorbing dislocations and creating a grain that grows larger. This process stops when the new grains grow so large that they impinge on each other [15, 16].

Solutes and second-phase particles in alloys also have significant effect on static restoration mechanisms. Solutes increase the dislocation density and stored energy but retard the grain boundary migration and hence SRX. This retardation in Ni-based super alloys and stainless steels makes it possible to quench-in the hot-worked substructure [16].

2.3 Review on Fe_3Al

2.3.1 Crystal structure and phase diagram

The crystal structure and equilibrium phase diagram of Fe-Al were based on the work of Bradley and Jay [18, 19, 20]. They differentiated three structures: FeAl, disordered α phase, BCC structure; B2, imperfectly ordered BCC structure; Fe_3Al, DO_3, complex cubic structure related to BCC. Bradley and Jay interpreted DO_3 as a large cubic cell made up of 8 ordinary BCC cells stacked together [20]. The crystal structures are shown as Figure 2.6 [20, 21, 22], and their change with temperature and Al content shown as Fig.2.7 [2]. When temperature decreases from 1000 to 200°C, A2, in other words, α phase changes to B2 and then to DO_3 at about 542°C. DO_3 is stable within the range of Al content 24-32wt% at room temperature [23]. McQueen and Kuczynski did a systematic study on the relationship between composition (19.9~33.6at%Al) and ordering temperature as well as Curie temperature of Fe_3Al and FeAl [24].

2.3.2 Mechanical properties

2.3.2.1 Optimum composition

Fe_3Al has industrial advantages, but its applications are significantly influenced by two major drawbacks: the low strength in high-temperature creep and poor ductility at ambient temperatures related to hydrogen embrittlement. However, both properties can be improved by an optimal Al content, addition of alloying elements and proper thermomechanical processing. The composition of most interest is Fe-28at%Al-5at%Cr (Fe-15.9wt%Al-5.5wt%Cr). Cr is added for maximum room-temperature ductility perhaps because Cr diminishes ordering [25, 26]. The carbide former Nb is generally added to form Fe_2Nb precipitates that strengthen the matrix at high temperatures [25, 26]. In this project,

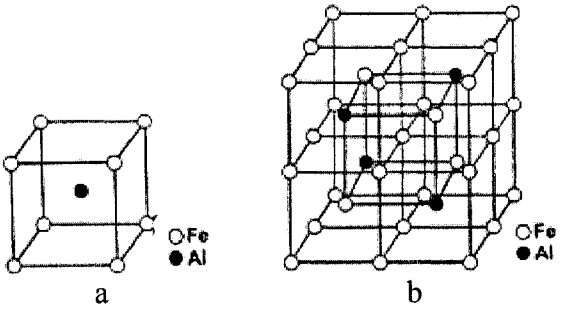

Fig. 2.6 Crystal structure: a) FeAl, BCC; b) Fe_3Al, DO_3 [21, 22, 23,].

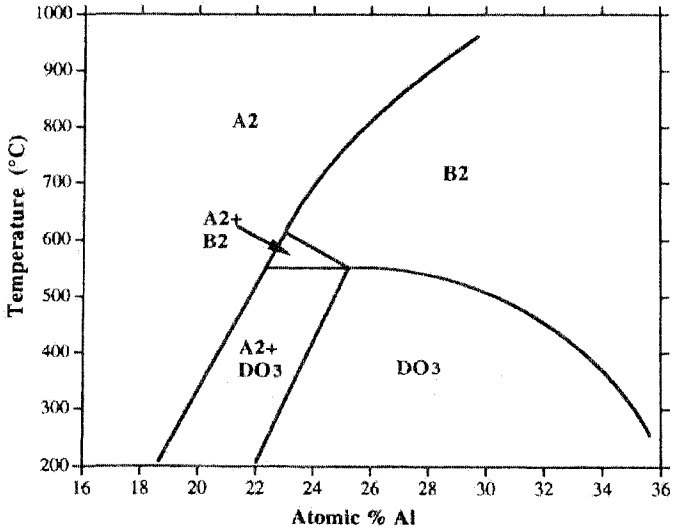

Fig. 2.7 Partial phase diagram of iron-aluminum alloys [2]

Fe_3Al (Fe-15.5Al-5.8Cr-1.0Nb-0.05C, wt%) is investigated.

2.3.2.2 The effect of Cr and Nb on mechanical properties

Nb has significant effect on tensile properties and creep resistance of Fe_3Al. In table 2.2, alloys 1 to 5 [27] were heated treated at 750°C for 1 hour before tension, alloy 6 [3] at 700°C for 1 hour. Table 2.2 and Figure 2.8 show that at room temperature, yielding stress increases but ductility and ultimate tensile stress decrease with the increase of Nb addition; At 600°C, with the increase of Nb addition, yielding stress and ultimate tensile stress decrease greatly but ductility decreases. The creep resistance increases rapidly with

the increase of Nb content shown as Figure 2.9 [27]. Compared with alloy 2 which has the same concentration of Cr and Nb, alloy 6 (also called FA-129) has lower ductility, yielding stress and ultimate tensile stress at both room temperature and 600°C, maybe due to the effect of Zr and B. Table 2.3 [28, 29] comparing the creep rupture life between binary Fe_3Al and alloys with additional alloying elements shows that the increase of Nb from 0 to 1% increases the rupture life drastically. Moreover, with the addition of Cr, Zr and B, both the rupture life and ductility increase.

Table 2.2 Tensile Properties and Creep Resistance of Alloys [3, 27]

		Creep Rupture 600°C 200 MPa		RT Tensile			600°C Tensile		
Alloy Code	Alloy Composition	Life (h)	Elong. (%)	Yield (MPa)	Ult. (MPa)	Elong. (%)	Yield (MPa)	Ult. (MPa)	Elong. (%)
1	Fe-28Al-5Cr-0.5Mo-0.05Zr-0.05B	20	62.4	520	1000	16.0	400	450	62.6
2	Fe-28Al-5Cr-0.5Mo-0.05Zr-0.05B-0.5Nb	65	51.7	545	992	14.8	457	511	53.6
3	Fe-28Al-5Cr-0.5Mo-0.05Zr-0.05B-0.6Nb	102	32.8	579	989	14.0	524	567	31.6
4	Fe-28Al-5Cr-0.5Mo-0.05Zr-0.05B-0.7Nb	130	37.5	599	900	11.3	550	590	35.2
5	Fe-28Al-2Cr-0.5Mo-0.05Zr-0.05B-0.8Nb	296	59.6	615	810	9.0	573	625	37.7
6	FA-129: Fe-28Al-5Cr-0.5Nb-0.2C			430	850	13.0	390	445	40.0

Table 2.3 Creep rupture data of Fe_3Al alloys [28, 29]

Alloy (at%)	T (°C)	Stress (MPa)	Rupture life (h)	Elongation (%)	Min. Creep rate ($\%s^{-1}$)
Fe-28Al	650	138	0.6	37.0	8.5×10^{-3}
	625	207	0.2	46.7	6.1×10^{-2}
Fe-28Al-1Nb	650	138	304.0	37.3	1.4×10^{-6}
Fe-28Al-5Cr-0.1Zr-0.05B	591	207	208	55.0	---

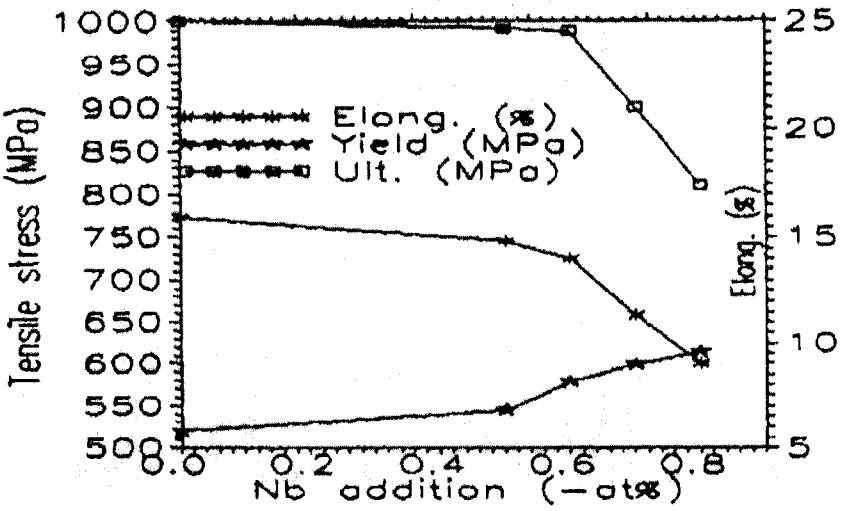

a

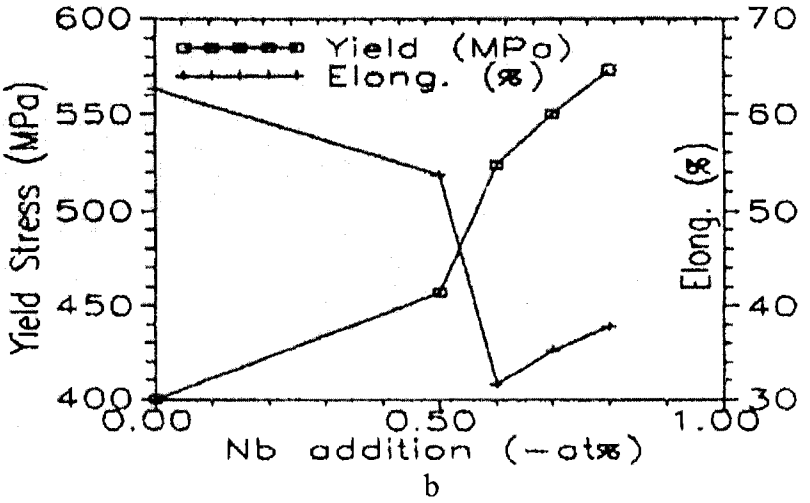

b

Fig. 2.8 Mechanical property variation with Nb content:

a) Room temperature; b) 600°C [27].

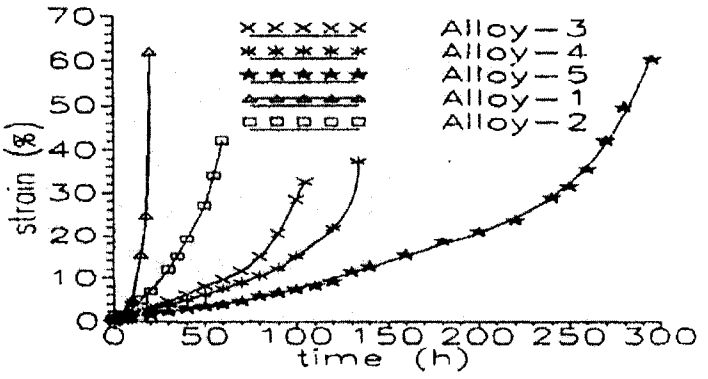

Fig. 2.9 Creep rupture life of alloys in Table 2.2 [27].

When Nb content increases to 2at%, the creep rupture life of the alloy was increased greatly shown as Figure 2.10, and its yielding stresses at both room temperature and 600°C are comparative to those of 316SS (Stainless steel, Fe-16.4Cr-12.05Ni-2.73Mo) shown in Figure 2.11, therefore, polyternary Fe_3Al such as FA-129 is considered as potential substitute for commercial 316SS [25].

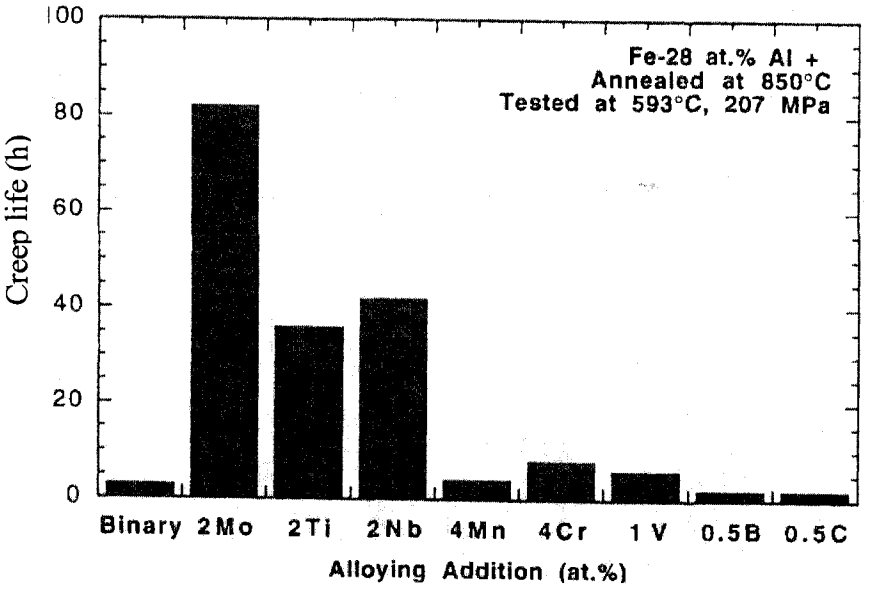

Fig. 2.10 The effect of ternary addition on the creep rupture life of Fe-28at%Al [25].

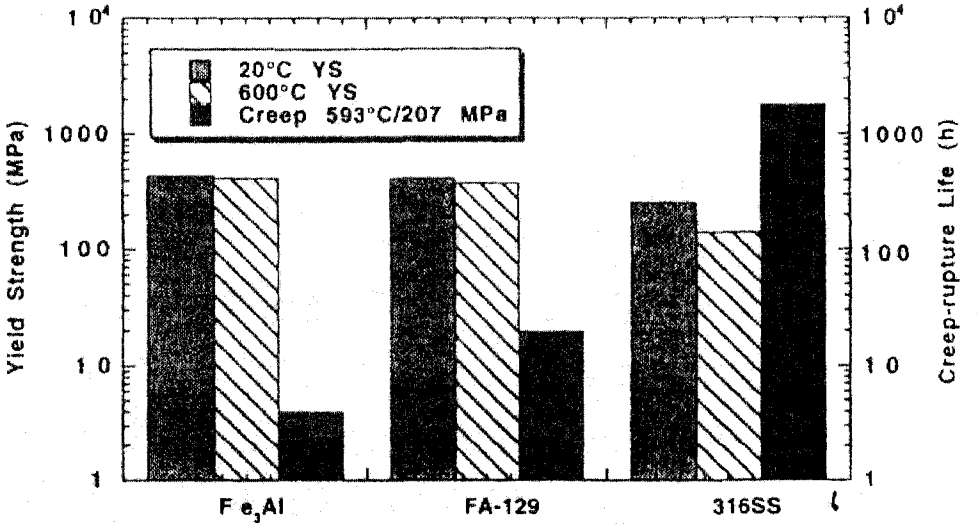

Fig. 2.11 Comparison of tensile yielding strength and creep rupture life between Fe_3Al alloys and 316SS [25].

2.3.2.3 The effect of heat treatment and quenching on mechanical properties

Control of microstructure through heat treatment can improve creep-rupture life of Fe_3Al alloys. Alloy FA-180 (Fe-28Al-5Cr-0.025Zr-0.5Nb-0.005B, similar to Alloy 2 in Table 2.2) was found to have the longest creep rupture life at 593°C and 207MPa after being heat treated at 1150°C for one hour followed by air cooling shown as Figure 2.12. Figure 2.13 shows that after a heat treatment at 1150°C for one hour, the creep rupture life is longer for oil quenching than air cooling or water quenching [25]. This is because oil creates a barrier between Al and the moisture in air so that hydrogen is absorbed, and embrittlement is reduced. Tension tests for alloy FAL (Fe-15.9Al-5.5Cr-0.01B-0.15Zr, wt%) were carried out, Sikka et al found the same effect of quenching on creep rupture life, but ductility, yielding stress and ultimate tensile stress decrease at room temperature with the increase of heat treatment temperature, because the increase of recrystallization with the increasing heat treatment temperature leads to more transverse GBs for hydrogen diffusion, which lowers mechanical properties [3].

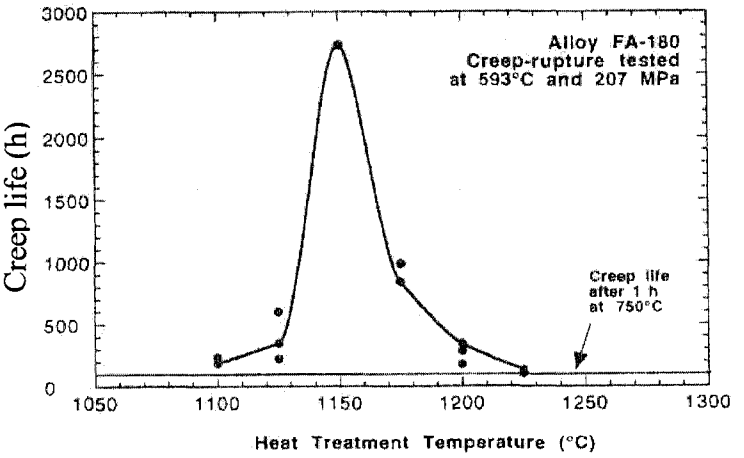

Fig. 2.12 Creep-rupture life of FA-180 versus heat treatment temperature. Specimens heat treated for 1h followed by air cooling [25]

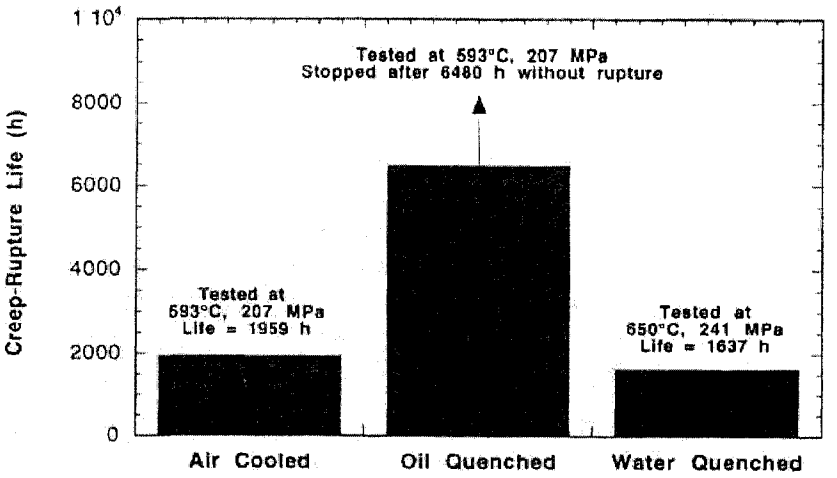

Fig. 2.13 Effect of quenching after heat treatment of 1150°C+1h on the creep-rupture life [25]

2.3.2.4 Constitutive analysis and activation energy

Constitutive analysis is valuable in defining the influence of deformation condition on flow stress of BCC metals in hot working, accurately shown as equation 2.1, 2.2 and 2.3. Such equations are also applicable to steady-state creep. Figure 2.14 exhibits the relationship between creep rate and stress for Fe-20at%Al at different T [30]. Under constant stress, the material creeps faster at higher T; the dependence of rate on T above 500°C follows an Arrhenius function. The activation energies Q_{HW} were calculated from data on several Fe-Al alloys, and the Q_{HW} value increased linearly with Al content as shown in Figure 2.15 [30] indicating that the dislocation motion was progressively retarded with the increase of Al content, and the materials required longer time for restoration. From the linear relationship, the Q_{HW} value for Fe-28at%Al (approximately Fe-16.5wt%Al) is 93.5kcal/mol or 379kJ/mol. Voyzelle carried out constitutive analysis on Fe_3Al (Fe-15.5Al-5.8Cr-1.0Nb-0.05C, wt%) and provided the Q_{HW} values of similar materials as shown in Table 2.4 [4, 5]. Unfortunately, he adopted different values of α for different materials, which changes the Q_{HW} value for a given composition and makes it difficult to compare the influence of

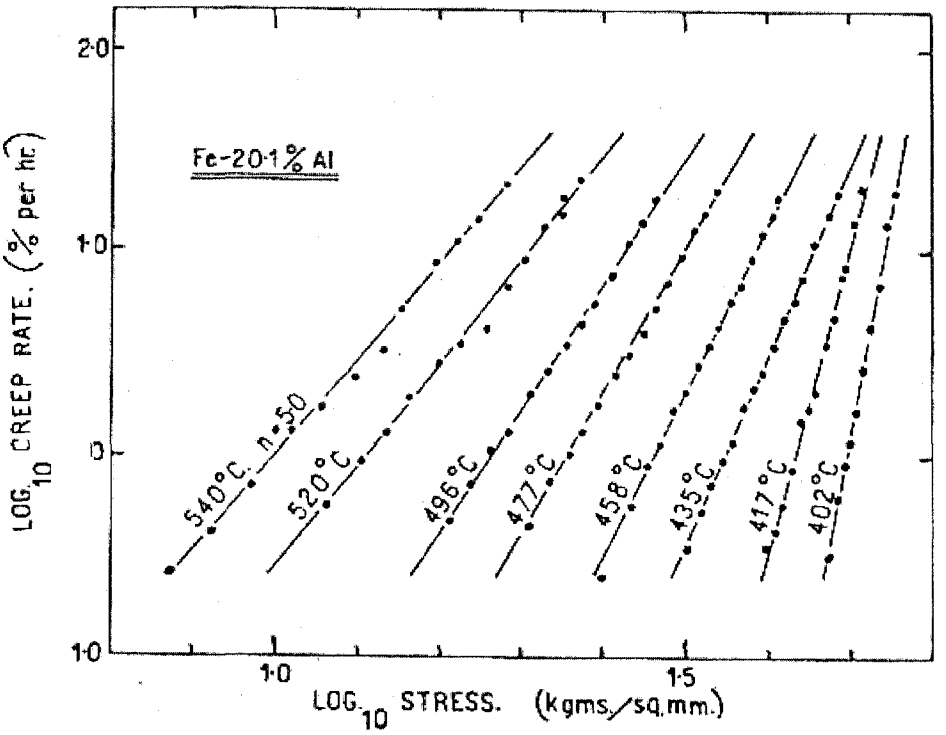

Fig. 2.14 Double log plot of steady state creep rate and stress [30].

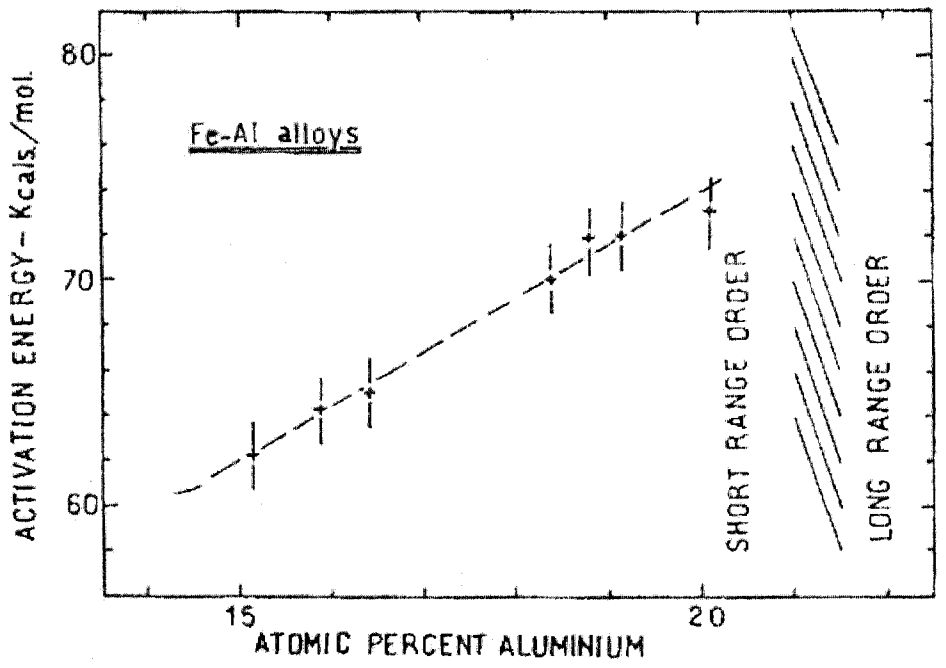

Fig. 2.15 Activation energy for steady-state creep vs composition above 500°C [30].

alloying on hot working process for a fixed deformation condition [4, 5]. Figure 2.15 compares the effect of deformation condition Z on flow stress σ of similar Fe_3Al materials (with different α values) [5]. In this project, the value of α is taken as $0.017MPa^{-1}$ for all materials to facilitate comparison. Table 2.5 lists α, Q_{HW} and values obtained at σ_P for different Fe_3Al materials. For the same material, n value at the peak strain changes greatly while Q_{HW} value varies less than 10% compared to that of Voyzelle. Figure 2.17 exhibits the effect of deformation condition Z on flow stress σ of similar Fe_3Al materials (with the same α values). Under the same condition, FeAlCr/TMT is stronger than Fe_3Al that is stronger than FAPY due to the combined effect of the alloying elements.

Table 2.4 Q_{HW}, n and lnA values obtained at σ_P and $\varepsilon = 0.5$ for different Fe_3Al materials, α varying [4, 5]

Materials (wt%)	Strain	α (MPa^{-1})	Q_{HW} (kJ/mol)	n	lnA (s^{-1})
FAPY (Fe-8.1Al-5.5Cr-2.0Mo-0.2Zr-0.02C)	Peak	0.0155	339	3.0	30.0
	0.5	0.0137	344	3.7	30.8
FeAlCr (Fe-8.3Al-6.3Cr-2.0Mo-0.2Zr-0.01C)	Peak	0.0066	383	5.8	38.4
	0.5	0.0085	339	5.0	32.8
FeAlCr/TMT (Fe-8.5Al-4.8Cr-2.06Mo-0.1Zr-0.03C)	Peak	0.0075	288	4.2	27.6
	0.5	0.0095	279	3.9	26.2
Fe_3Al (Fe-15.5Al-5.8Cr-1.0Nb-0.05C)	Peak	0.0070	352	3.8	33.3
	0.5	0.0070	330	3.7	32.2

Table 2.5 Q_{HW} and n values obtained at σ_P for different Fe_3Al materials, $\alpha=0.017MPa^{-1}$

Materials	Current values (Peak)				
	α(MPa^{-1})	n	Q_{HW} (kJ/mol)	T(°C)	$\dot{\varepsilon}(s^{-1})$
FAPY	0.017	3.3	376	800~1100	0.001~10
FeAlCr/TMT	0.017	3.2	316	800~1200	
Fe_3Al	0.017	2.9	373	900~1200	

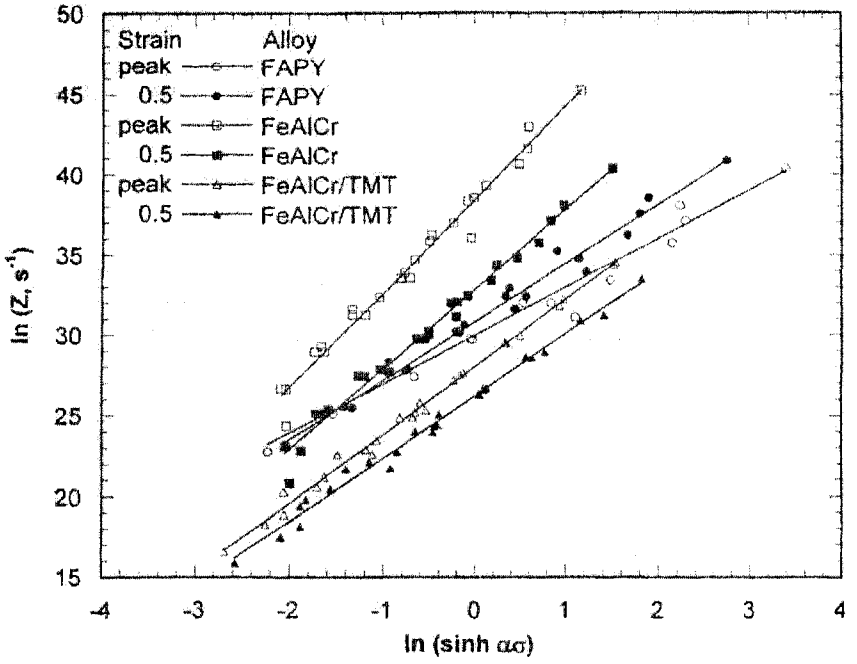

Fig. 2.16 Variation of lnZ with ln(sinh(ασ) at peak strain ε_P and ε=0.5 for FAPY, FeAlCr and FeAlCr/TMT, α varying [5].

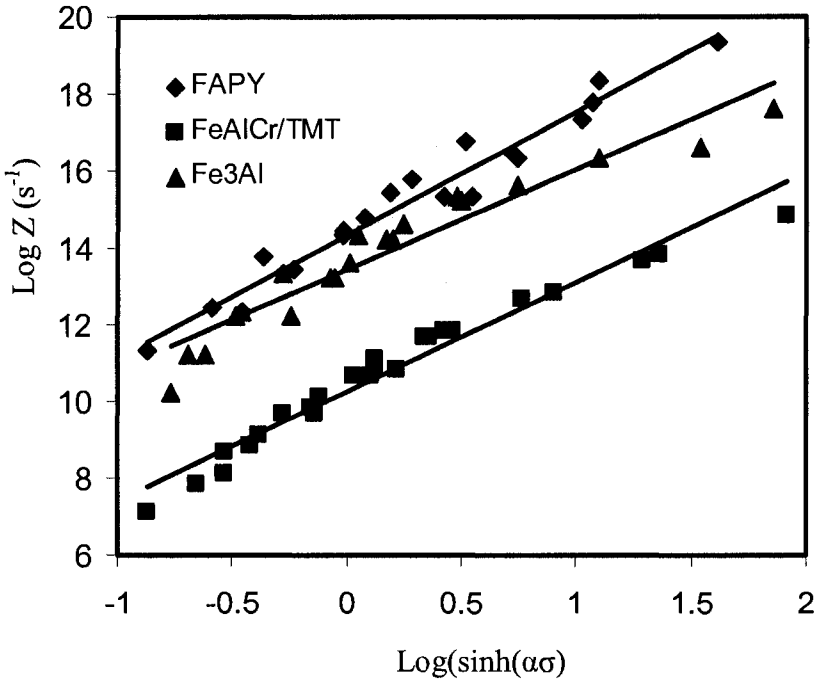

Fig. 2.17 Variation of Log Z with Log(sinh(ασ) at peak strain ε_P for FAPY, FeAlCr/TMT and Fe_3Al , $\alpha=0.017MPa^{-1}$

2.4 Review on Fe-2.7Si (wt%)

2.4.1 Composition and phase diagram

Silicon steels with Si content up to 5wt% are the most important ferromagnetic materials today. Their magnetic properties, resistivity, grain size and texture can be controlled by composition and processing. When carbon content is less than 0.02wt%, a gamma loop extends to about 2.5wt% silicon in the phase diagram as shown in Figure 2.18 [31]. The commercial composition of high permeability, grain-oriented silicon steel contains 3wt% Si and 0.07wt%C. The gamma loop is expanded because of the combination of the elements. In pure Fe-Si alloys, a 0.07wt% of carbon extends the gamma loop from 2.5 to 6.5wt% with the maximum amount of austenite at around 1150°C. Figure 2.19 shows the influence of carbon content on the amount of austenite with Si content 3.25wt% [32].

In current project, the composition of the material is Fe-2.7Si-0.06C (wt%). The

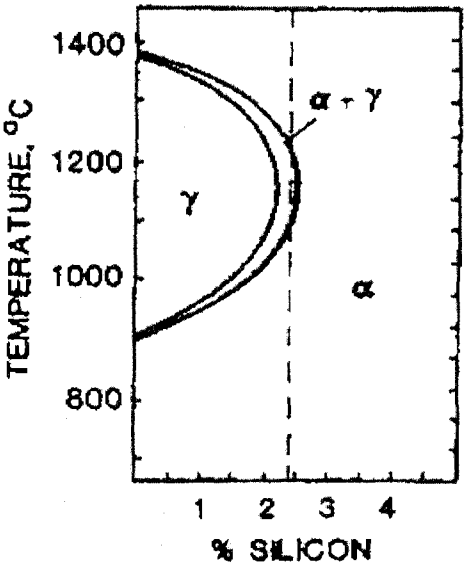

Fig. 2.18 Fe-Si phase diagram for alloys containing 0.01~0.02wt% C [31].

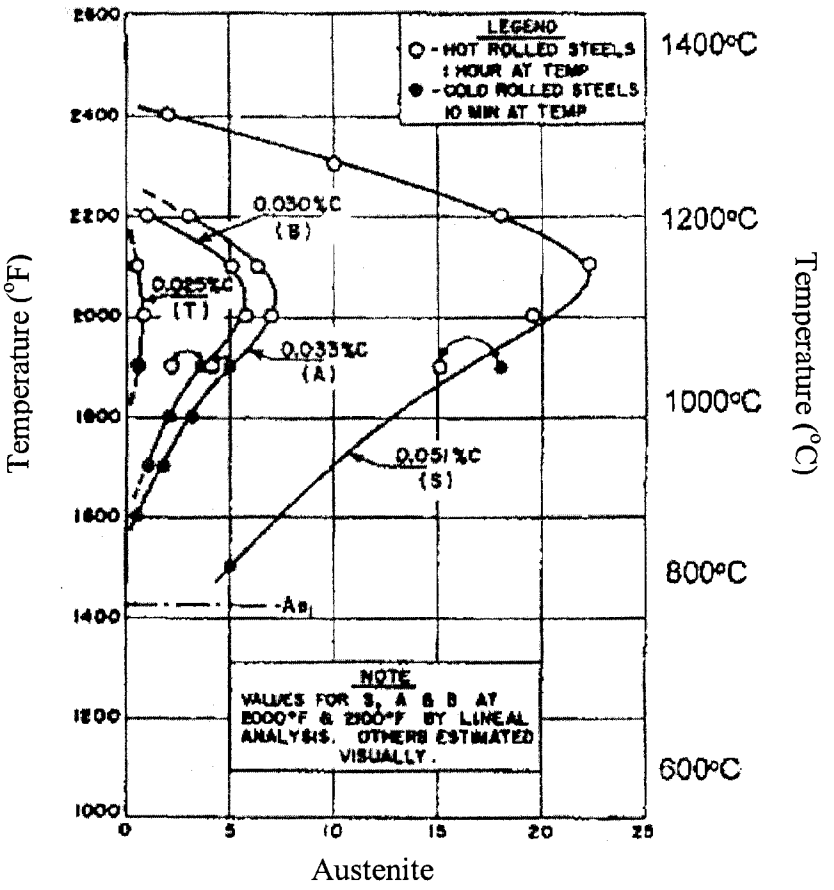

Fig. 2.19 Amount of austenite in four Fe-3.25wt% Si alloys at high T [32].

isothermal-continuous experiments were carried out within 600~900°C, which is below the range of austenite. Therefore, DRV may be the dominant restoration mechanism.

2.4.2 Composition and flow stress

Silicon and carbon contents have great influence on the flow stress of Fe-Si steels. Akta et al carried out experiments and found that with the increase of carbon content, the flow stress of the material increases as shown in Figure 2.20. The composition of the as-received slab A is Fe-3.16Si-0.036C (wt%); after decarburization, the new material is named A(2). After A is hot-rolled, annealed and decarburized, the new material is named A(3). Material A forms austenite at high T so that it has higher flow stress than A(2) and

A(3) that do not form austenite. Moreover, with the increase of T, the difference between the flow stresses of the materials becomes bigger because more austenite forms [10].

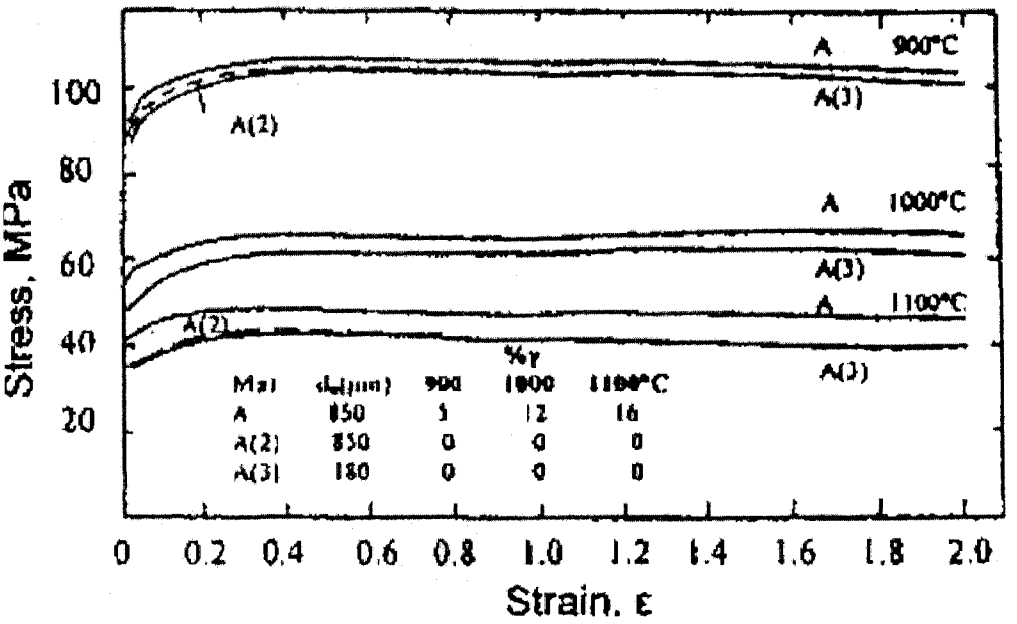

Fig. 2.20 Compression stress-strain curves for materials with and without austenite at different T and $\dot{\varepsilon} = 5s^{-1}$ [10].

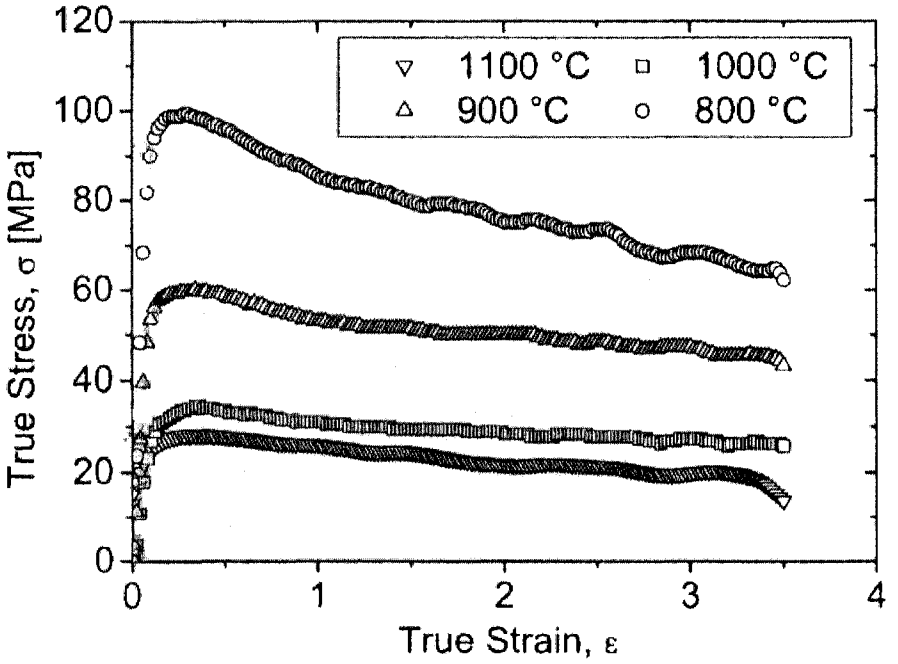

Fig. 2.21 Torsion stress-strain curves for Fe-2.0wt%Si at different T and $\dot{\varepsilon} = 2s^{-1}$ [11].

The increase of Si content leads to an increase of flow stress as shown by the comparison between Figure 2.20 and 2.21. The composition of the material in Figure 2.21 is Fe-2Si-0.003C-0.02Mn (wt%), and it has much lower flow stress at the same T compared to that of material A(2) and A(3) even with higher $\dot{\varepsilon}$.

2.4.3 Activation energy Q_{HW}

Uvira and Jonas analyzed the hot working of Fe-2.8Si-0.03C-0.45Mn (wt%) and exhibited the dependence of flow stress σ on $\dot{\varepsilon}$ and T as shown in Figure 2.22 [12]. The result of Rossard and Blain was included for better understanding [33]. σ increases with increasing $\dot{\varepsilon}$ and decreasing T. Stang investigated the relationship between creep rate $\dot{\varepsilon}$ and stress σ, temperature T of Fe-3.2Si-0.028C-0.03Mn (wt%) as Figure 2.23 and 2.24 individually [34]. The results of Lytton [35] and Barret [36] were included for comparison. The Q_{HW} values of different materials were calculated with different α values as shown in Figure 2.25 and Table 2.6 [11, 12, 34, 37, 38, 39, 40, 41]. Figure 2.25 indicates that Q_{HW} increases with the increase of Si content, because the solute pins dislocations and reduces their mobility, which makes it difficult for self-diffusion or dislocation climb. The Q_{HW} values of Armco irons and Fe-Cr alloys are included in Table 2.6 to illuminate the effect of solutes. It can be seen that Q_{HW} values of Fe-Si and Fe-Cr alloys are always higher than those of Armco irons which mainly undergo self-diffusion meaning that solutes increase the Q_{HW} values. In this project, the value of α is taken as $0.017 MPa^{-1}$ for all materials to facilitate comparing the effect of deformation condition Z on the hot working process.

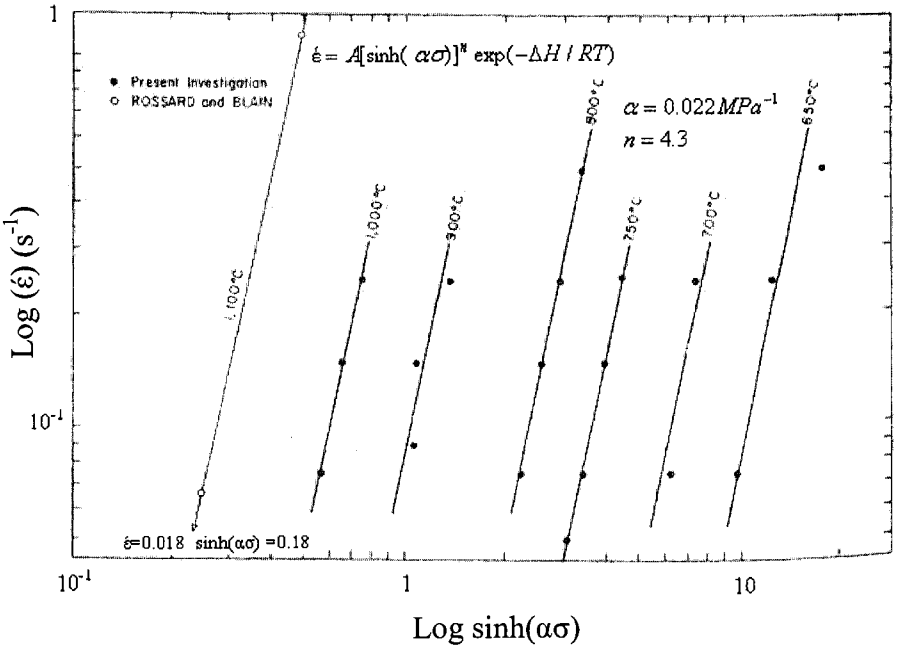

Fig. 2.22 In hot working of Fe-2.8wt%Si, the relationship between $\dot{\varepsilon}$ and σ [12].

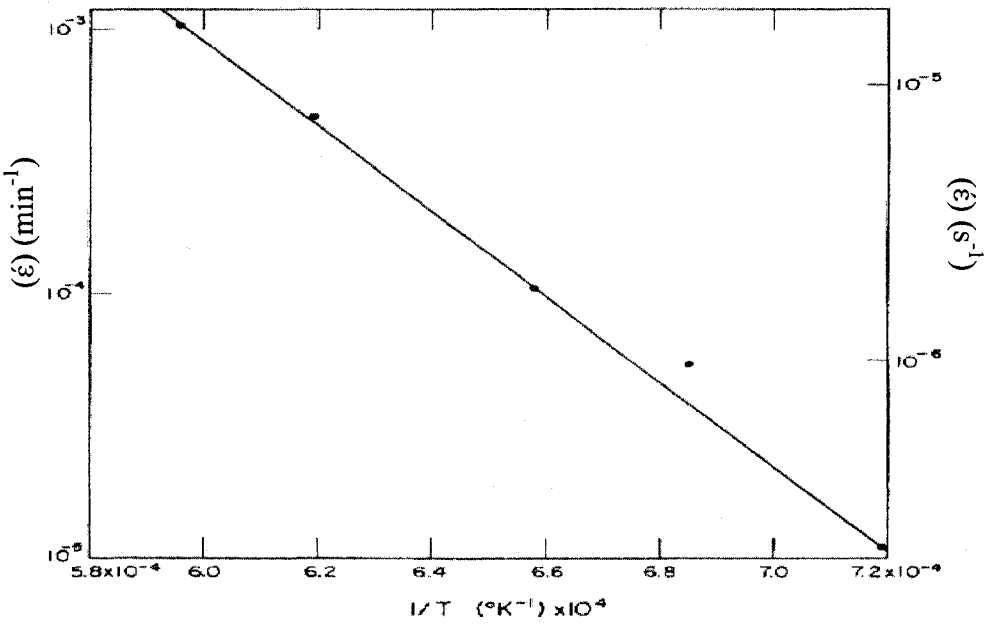

Fig. 2.23 An Arrhenius plot of steady state creep data at 413kPa for several temperatures of Fe-3.2Si. The data yield activation energy of 310kJ/mol[34].

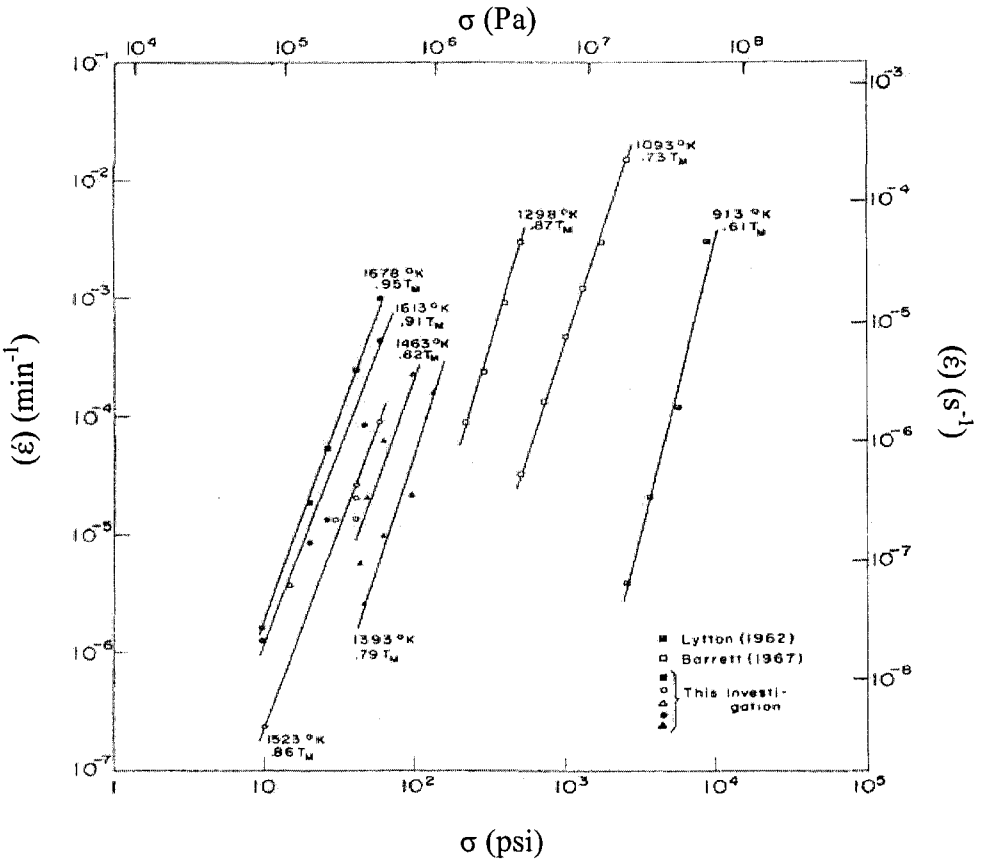

Fig. 2.24 The stress dependence of flow stress on the steady state ε̇ for Fe-3wt%Si. The data of Lytton and Barrett included for comparison [34, 35, 36]

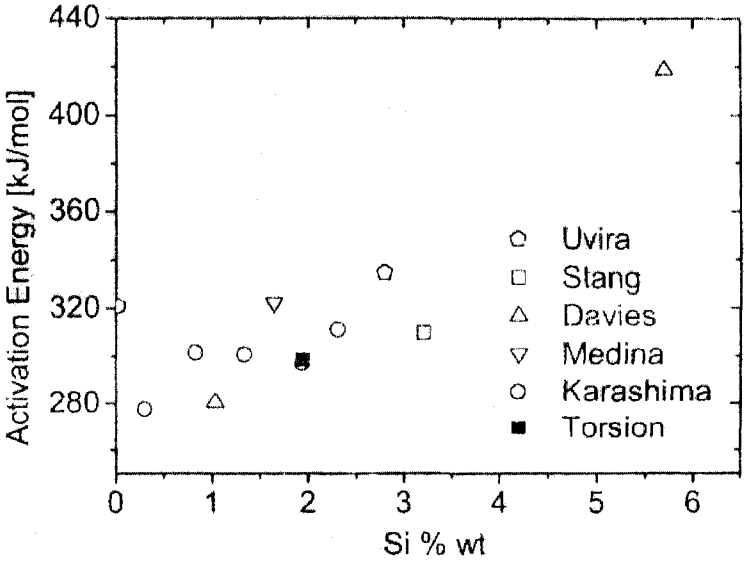

Fig. 2.25 Activation energy vs Si content from different authors [11].

Table 2.6 α and Q_{HW} values for Fe-Si and other ferritic stainless steels [10, 11, 12, 34, 39, 40, 41, 42, 43, 44]

Material (wt%)	α (MPa^{-1})	Q_{HW} (kJ/mol)	Reference
Fe-2.0Si-0.003C-0.02Mn	0.013	299	11
	0.017	261	11(Recal.)
Fe-2.8Si-0.03C-0.45Mn	0.022	335	12
Fe-3.2Si-0.028C-0.03Mn		310	34
Fe-2.31Si-0.003C		341	39
Fe-1.94Si-0.006C		314	39
Fe-3.0Si-0.036C-0.089Mn	0.017	287	10(Recal.)
Fe-2.7Si-0.06C	0.017	247	Current
	0.0166	178	9
Fe-0.02C-0.003Si (Armco iron)	0.025	276	12
Fe		280	40
Fe-0.6C-0.4Mn-0.5Ni-0.8Cr-0.2Mo		αS 168	41
		αL 412	
		γ 290	
Fe-0.2C-0.94Mn-0.05Nb		γ 434	42
Fe-16.6Cr-0.96Mo-0.21Ni-0.58Mn-0.066C (434)		397	43
Fe- 16.55Cr-0.96Mo-0.21Ni (434C)	0.017	351	6(Recal.)
Fe-11.0Cr-0.01Mo-0.49Mn-0.006C (409C)		270	43
Fe-11.0Cr-0.01Mo-0.16Ni-0.19Ti (409C)	0.017	308	13(Recal.)
Fe-25Cr (W)		207	44
Fe-18Cr-10Ni (W)		485	44

C: Cast; W: Worked; αS : Spheredized ferritics; αL : Laminar ferritics; γ : Austenites; Recal: Recalculated by the author based on original data from reference indicated.

2.4.4 Multi-stage tests

In industry, a hot working process such as rolling is usually composed of several stages with declining T. Each pass of the simplified rolling schedules is defined with parameters such as temperature T_i, strain rate $\dot{\varepsilon}_i$, pass strain ε_i and interval time t_i. In simulation of rolling, all parameters are constant in each pass but may vary from pass to pass. The stress on reloading at the start of each pass is σ_{ri} and reaches a maximum σ_{mi} at

the end. The material hardens but undergoes restoration simultaneously in each pass. During the interval between two neighboring stages, SRX and SRV may occur, which leads to both fractional softening (FS) and a complex microstructural evolution of the material. The simulation of FS_i of each pass elucidates the fraction of SRX and SRV with declining T. The fraction of SRX and FS were investigated with 300 series stainless steels and aluminum alloys in multi-stage deformation [45, 46, 47, 48, 49, 50, 51, 52, 53]. The retained strain energy at the end of pass i is:

$$S_i = (\sigma_{mi} - \sigma'_{yi}) / \sigma'_{yi} \qquad (2.6)$$

Here, σ'_{yi} is the yielding stress of the recrystallized material at T_i. The residual hardening at the start of pass $i+1$ is:

$$S_{O(i+1)} = (\sigma_{y(i+1)} - \sigma'_{y(i+1)}) / \sigma'_{y(i+1)} \qquad (2.7)$$

Here, $\sigma_{y(i+1)}$ and $\sigma'_{y(i+1)}$ are the actual and recryatllized yielding stresses at T_{i+1}. σ'_{yi} and $\sigma'_{y(i+1)}$ can be calculated from the constitutive equation of isothermal tests. From equations 2.6 and 2.7, FS_i in interval i can be calculated as:

$$FS_i = (S_i - S_{O(i+1)}) / S_i$$

$$= [\sigma_{mi} - \sigma_{y(i+1)} \cdot (\sigma'_{yi}) / \sigma'_{y(i+1)})] / (\sigma_{mi} - \sigma'_{yi}) \qquad (2.8)$$

However, in this project, FS is not calculated because the values of σ_{yi} are affected by solute pinning of dislocations, which is reflected by the oscillation of the isothermal

continuous flow curves around the strain of 0.2%. Instead, the relative softening (RS) and relative reduction of stress (RRS) of the material were calculated with equations 2.9 and 2.10:

$$RS = \frac{\sigma_{mi} - \sigma_{r(i+1)}}{\sigma_{mi}} \tag{2.9}$$

$$RRS = \frac{\sigma_{Pi} - \sigma_{mi}}{\sigma_{Pi}} \tag{2.10}$$

Here, σ_{Pi} is the peak stress in isothermal-continuous deformation under T_i and $\dot{\varepsilon}_i$.

2.4.4.1 Fe-2.0wt%Si steels

Calvillo et al [12] did 16-stage deformation of Fe-2.0Si-0.003C-0.02Mn (wt%) (the temperature decreased from 1100 to 800°C, $\dot{\varepsilon}_i = 1s^{-1}$, $\varepsilon_i = 0.1$, $t_i = 5s$) as shown in Figure 2.26 but did not analyze the fraction of SRX and FS . Based on multi-stage flow curve shown in Figure 2.26 and the relationship between mean flow stress and T shown in Figure 2.27, RS compared to σ_{mi} and RRS compared to σ_{Pi} were calculated as shown in Figure 2.28 and 2.29.

Figure 2.28 exhibits that RS increases with the decrease of T_i, which is unreasonable. When T decreases from T_i to T_{i+1}, due to the larger combined effect of DRV in the preceding pass ($T_{i-1} = T_i + 20$, °C) and the static softening during the interval after pass $i-1$, the substructure carried from stage i over to stage $i+1$ becomes harder than that carried from stage $i-1$ to stage i so that $\sigma_{r(i+1)}$ should become bigger than σ_{ri},

which causes a decrease of RS relative to σ_{mi}. The unreasonable increase is due to the unreasonable decrease of σ_{ri} as shown in Figure 2.26.

According to Figure 2.29, the amount of RRS increases to a peak at 920°C and then decreases. Two mechanisms strain hardening and softening function simultaneously during deformation in each pass, and the material also undergoes static restoration during the following interval. At 1100°C, the specimen undergoes a high level of restoration and almost returns to its original state. As a result, there is little difference between σ_{P1} and σ_{m1}, which leads to a very low value of RRS. In the range 1100~920°C, when T decreases from T_{i-1} to T_i, the material requires bigger ε_i to reach steady state σ_{Pi} where $\sigma_{Pi} = \sigma_{mi}$. A fixed ε_i causes a bigger and bigger difference between σ_{Pi} and σ_{mi}

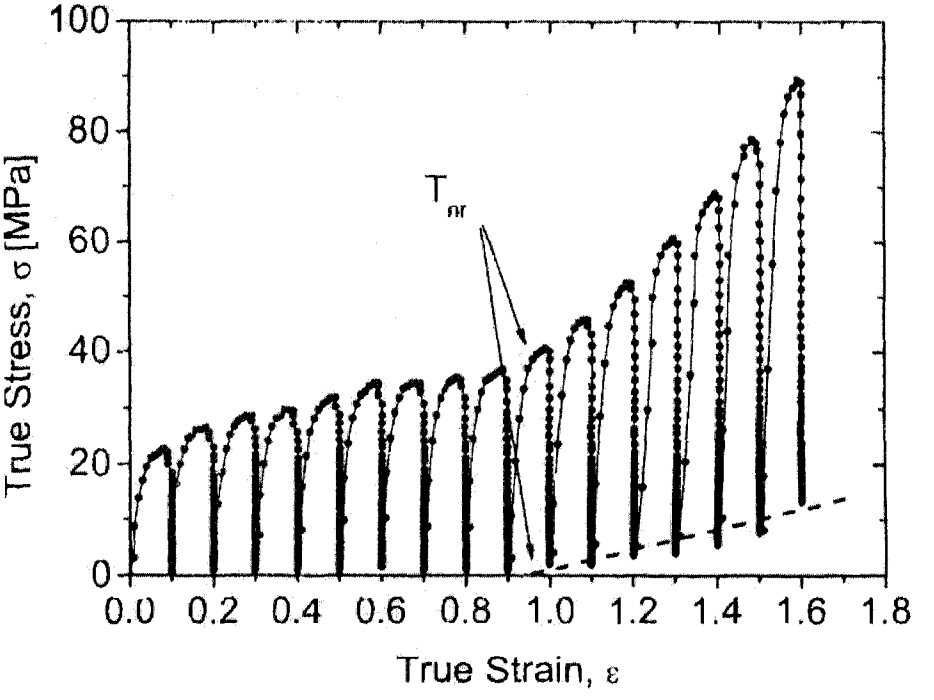

Fig. 2.26 16-stage schedule with Fe-2.0wt%Si in torsion tests with T_i decreasing from 1100 to 800°C, $\dot{\varepsilon}_i = 1s^{-1}$, $\varepsilon_i = 0.1$, $t_i = 5s$ [11].

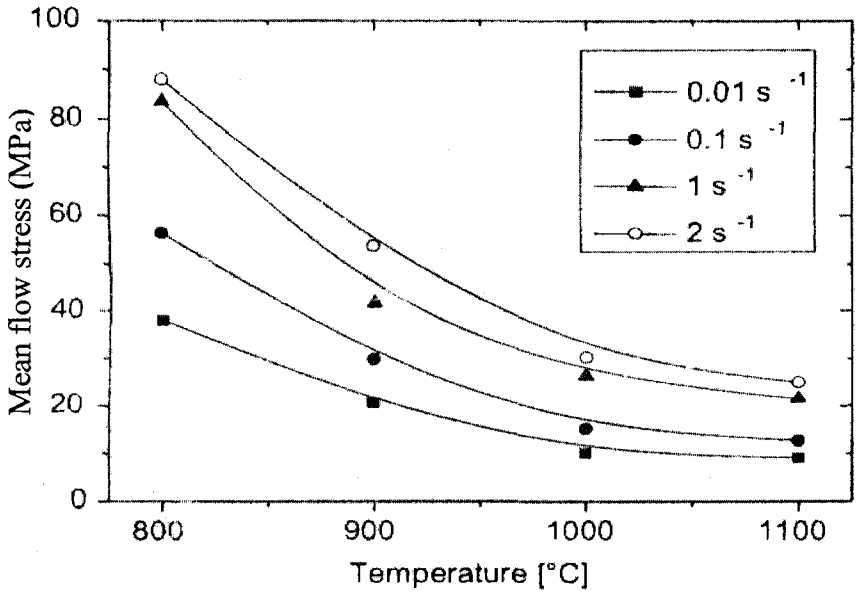

Fig. 2.27 Mean flow stress for Fe-2.0wt%Si in torsion at different T [11].

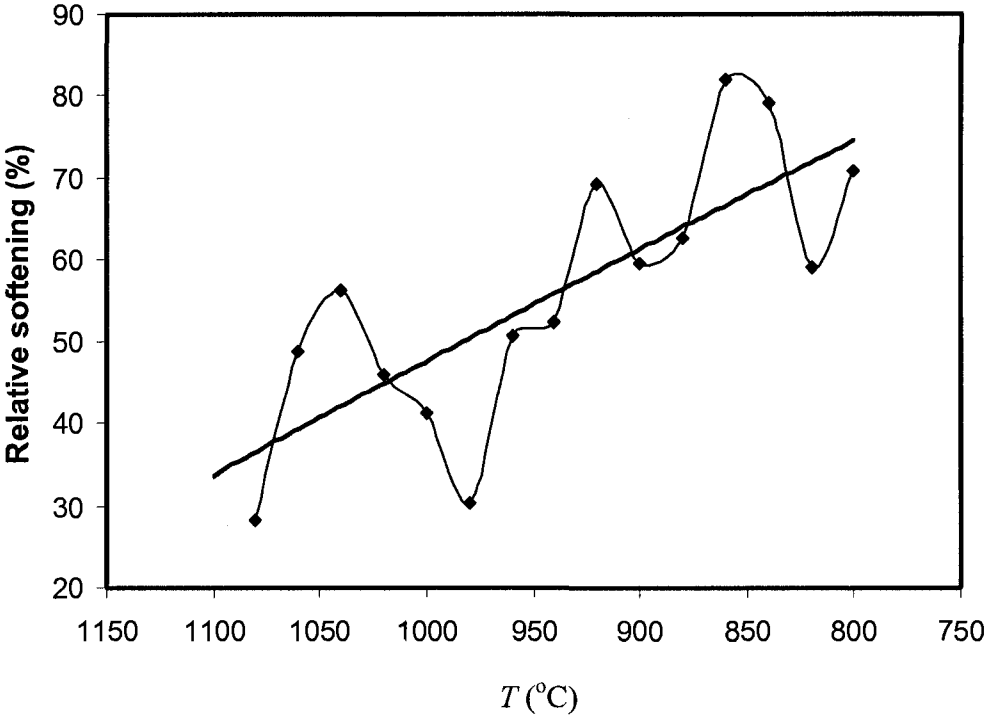

Fig. 2.28 Relative softening for Fe-2.0wt%Si in torsion at declining T_i with $\dot{\varepsilon}_i = 1s^{-1}$.

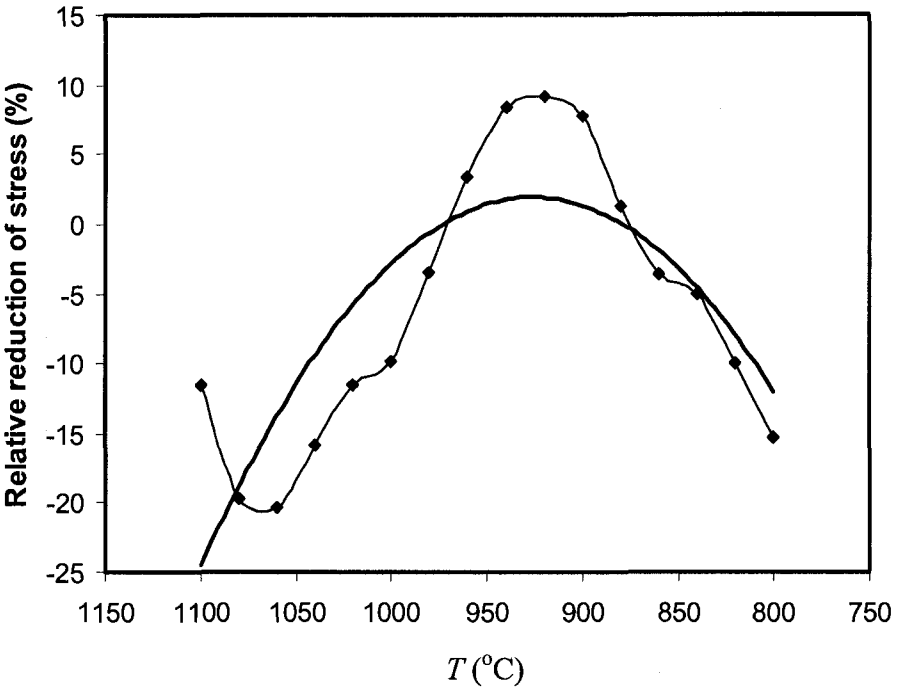

Fig. 2.29 Relative reduction of stress for Fe-2.0wt%Si in torsion at declining T_i with $\dot{\varepsilon}_i = 1s^{-1}$.

so that when σ_{Pi} increases slightly from pass to pass, *RRS* increases until a peak at 920°C. When T_i decreases from 920 to 800°C, the material hardens faster but restores slower so that σ_{Pi} increases fast but difference between σ_{Pi} and σ_{mi} decreases, *RRS* decreases. This result indicates that 920°C is the optimal T in industrial rolling.

T_{nr} in Figure 2.26 refers to the T_i where SRX stops to be complete and partial SRX and SRV cause softening during the intervals. A schematic dependence of mean flow stress (MFS) in a pass on the inverse pass temperature T_i for Fe-2.0wt%Si in multi-stage torsion test with declining T_i is shown in Figure 2.30. In region I, complete SRX and SRV cause softening; in region II, partial SRX and SRV work for softening; T_{nr} differentiates the two regions. In region III, only SRV works for softening. Fe-3.0Si

(wt%) sheets are hot-rolled and cooled in region II and III so that the sheets end up with a mixture of elongated and fine ferritic grains; then the sheets will be cleaned, cold-rolled and continuously annealed for shaping into transformers at room temperature.

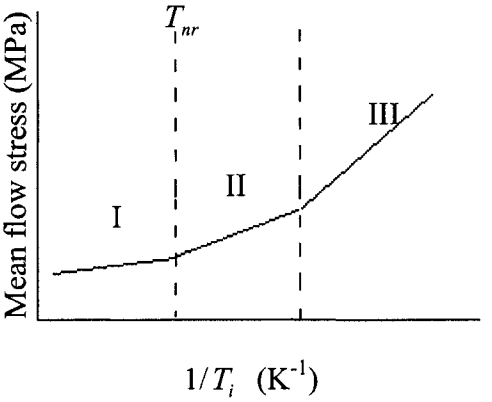

Fig. 2.30 A schematic dependence of MFS on inverse T_i for Fe-2.0wt%Si in torsion at declining T_i. T_{nr} differentiates region I with complete SRX and SRV; region II has partial SRX and SRV; region III only has SRV.

2.4.4.2 Aluminum alloys

In hot working, Al alloys with FCC crystal structure have similar high capability of DRV to that of silicon steels with BCC structure thus sharing many similarities in behavior. For pure Al, Poschmann and McQueen [53] carried out isothermal-continuous tests and 5, 9, 17-stage deformations with $\varepsilon_i = 0.92$, 0.46 and 0.23 and $t_i = 376$, 188 and 94 seconds respectively when $\dot{\varepsilon}_i = 1.16 s^{-1}$ and T_i declines from 500 to 300°C as shown in Figure 2.31. The values of σ_{mi} and σ_{ri} are taken as shown in Figure 2.32. At any stage T_i, σ_{Pi} is always higher than σ_{mi} because the specimen undergoes strain hardening but never reaches the steady state of the isothermal-continuous test. In the 5-stage test with $\varepsilon_i = 0.92$, the specimen undergoes the highest level of strain hardening so that it has the highest σ_{mi}

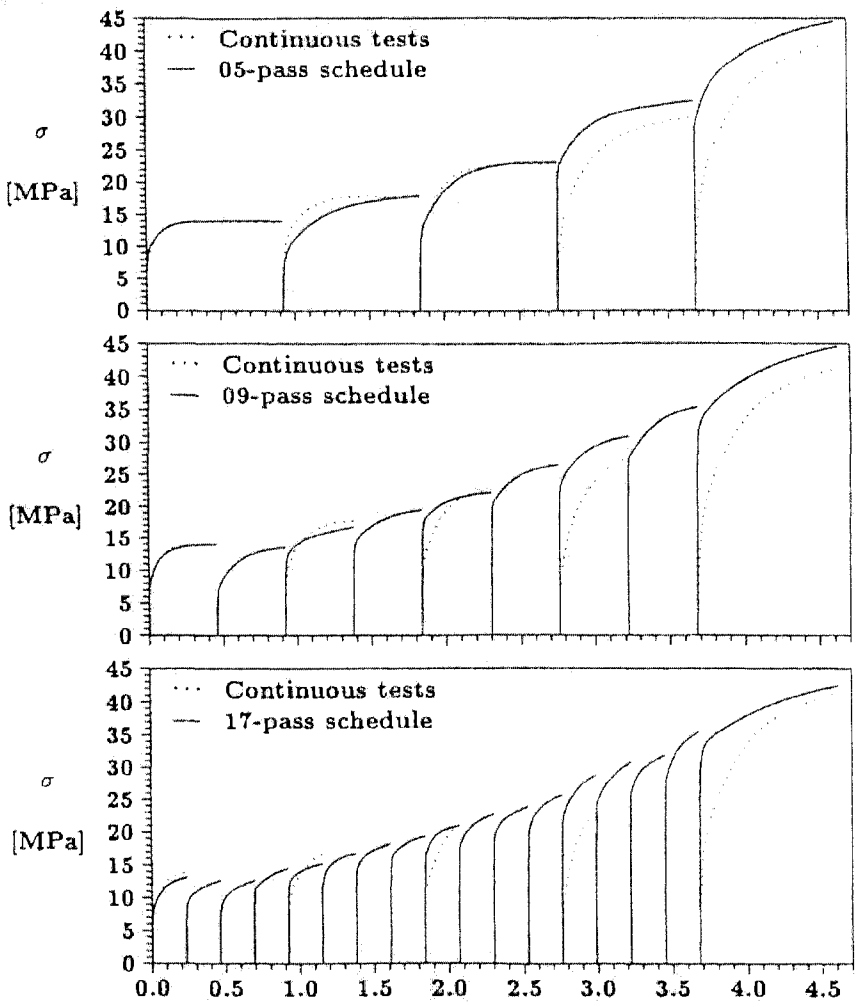

Fig. 2.31 5, 9 and 17-stage deformation curves of pure Al. The dotted lines represent continuous stress-strain curves shifted into the ε-position of the multi-step passes deformed at the same T_i [53].

compared to the 9-stage test with $\varepsilon_i = 0.46$ and 17-stage test with $\varepsilon_i = 0.23$. Moreover, the 5-stage specimen has the longest interval 376s to restore so that it has the lowest σ_{ri}. The specimen for 9-stage test has medium σ_{mi} and high σ_{ri}. The specimen for 17- stage test has the lowest σ_{mi} but high σ_{ri}.

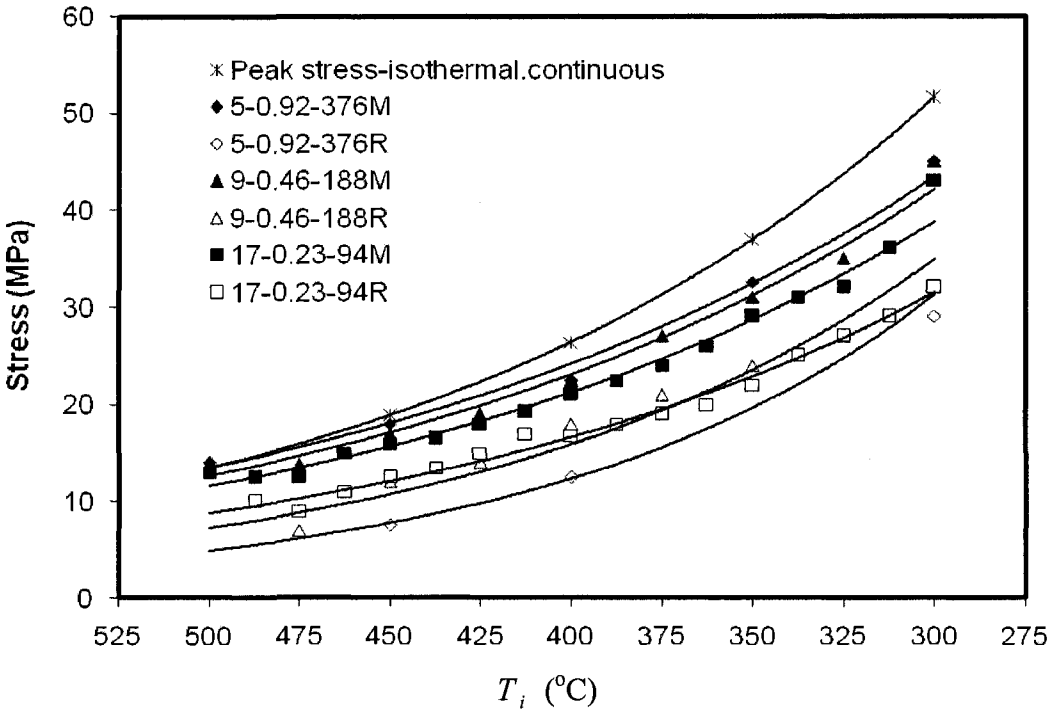

Fig. 2.32 σ_{Pi} for Al in in isothermal-continuous tests, maximum stress σ_{mi}, reloading stress σ_{ri} of each pass in 5, 7, 9-stage rolling schedule with T_i decreasing from 500 to 300°C and $\dot{\varepsilon}_i = 1.16s^{-1}$, ε_i is 0.92, 0.46 and 0.23 and t_i is 376, 188 and 94 seconds respectively.

When T decreases from 500°C (~0.83 T_M, melting temperature) to 300°C (~0.61 T_M), RS_i decreases with the highest rate for 5-stage, medium rate for 9-stage and lowest rate for 17-stage deformation as shown in Figure 2.33. Two mechanisms strain hardening and DRV function simultaneously during deformation in each pass, and the material also undergoes SRV and SRX during the following interval. At 500°C, the specimen undergoes a high level of restoration, as a result, there is little difference between σ_{m1} and σ_{r1}. But because of the low value of σ_{m1}, RS_i value is high. When T_i decreases, both σ_{mi} and σ_{ri} increase because of the lower level of DRV during pass i and lower level of SRV and SRX during

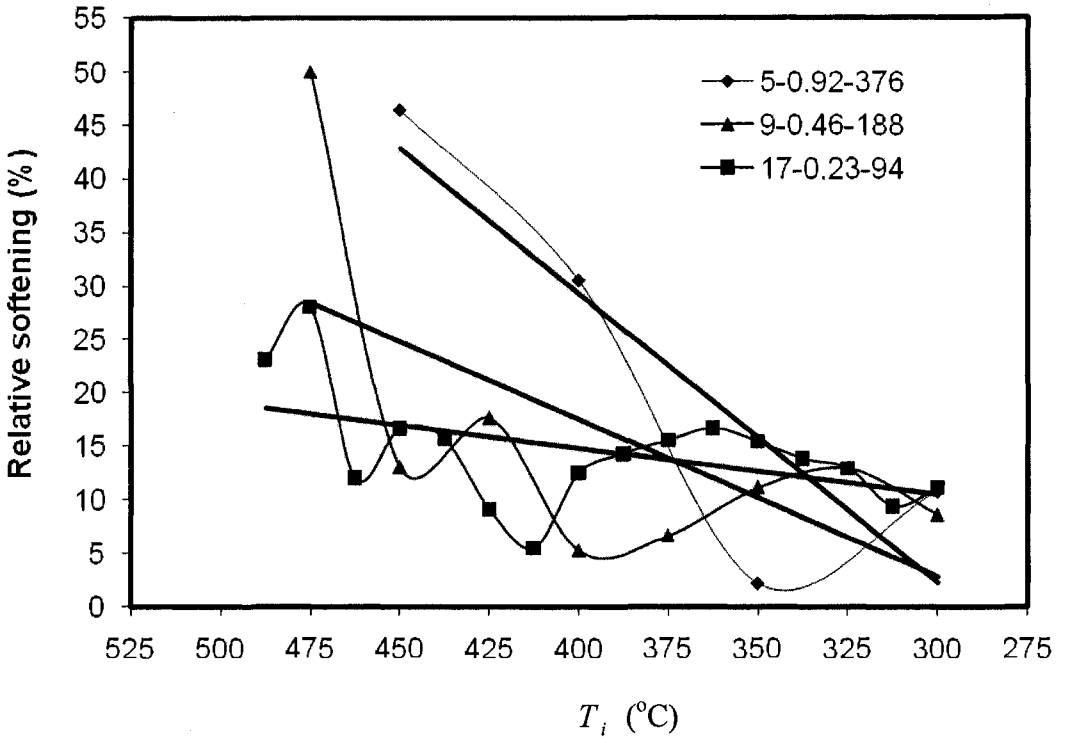

Fig. 2.33 Relative softening for pure Al in 5, 9 and 17-stage rolling with $\dot{\varepsilon}_i = 1.16s^{-1}$.

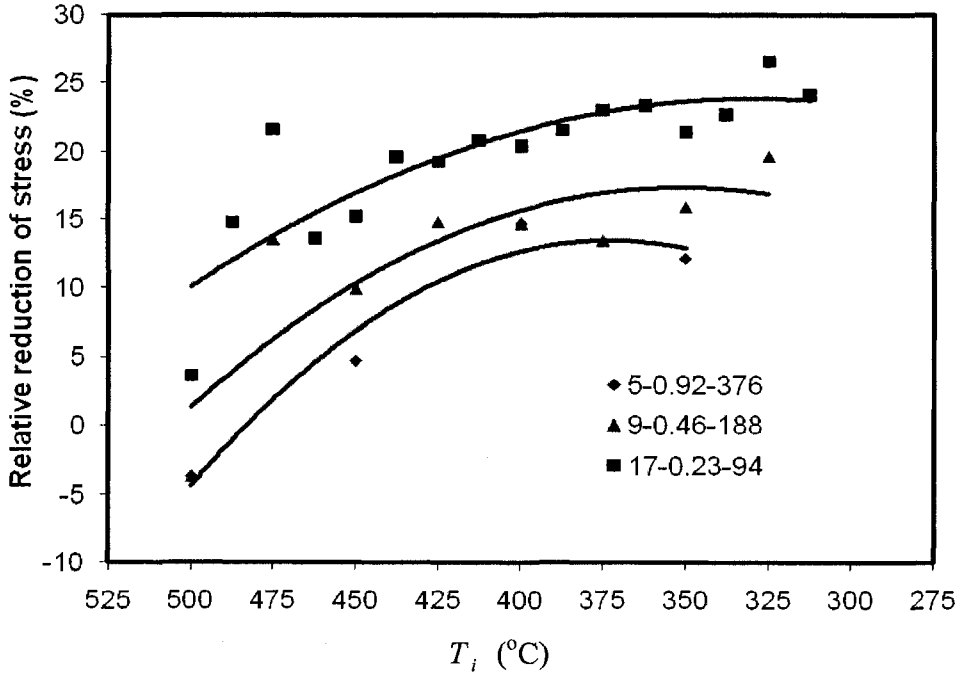

Fig. 2.34 Relative reduction of stress for pure Al in 5, 9 and 17-stage rolling with $\dot{\varepsilon}_i = 1.16s^{-1}$.

the interval after pass i, which leads to a smaller difference between σ_{mi} and σ_{ri}. As a result, RS_i value relative to the increasing σ_{mi} keeps decreasing.

In Figure 2.34, RRS_i increases until a peak around 350°C and then decreases slightly as shown in Figure 2.33. At 500°C, the specimen undergoes a high level of restoration and almost returns to its original state. As a result, there is little difference between σ_{P1} and σ_{m1}, especially for the 9, 17-stage deformation as shown in Figure 2.30, which leads to a very low value of RRS. In the range 500~350°C, when T decreases from T_{i-1} to T_i, the material requires bigger ε_i to reach steady state σ_{Pi} where $\sigma_{Pi} = \sigma_{mi}$. A fixed ε_i causes a bigger and bigger difference between σ_{Pi} and σ_{mi} so that when σ_{Pi} increases slower from pass to pass, RRS increases until a peak at 350°C. When T_i decreases from 920 to 800°C, the material hardens faster but restores slower so that σ_{Pi} increases fast but difference between σ_{Pi} and σ_{mi} decreases, RRS_i decreases. For the last pass in each schedule, the strain is 1.0, much higher than previous ones, σ_{mi} of the last pass is much higher as shown in Figure 2.32. As a result, RRS_i values of the last pass are unreasonably low so that they are omitted from analysis.

Figure 2.35 presents the values of FS_i for decreasing T_i [53]. The arrows indicate the microstructure observed in specimens quenched at the end of the interval. The initial value FS_0 was set as 1. The first interval of the 5-stage test is dominated by SRX followed by grain growth (GG), causing FS_1 value to exceed 1. The second interval with FS_2 decreasing to about 0.85 mainly features SRX with a low volume of unrecrystallized material. SRX ceases to be complete and the temperature is marked as

T_{nr} as shown in Figure 2.36 [53]. The sole restoration mechanism in the last two intervals ($\leq 350°C$, $0.67T_M$) is SRV with FS_i being about 0.3.

The 9-stage test has similar features to those of 5-stage test. The first interval causes FS_1 value of 1.25 indicating a complete SRX followed by GG. FS_2 drops to about 0.65 at the end of the second interval, and the material has considerable SRX combined with big areas of recovered grains. T_{nr} is marked here as in Figure 2.36. At the end of the fourth interval, the fraction of SRX drops and FS_4 value is about 0.4. SRV is the only restoration mechanism in the remaining intervals ($\leq 375°C$, $0.69T_M$) and FS_i value decreases to 0.25 at the end of the test [53].

The 17-stage test does not see any GG but attains complete SRX in the first two intervals, T_{nr} is also marked here as in Figure 2.36. At lower T_i, FS_i decreases because the fraction of SRX decreases. At the end of sixth interval, FS_i becomes quite low. SRV becomes the sole restoration mechanism since the ninth interval when $T_i \leq 400°C$, $0.72T_M$ [53].

From the comparison between Figure 2.34 and 2.35, RS_i in the range 40~50% or $RRS_i \leq 5\%$ is related to a complete SRX and GG, $FS_i > 100\%$; RS_i of 20~35% or RRS_i of 5~10% is related to a complete SRX, RS_i of 15~20% o RRS_i of 10~15% related to partial SRX, and RS_i below 15% or RRS_i of 15~25% is solely SRV. FS_i and RS_i decline but RRS_i rises as T_i decreases because as discussed above.

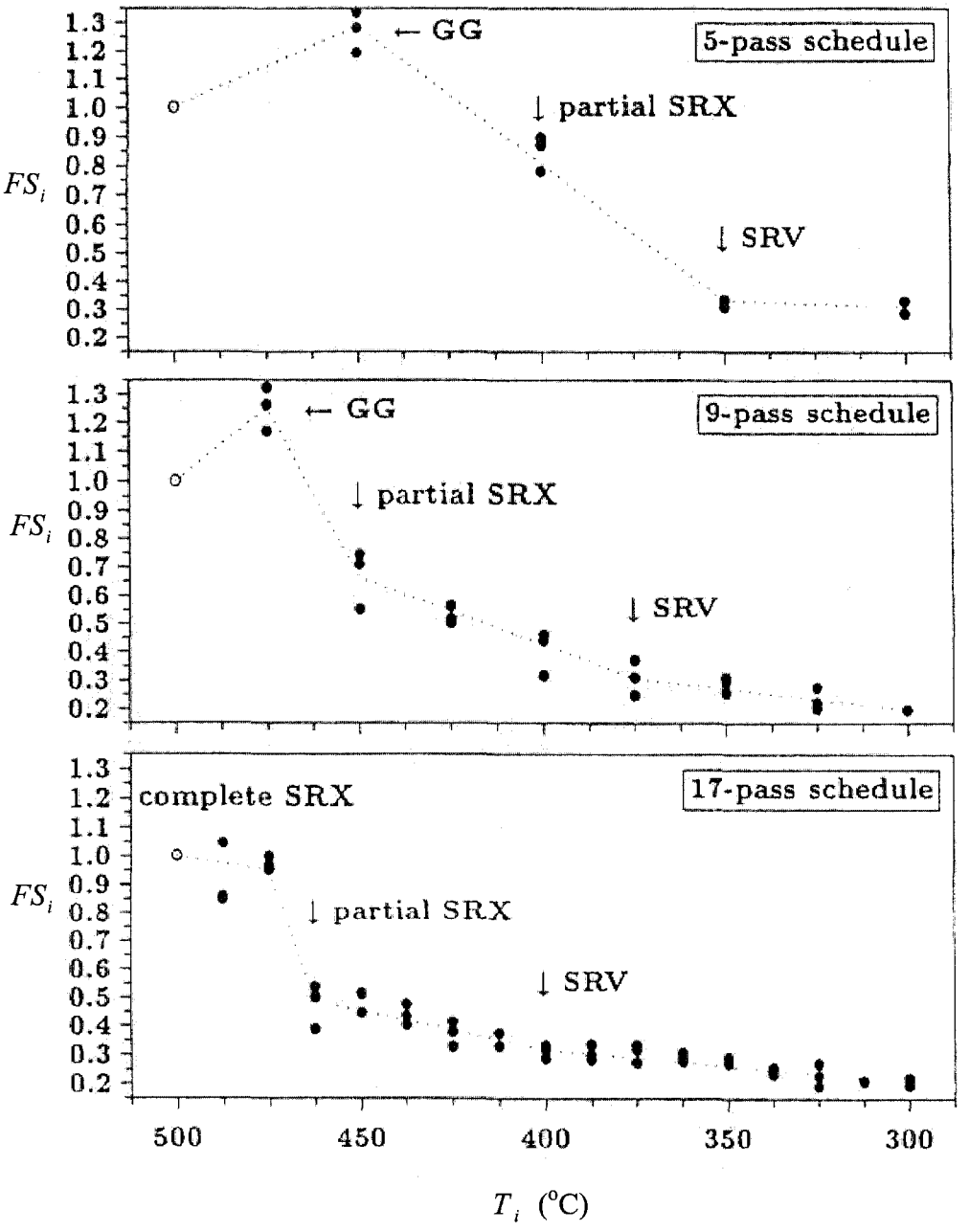

Fig. 2.35 Fractional softening FS_i during the pass intervals of 5, 9 and 17-stage rolling tests under different T_i at which the interval concluded. Data points related to grain growth (GG) and complete SRX are included. Also shown are the region of partial SRX and the point below which there is only SRV indicated by the downward arrows [53].

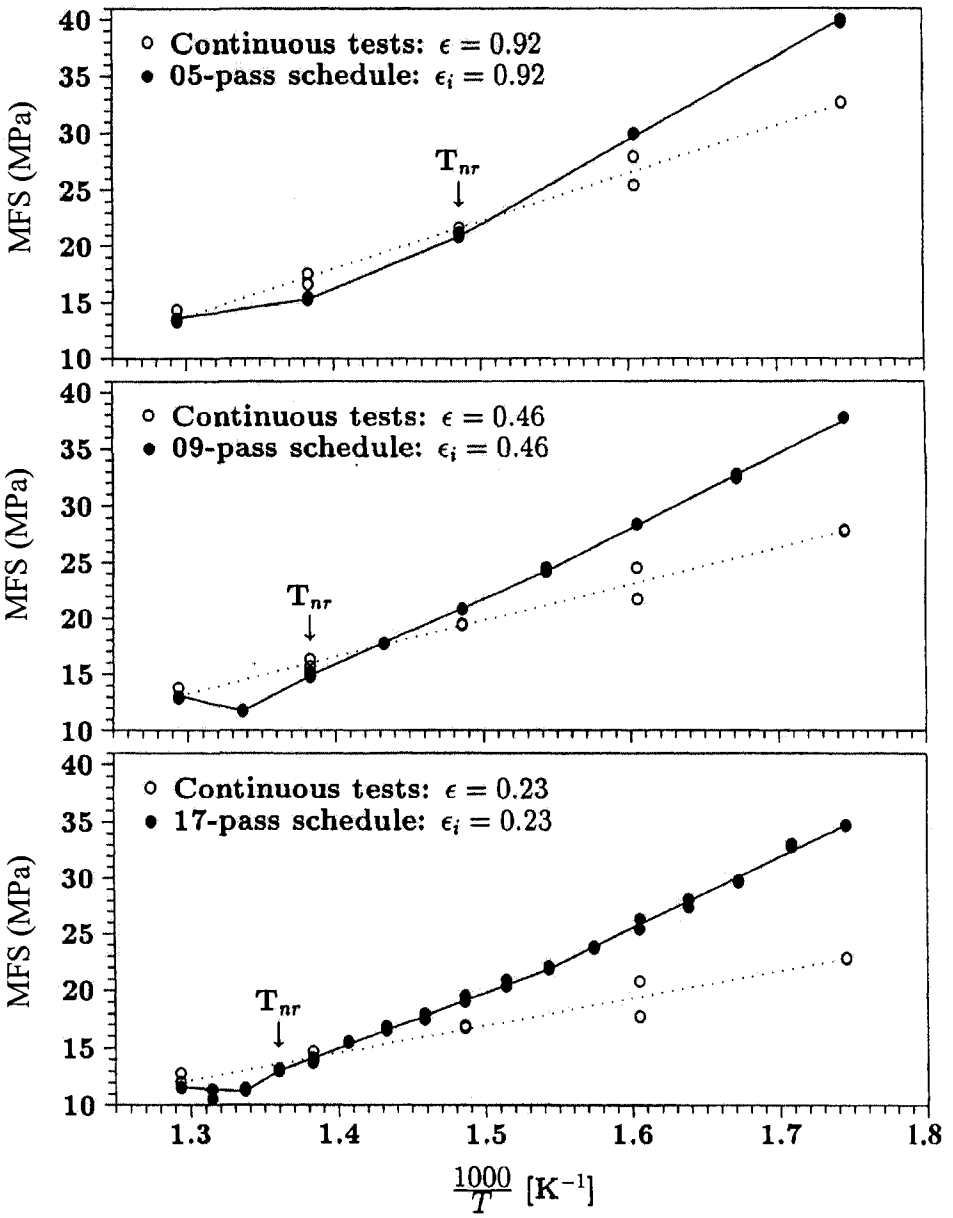

Fig. 2.36 Temperature dependence of MFS during the multi-stage deformation. The dotteed lines represent MFS values for isothermal continuous tests [53].

2.4.5 SRX and grain growth (GG)

English and Backofen [54] carried out hot-compression tests with Fe-3.2Si-0.11Mn-0.03C (wt%) to axial strain of 0.1 to 0.7 at $\dot{\varepsilon}$=100 s^{-1} over the range 710~911°C. They analyzed by optical microscopy the variation of the fraction X_s of SRX with

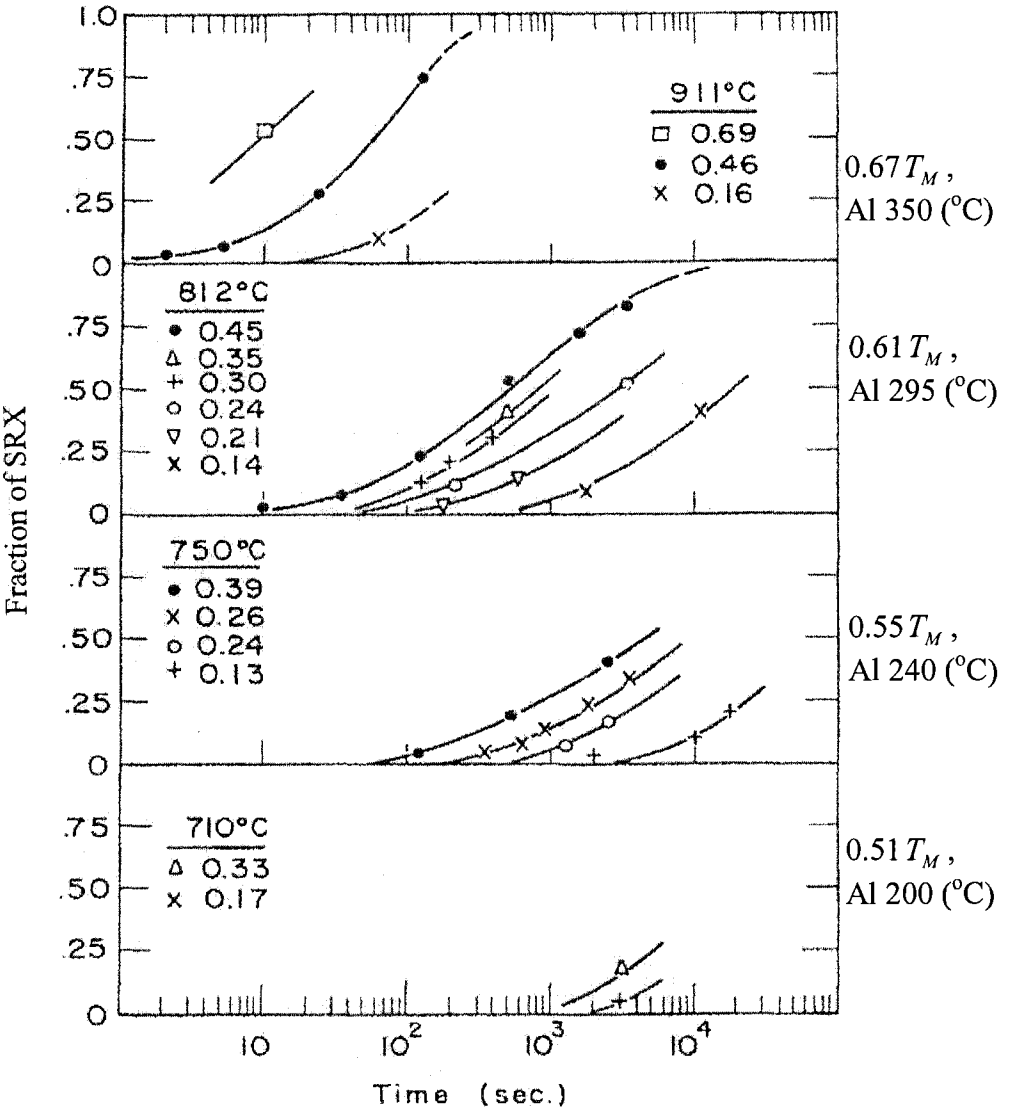

Fig. 2.37 In hot-compression tests with Fe-3.2Si-0.11Mn-0.03C (wt%), the variation of fraction of SRX X_S with holding time at deformation T. Symbols suggest strains ε of the tests [54].

holding time at the deformation T as shown in Figure 2.37. At a fixed T such as 812°C, the increase of deformation strain ε, for example from 0.14 to 0.45 leads to shorter nucleation times (600 down to 10s) and an increase of X_S from 10 to 75% at 2000s due to the increase of strain energy. When specimens are deformed to similar strains such as

0.16 at 911°C, 0.14 at 812°C, 0.13 at 750°C and 0.17 at 710°C, the decrease of deformation and holding T from 911°C to 812 and then 710°C causes a substantial increase of holding time from about 20 seconds to about 600 seconds and then thousands of seconds to nucleate recrystallization. Also at these similar strains around 0.15, if holding time is fixed as 100s, no SRX occurs except an X_S value of about 0.13 at 911°C. However, if the strain is increased to about 0.45, nucleation of SRX starts at a shorter time, for example, from 600 down to 10s at 812°C; and with a fixed holding time 100s, the specimens have X_S value of 0.75 at 911°C, 0.25 at 812°C and 0.05 at 750°C but no recrystallization at 710°C.

Due to the design of these isothermal-continuous tests, they could be converted to a 3-stage test with T_i decreasing from 910 to 810 and then 710°C, ε_i being either 0.2 or 0.4 and t_i being 10, 20, 40 or 100 seconds. This will provide important clues for analyzing the effect of T_i, ε_i and t_i on the softening of Fe-2.7Si-0.06C when $\dot{\varepsilon}$ is constant.

Nucleation of new grains mainly occurs at the triple junctions of the original grains with some along grain boundaries (GBs) and some around inclusions. Figure 2.38 exhibits the average grain growth rate G during the progress of recrystallization when the specimens are deformed at the T to the strain as indicated and then held at the same T. A relationship is found as below:

$$G = \frac{0.004}{t} \qquad (2.11)$$

Here, t is time. From this equation, the first-formed nuclei account for a predominately large fraction of recrystallization. During recrystallization, G is observed to decrease by two orders of magnitude at first but more slowly later on, which is qualitatively consistent

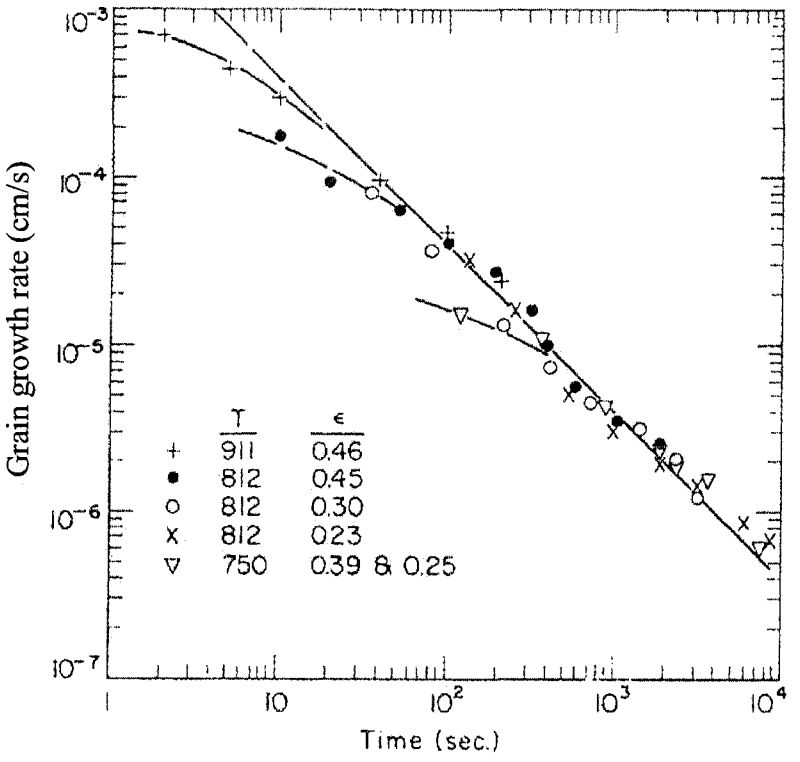

Fig. 2.38 In hot-compression tests with Fe-3.2Si-0.11Mn-0.03C (wt%) specimens deformed at T to the strain as indicated and then held at the same T, average grain growth rate versus holding time calculated based on data in Figure 2.35 [54].

with the mechanism of homogeneous recovery. Moreover, solute segregation to GBs in the unrecrystallized material may also affect the grain growth rate. In hot working, inclusions cause a high density of nuclei within the grains, which refines the SRV grains.

2.4.6 Microstructure analysis

2.4.6.1 Microstructure evolution of Fe-3Si and Fe-25Cr

C. S. Barrett et al [55] investigated the substructure evolution for Fe-3Si as a function of creep strain at 643°C, 0.51 T_M and 48MPa with grain diameter 0.1mm as

shown in Figure 2.39. Dislocations form loose tangles after a relatively small strain 0.008 as shown in Figure 2.39a; at a strain of 0.038, the accumulated dislocations progress into a loose substructure in Figure 2.39b; at a strain of 0.141, a cellular substructure with regular walls has been formed and steady-state creep starts, then the substructure is maintained equiaxed and stable with a diameter of 10μm. Rossard [56] investigated the substructure evolution of Fe-25Cr with strain at 1100°C, $\dot{\varepsilon}=1.11s^{-1}$ as shown in Figure 2.40. Nondeformed specimens have grains as shown in Figure 2.40a. At a strain of 0.22, substructures are formed within grains, but their walls are not dense enough to etch strongly so that GBs are more noticeable and easily differentiated (Figure 2.40b). When strain is increased to 0.88, subgrains are well-formed inside grains. However, because of the etching dependence on grain orientation, they are easily seen in some grains but difficult in others as shown in Figure 2.40c. When strain reaches a high value of 1.32 (Figure 2.40d), equiaxed subgrains with approximately constant size are formed inside the grains. At a strain of 3.7 (Figure 2.40e), the subgrains cover the whole surface, but their boundaries are not etched up so that some boundaries cannot be seen.

Substructure has very regular walls in creep but denser, less regular walls in hot working. The investigation of creep substructure for Fe-3.0Si [55] provides some clues to the substructure evolution in hot working. Fe-25Cr has similar BCC structure to that of Fe-2.7Si; consequently, its substructure evolution has some similarity to that of Fe-2.7Si. However, Cr atoms being fairly similar to those of Fe has less interaction with dislocations than does Si. As a result, 25%Cr produces substructures somewhat similar to 3% Si.

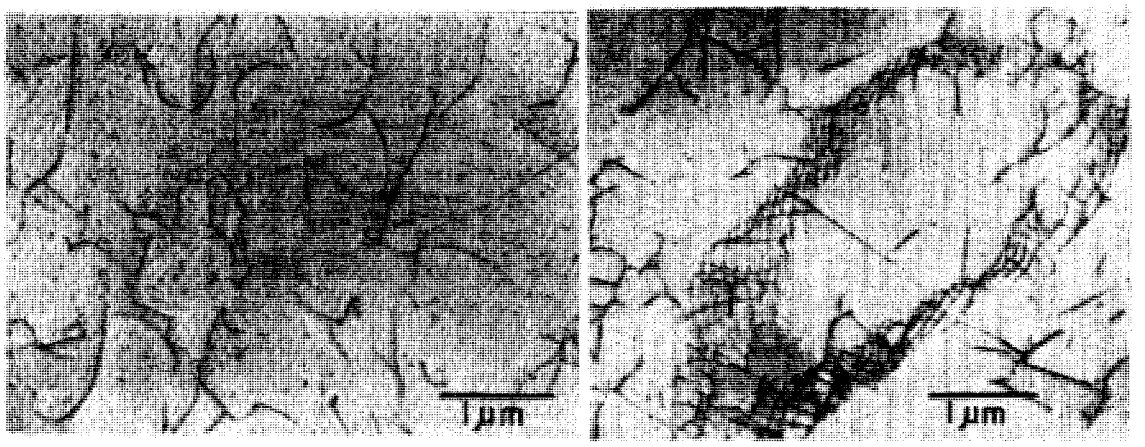

a b

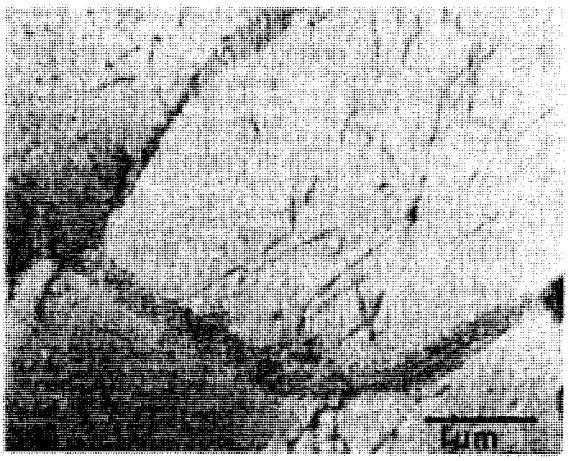

c

Fig. 2.39 Transmission electron microscopy (TEM) substructure evolution for Fe-3Si (wt%) as a function of creep strain at 643°C, 0.51 T_M and 48MPa with grain diameter 0.1mm: a) $\varepsilon = 0.008$; b) $\varepsilon = 0.038$; c): $\varepsilon = 0.141$; ×10000 [55].

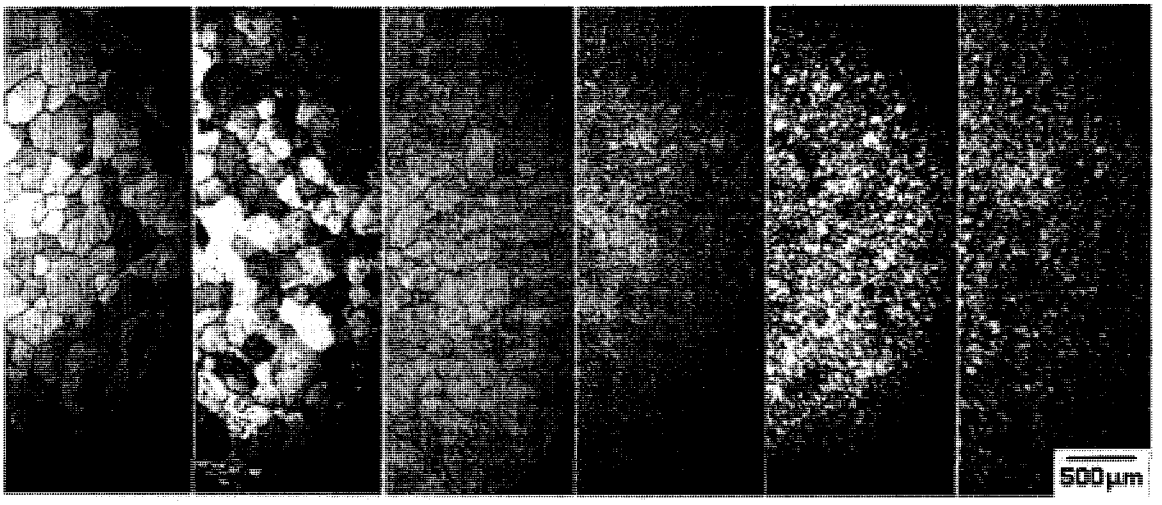

a ε=0 b 0.22 c 0.88 d 1.32 e 3.7 f 11

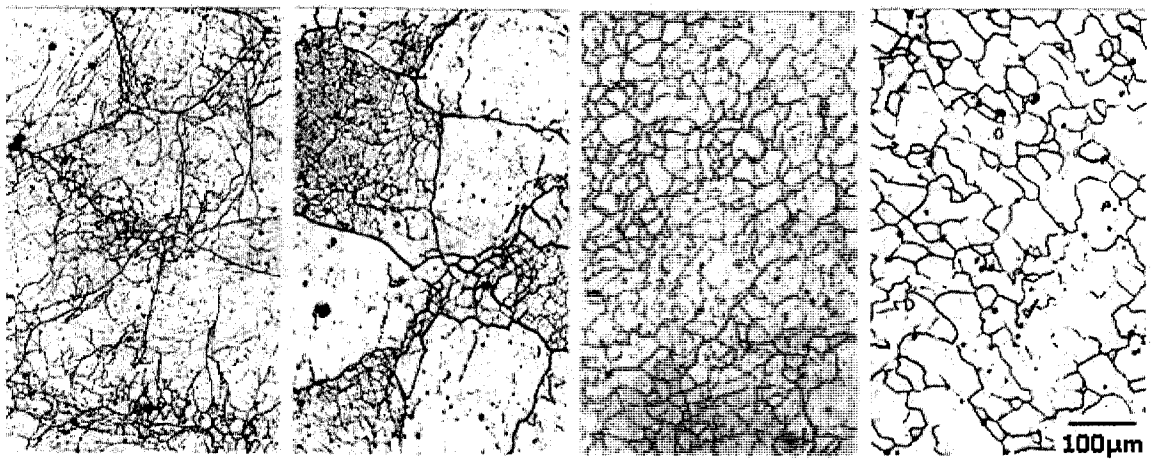

b 0.22 c 0.88 d 1.32 e 3.7

Fig. 2.40 The substructure revolution of Fe-25Cr [61] with strain at 1100°C and $\dot{\varepsilon}$=1.11s^{-1}: Upper row: a) ε=0, b) ε=0.22, c) ε=0.88, d) ε=1.32, e) ε=3.7, f) ε=11, ×18; Lower row shows the magnified microstructures of b, c, d and e of upper row, ×100 [56].

2.4.6.2 Subgrain size

Some researchers investigated the relationship between subgrain size and flow stress. For Fe-2.7Si-0.03C-0.39Mn, J-P.A.Immarigeon and Jonas [57] found that at 675°C/0.1s^{-1}, the subgrain size was 1.26μm and $\sigma = 207MPa$ when $\varepsilon = 0.53$ or subgrain size 1.48μm and $\sigma = 220MPa$ when $\varepsilon = 0.63$. C. S. Barrett et al [55] observed subgrain sizes for Fe-3Si as a function of stress with grain diameter 0.3mm as shown in Figure 2.41. A subgrain size of 10μm corresponds to a flow stress of 48MPa. Kosic et al [58, 59]

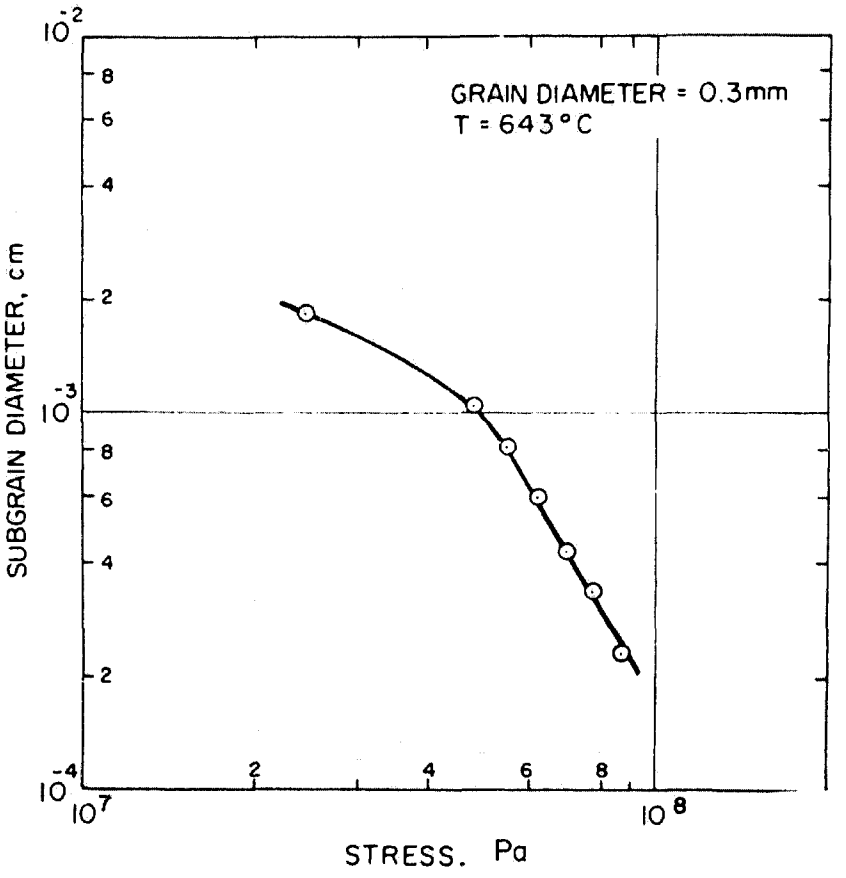

Fig. 2.41 Relationship between subgrain size and flow stress for Fe-3Si (wt%) as a function of creep strain at 643°C, 0.51 T_M and 48MPa with grain diameter 0.3mm, creep strains about 0.2 [55].

found a subgrain size of 2μm for Fe-2.8Si at 600°C/1.11s^{-1}, $\varepsilon = 0.4$. Uvira and Jonas [60] carried out a series of experiments with Fe-2.8Si-0.03C-0.45Mn and found a linear relationship between reciprocal subgrain size and flow stress as shown in Figure 2.42, which is in agreement with Equations 2.1 and 2.2. At 650°C/0.5s^{-1}, the subgrain size is 2μm when $\varepsilon = 1.6$. Current results are included for comparison. At 70MPa, current material Fe-2.7Si-0.06C has subgrain sizes of 10 and 60μm in different areas as shown by the two connecting points. At 198MPa, the material has a subgrain size of 2.9μm in some areas.

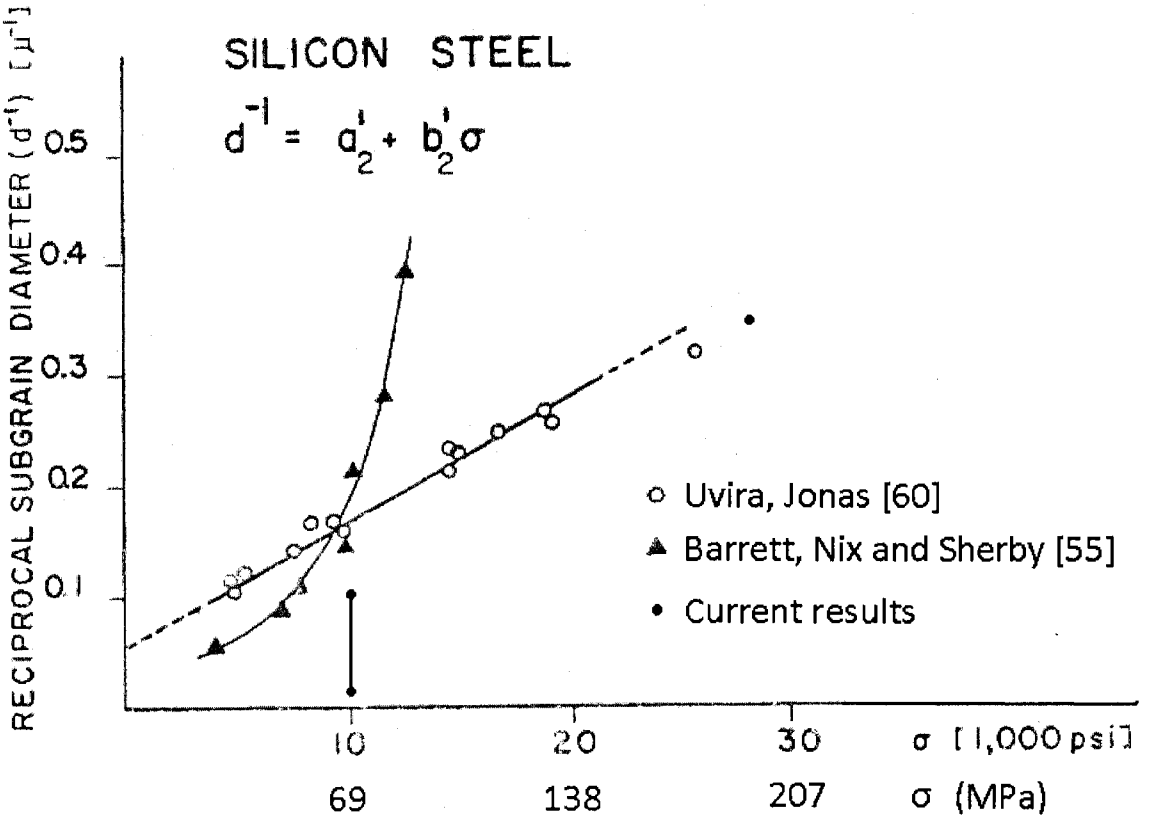

Fig. 2.42 Linear relationship between reciprocal subgrain size and flow stress for Fe-2.8Si (wt%) [60], Fe-3.0Si [55] and current results.

CHAPTER THREE

MATERIAL PREPARATION AND EXPERIMENTAL PROCEDURES

3.1 Material preparation

The Fe_3Al material was prepared by air-induction melting, and the plates were hot rolled in CANMET-Materials Technology Laboratory, Ottawa [4, 5]. Torsion specimens were machined to a gage length $L = 23\,\text{mm}$ and diameter $2r = 5.1\,\text{mm}$. Machining difficulty arose because of the hardness of the material, and about 25% of the potential specimens broke due to preexisting cracks. The silicon steels were provided by ARMCO Steel Co., and received as 155mm-thick plates, then machined to a gage length $L = 22.2\,\text{mm}$ and diameter $2r = 6.3\,\text{mm}$. Figure 3.1 exhibits the geometry of the two specimens [7].

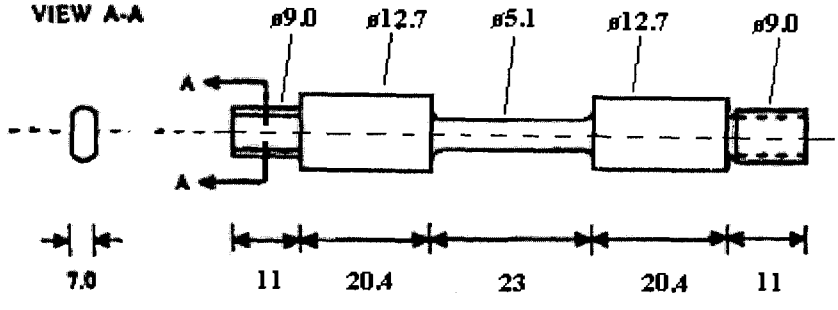

a

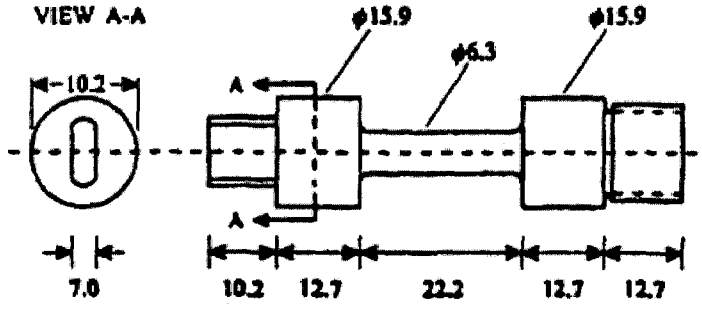

b

Fig.3.1 Geometry of torsion samples with unit mm: a) Fe_3Al, b) Fe-2.7Si.

3.2 Experimental procedure

3.2.1 Torsion tests

The specimen was deformed in a closed-loop servo-controlled hot-torsion machine shown as Figure 3.2 in Department of Mining, Metals and Materials, McGill University and heated in a four-element radiant furnace while being protected by a constant flow of argon to avoid oxidation. Figure 3.2c is the structure of the machine [61]. Fe_3Al specimens were heated up to the deformation temperature T in the range 750-950°C, and held for 30min, then deformed with the strain rate $\dot{\varepsilon}$ of either $0.01s^{-1}$, $0.1s^{-1}$ or $1s^{-1}$.As soon as deformation was completed, the specimen was extracted longitudinally from the furnace and water jet quenched immediately to retain the hot-worked microstructure. Torque and angular strain were measured, and the equivalent flow stress σ and strain rate $\dot{\varepsilon}$ were calculated with equations 3.1 and 3.2 [21]:

$$\sigma = (\Gamma / 2\pi r^3)(3 + n' + m)(\sqrt{3}) \qquad (3.1)$$

$$\dot{\varepsilon} = 2\pi r / L(rev) / \sqrt{3} \qquad (3.2)$$

Here, Γ is torque; n' is the strain-hardening coefficient, it is taken as zero at the peak stress σ_p; m is the strain rate sensitivity, its value is determined from the slopes of a $\log\Gamma$ versus $\log\dot{\varepsilon}$ plot.

Fe-2.7Si specimens were tested in either isothermal-continuous or multi-stage declining T tests. In isothermal-continuous tests, the specimens were heated up to1000°C within 10 minutes, held for 5 minutes, and then cooled down to the deformation T in the range 600~900°C, held for 5 minutes and deformed with $\dot{\varepsilon}$ of $0.1s^{-1}$,$1s^{-1}$ or $5s^{-1}$. In multi-stage tests, some samples were heated up to 900°C within 10 minutes, held for 5 minutes

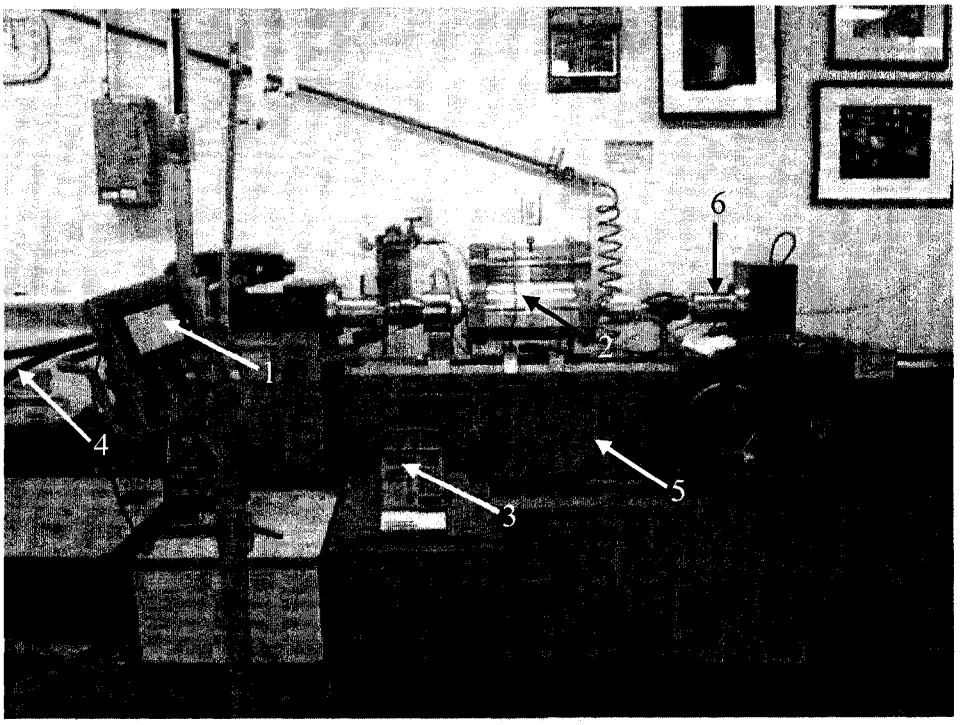

a

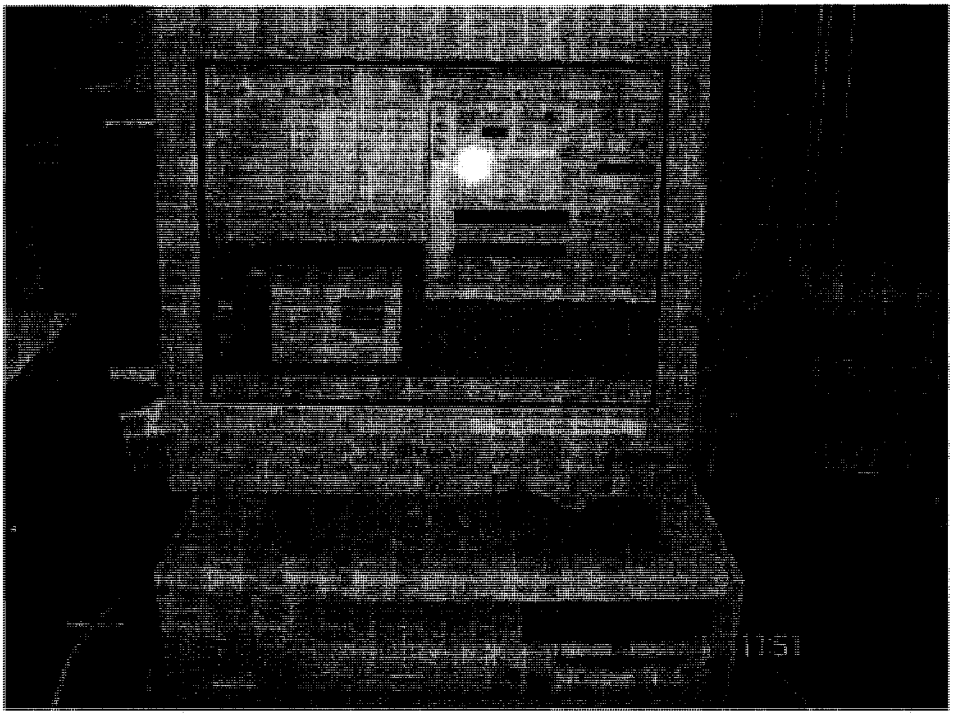

b

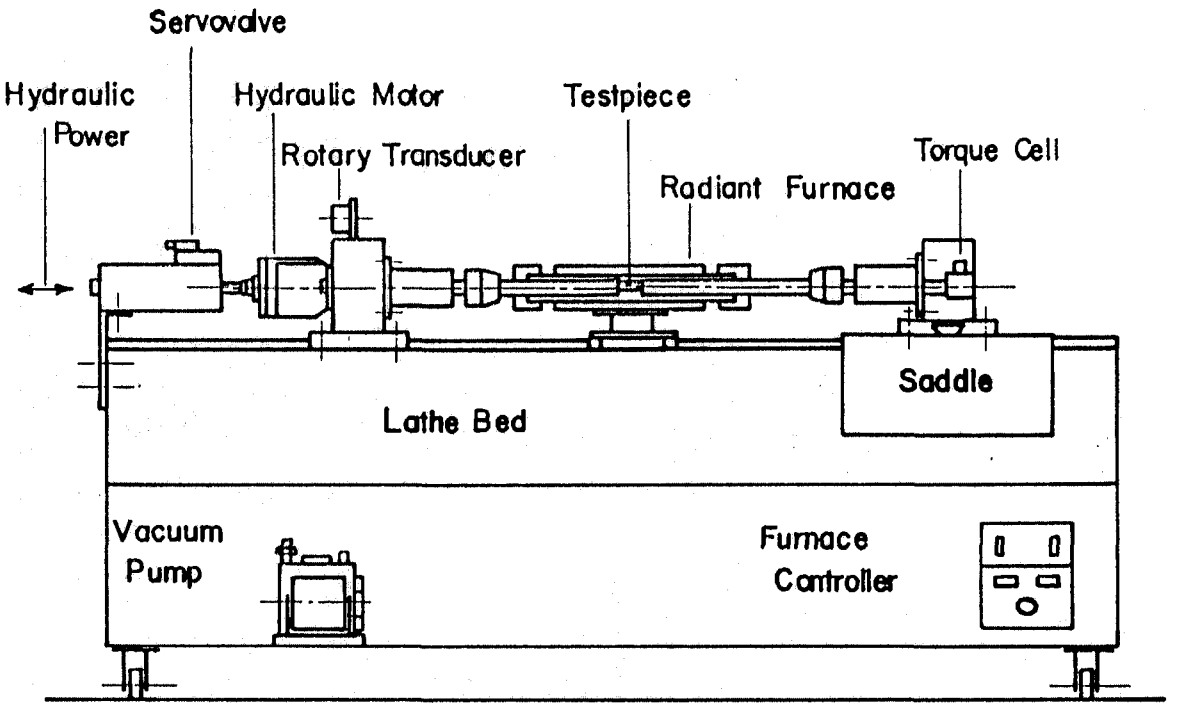

c

Fig. 3.2 Torsion machine. a) 1: Remote control station; 2: Radiant furnace; 3: Temperature programmer; 4: Hydrolic motor; 5: Lathe bed frame; 6: Load cell; b) Deformation parameter programmer; c) The schematic structure [61].

and deformed with $\dot{\varepsilon}$ of $0.1s^{-1}$ or $1s^{-1}$ as T was decreased to 600°C in equal steps over17 passes. Some specimens were heated up to 1000°C within 10min, then held and tested in the range of 1000°C~700°C. The pass strain was either 0.2 or 0.3, and the interval between two neighboring stages either 20s or 40s.

3.2.2 Compression tests

The shoulder of the torsion specimens were cut with ISOMET™ 11-1180 Low Speed Saw by Buehler Ltd. and machined to compression specimens shown as Figure 3.3. They were mounted in a compression machine shown as Figure 3.4 and heated in a

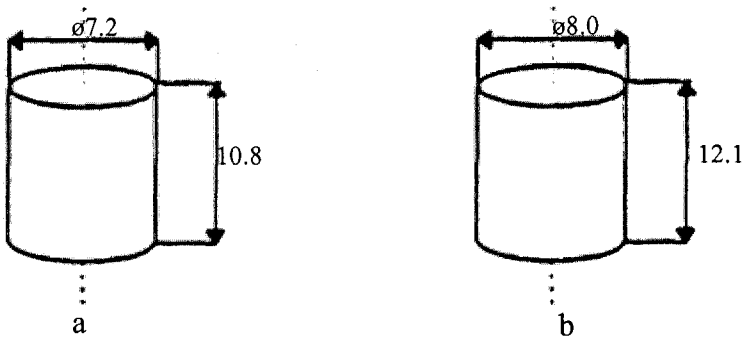

Fig. 3.3 Geometry of compression samples with unit mm: a) Fe_3Al; b) Fe-2.7Si.

furnace while being protected by a constant flow of argon. Fe_3Al samples were heated up to 1000°C and cooled down to the deformation T in the range 830~1050°C, and held for 15min, then compressed until maximum strain $\varepsilon_m = 0.5$ with $\dot{\varepsilon}$ of either $0.01s^{-1}$, $0.1s^{-1}$ or $1s^{-1}$. The Fe-2.7Si specimens were heated up to1000°C within 10 minutes, held for 5 minutes, and then cooled down to the deformation T in the range 600~900°C, then held for 5 minutes and compressed until $\varepsilon_m = 0.5$ with $\dot{\varepsilon}$ $1s^{-1}$.

3.2.3 Optical microscopy

The gage sections of the deformed specimens were cut, mounted in PR-22 PNEUMATIC MOUNTING PRESS by LECO Corporation, ground with LUNN MAJOR from STRUERS Corporation of Denmark and polished with VP-150 Grinder/Polisher from LECO Corporation. Their cracks were observed with BX51M OLYMPUS Metallurgical Microscopy. After that, the Fe_3Al specimen deformed at 830°C/$0.01s^{-1}$ was etched in a solution of 20%HNO_3 +20%HCl +60%H_2O, the specimen at 950°C/$0.01s^{-1}$ and 950°C/$0.1s^{-1}$ in a solution of 30% HNO_3 + 20%HCl +50%H_2O, those at 750°C/$0.01s^{-1}$, 830°C/$0.1s^{-1}$, and 830°C/$1s^{-1}$ in 50%CH_3COOH + 30%HNO_3 +20%HCl. The isothermal-continuous specimens of Fe-2.7Si were etched in the solution of 10%HNO3 + 20%HCl

a

b

Fig.3.4 Compression machine. a) 1: remote control station; 2: the furnace; temperature and deformation parameter programmers not included; b) the red-hot furnace open after deformation, 3: sample sticking to the punch. inside .

+30%Methonal +40%Glycerol [62]. The specimens of multi-stage tests were etched in the same solution or a solution of 30%HNO3 + 20%HCl +50%H_2O.

The compression specimens were cut into halves, ground and polished, and then their cracks were observed optically.

Footnote:

For three months in 1996 and 1999, Mohiedeen Abdel-Rahman, a visiting professor from Minia University, Egypt worked with Prof. H. J. McQueen on:

1. Isothermal-continuous torsion tests of Fe-2.7Si-0.06C [9]. The large disks of data that were left are not currently readable by available machines; The hard copy of flow curves to be adopted in this thesis have different stress scales from the published ones [9];
2. Multi-stage torsion simulation results were also left in the hard copy mentioned above as two sets of flow curves with totally different stress scales under identical deformation conditions.

The data were checked by:

1. Recalculation from 5 sets of data Mohiedeen sent from Egypt;
2. Compression tests on shoulder parts of torsion specimens.

The analysis gave consistent results that agreed with one set of isothermal-continuous and multi-stage test results in the hard copy left by Mohiedeen, and the new values were consistent with the published results of Akta [10], Calvillo [11] and Uvira [12].

CHAPTER FOUR

EXPERIMENTAL RESULTS

4.1 Fe_3Al

4.1.1 Torsion flow curves

Figure 4.1 shows the representative torsion flow curves of Fe_3Al. The three specimens deformed at $830^{\circ}C/0.01s^{-1}$, $950^{\circ}C/0.1s^{-1}$ and $950^{\circ}C/0.01s^{-1}$ exhibit strain hardening to a plateau, which is typical of the restoration mechanism dynamic recovery (DRV). The specimen deformed at $830^{\circ}C/0.01s^{-1}$ reached a strain of 20 but did not break implying that the material was very ductile; the flow stress remained constant at 37MPa over the plateau. The specimen deformed at $950^{\circ}C/0.01s^{-1}$ broke around a strain of 16 and the steady stress of 26MPa, being very ductile under this condition. The sample deformed at $950^{\circ}C/0.1s^{-1}$ broke around a strain of 6 with a plateau stress of 27MPa. The three specimens deformed at $750^{\circ}C/0.01s^{-1}$, $830^{\circ}C/0.1s^{-1}$ and $830^{\circ}C$ $/1s^{-1}$ show sharp strain hardening to a peak stress and drastic drop because of sample failure at randomly low strain. Figure 4.2 shows the ductility variation with stress and temperature-compensated strain rate Z. The specimens with stress greater than 90MPa ($log\ Z>16$) are very brittle while those with stress lower than 40MPa ($logZ\leq 16$) are very ductile ($\varepsilon_f>6$). This pattern of very low ductility and fairly random but high ductility indicate that preexisting defects caused the failure of the specimens. The fact that around 25% of the specimens broke on machining the Fe_3Al plate confirms the presence of cracks.

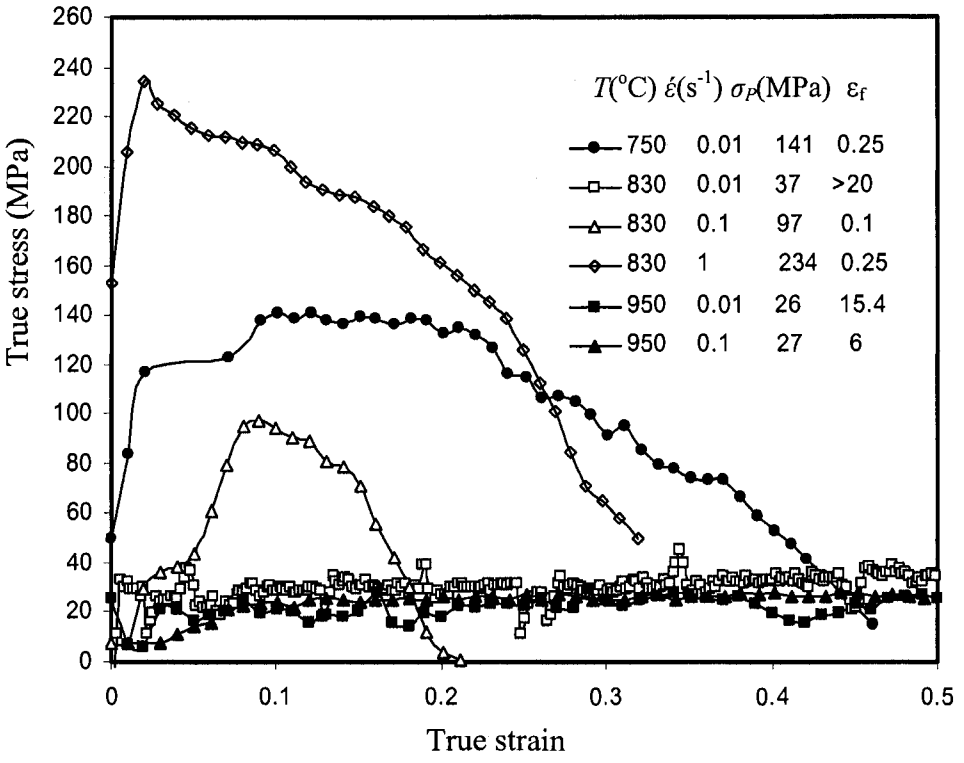

Fig.4.1 Stress-strain curve of Fe_3Al in torsion tests at different T and $\dot{\varepsilon}$.

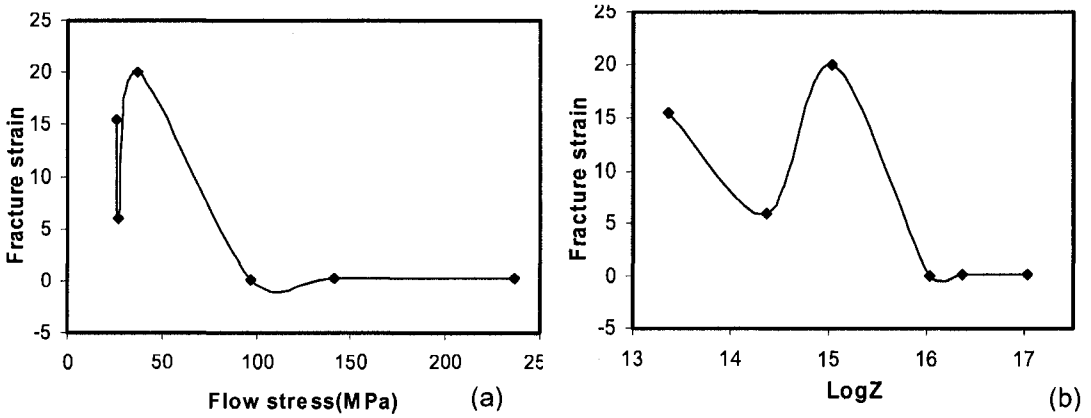

Fig.4.2 For Fe_3Al, the relationships between fracture strain and:

a) flow stress, b) logZ.

4.1.2 Torsion micrograph

The torsion specimens were examined normal to the radius close to the surface (~$0.8r_{gage}$). Preexisting cracks were observed, many being quite broad. Many contain

second-phase particles that are light grey to white in comparison to the shining metal; some particles were pulled out of the cracks by polishing. Some cracks appear triangular as if cavities at triple junctions; some are curved and irregular as if following grain boundaries (GB) or dendrites.

In Figure 4.3 of the sample at $830^{\circ}C/0.01s^{-1}$, cracks were developed aligned with GB in the shear plane almost perpendicular to the axis of the sample. Figure 4.3a demonstrates an extremely irregular surface as if regions on the scale of several grains had been extruded outwards while other regions had deep depressions. A crack related to a GB developed across the whole surface but did not propagate deeply enough to cause fracture. Figure 4.3b shows second-phase particles inside a crack with an ejected particle having caused a big scratch during polishing. A crack about 45° to the axis (Figure 4.3c) is probably related to a GB with a triangular cavity from a second-phase particle. Several round holes (Figure 4.3d) probably resulted from decohesion of hard second-phase particles lost during polishing.

Specimens deformed at $950^{\circ}C/0.01s^{-1}$ and $950^{\circ}C/0.1s^{-1}$ show similar features to those of the specimen deformed at $830^{\circ}C/0.01s^{-1}$. In the sample deformed at $950^{\circ}C/0.01s^{-1}$ (Figure 4.4a), surface indentations developed along GBs which tended to be parallel at 80° to the axis. Arrow 1 shows a big triangular hole probably related to a particle; the roughness along the cracks indicates second-phase particles along GBs. Figure 4.4b shows second-phase particles inside several holes; some were pulled out during polishing. In Figure 4.5 for $950^{\circ}C/0.1s^{-1}$, cracks developed at the surface of the specimen, some parallel to the GB. Figure 4.5b shows severe cracks opened up by the reduced stress at the transition from gage section to shoulder.

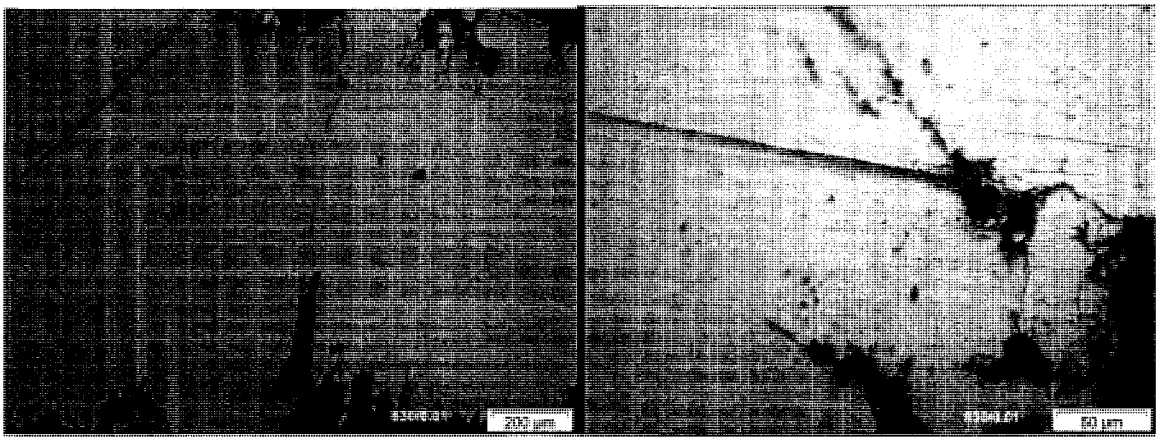

a b

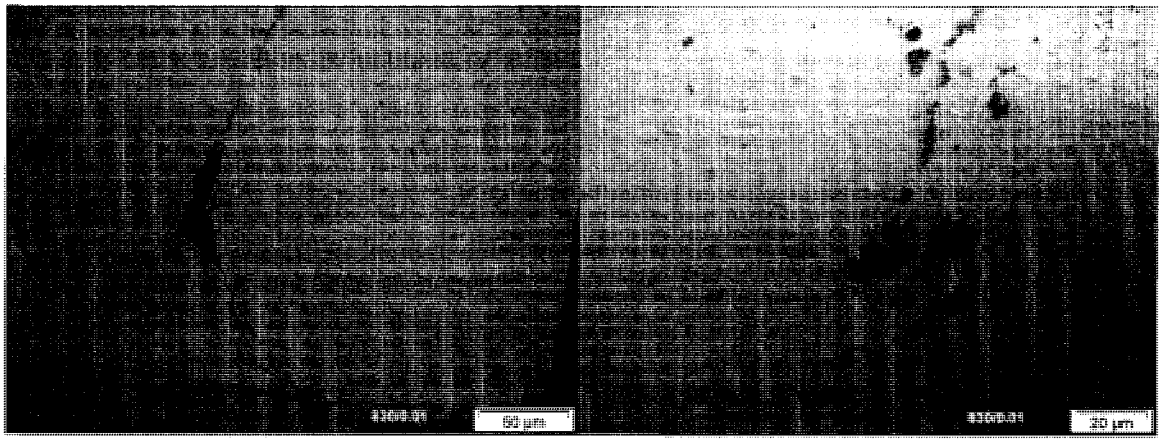

c d

Fig. 4.3 Torsion cracks of Fe_3Al deformed at 830°C, $0.01s^{-1}$, ε_f >20: a) very rough surface indicating deep indentations related to GBs, ×50; b) second-phase particles inside a crack, ×250; c) a crack connected with a large triangular cavity, ×250; d) round holes from the decohesion of non-deformable particles during deformation, ×500.

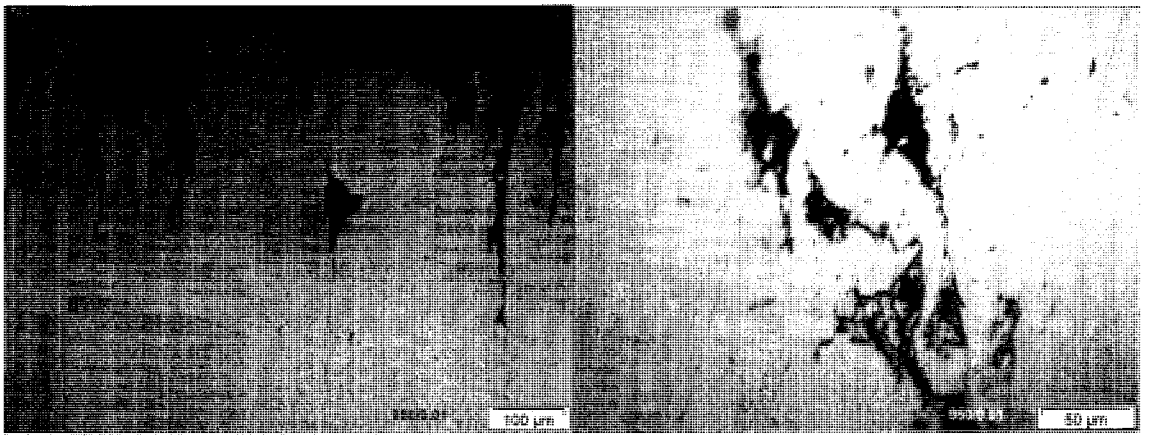

a b

Fig. 4.4 Torsion cracks of Fe_3Al deformed at 950°C, $0.01s^{-1}$, ε_f=15.4. a) indentations or surface marks related to GBs which tend to be parallel at 80° to the axis; the irregularity along the cracks indicates second-phase particles along GBs; area 1: particle, ×100; b) second-phase particles retained in some cracks, ×250.

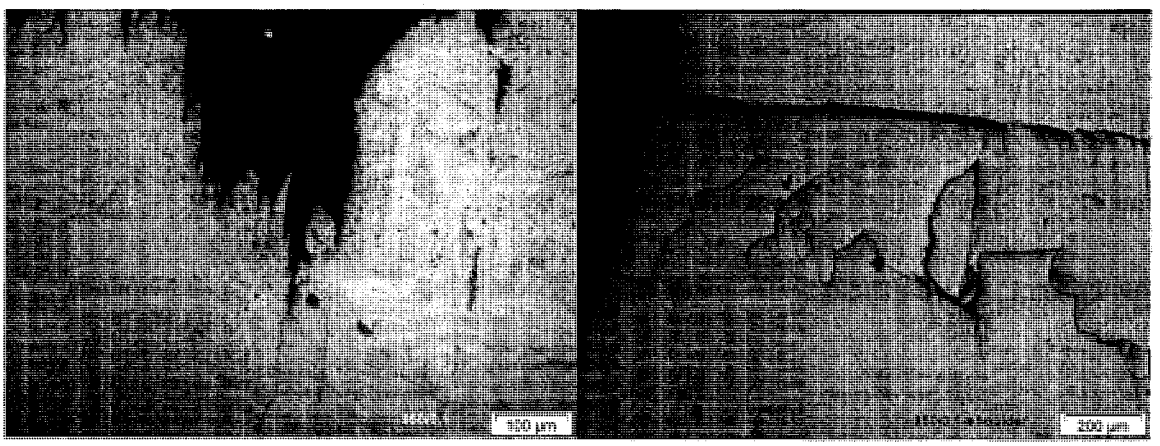

a b

Fig.4.5 Torsion cracks of Fe_3Al deformed at 950°C, $0.1s^{-1}$, ε_f=6. a) cracks at the surface of the specimen or parallel to GBs inside the sample, ×100; b) short serious cracks opened by reduced stress near the shoulder, ×50.

When specimens were deformed at 830°C/0.01s^{-1}, 950°C/0.1s^{-1} and 950°C/0.01s^{-1}, cracks propagated slowly reducing the stress, and the samples failed at high random strains. When specimens were deformed at 750°C/0.01s^{-1}, 830°C/0.1s^{-1} and 830°C/1s^{-1}, comparatively high stresses developed rapidly. Some long cracks initiated and linked up along GBs quickly shown as Figure 4.6, Figure 4.7 and Figure 4.8, causing very low ductility.

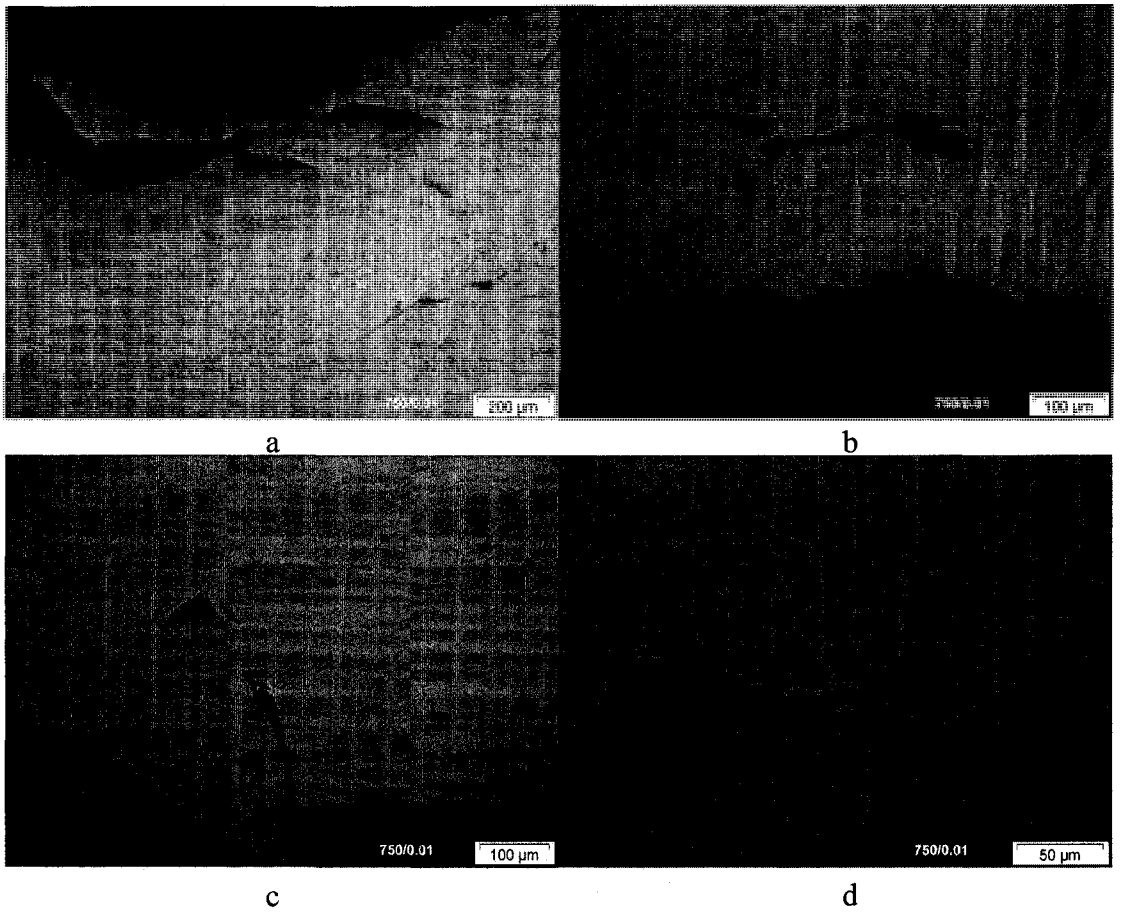

a b c d

Fig. 4.6 Torsion cracks at 750°C, 0.01s^{-1}, ε_f=0.25.a) cracks at the edge of the sample, ×50; b) a complex crack partially parallel to the axis linked with parts at 45° to the edge, ×100; c) a complex crack partially opened up linked with a length closed, about 45° to the edge, second-phase particles inside the crack, ×100; d) crack at a small angle to the edge with particles inside, ×250.

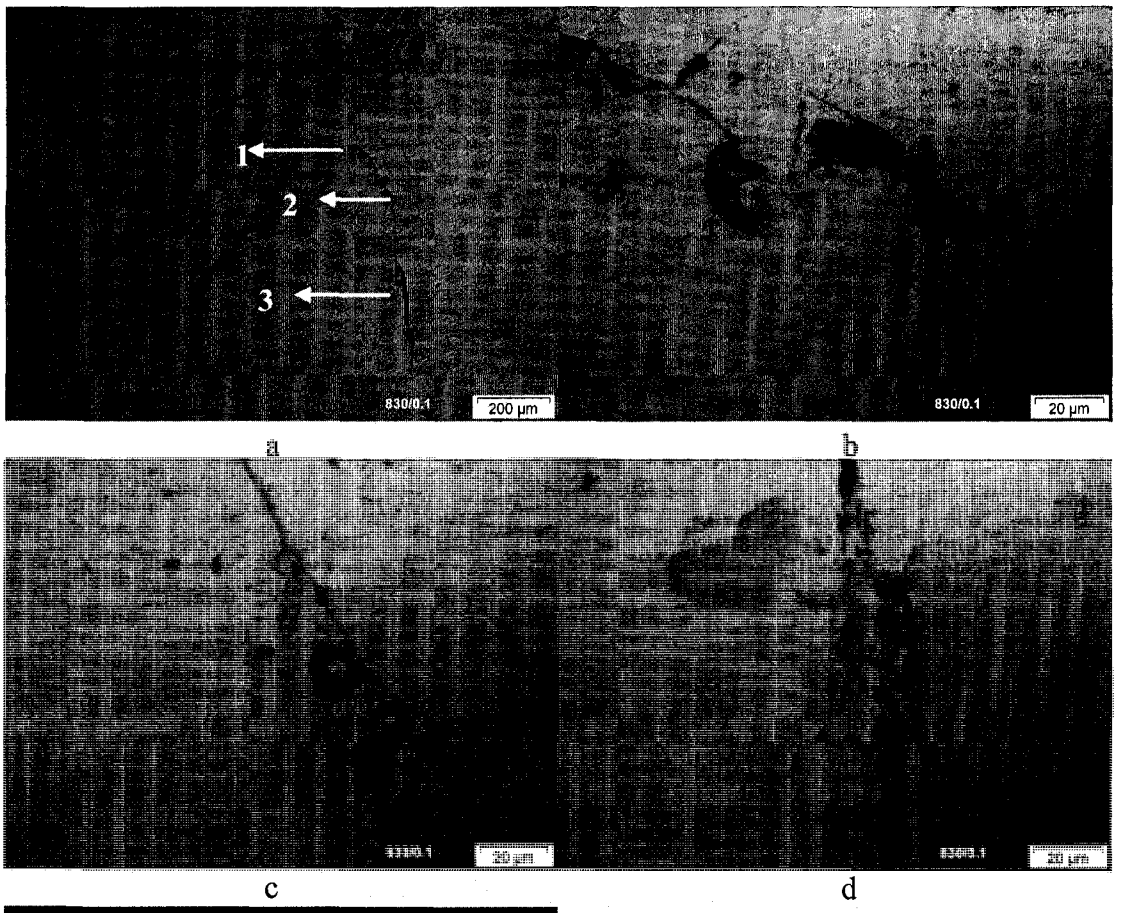

Fig. 4.7 Torsion cracks at 830°C, $0.1s^{-1}$. ε_f=0.1.a) a complex crack initiating failure, ×50;

Fig. 4.7b) image of arrow 1 in a) showing second-phase particles inside a hole, ×500; c) image of arrow 2 in a) showing second-phase particles in the hole, ×500; d) image of arrow 3 in a) showing metals in a hole with other phases mixed in, ×500; e) a smooth crack causing failure, ×50.

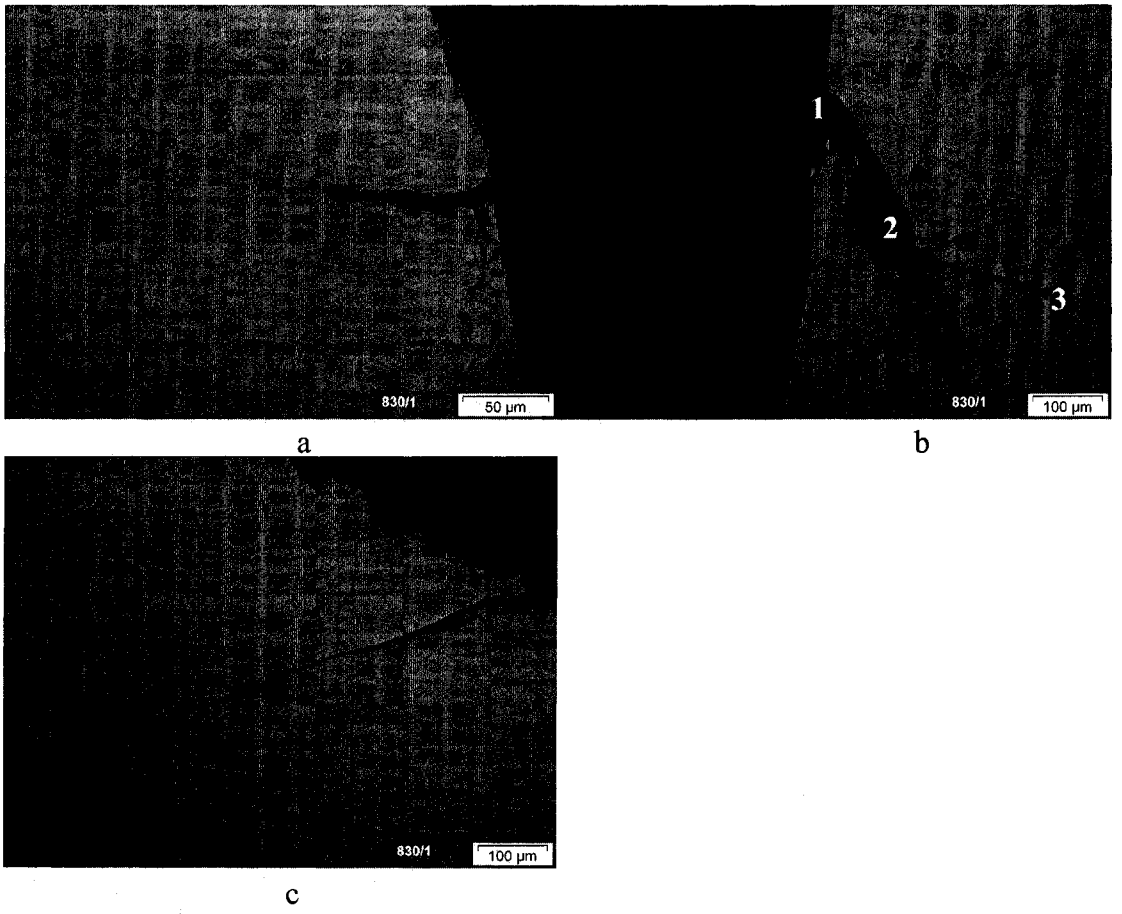

Fig. 4.8 Torsion cracks at 830°C, $1s^{-1}$, ε_f=0.25. a) crack with one branch parallel and another perpendicular to the axis, ×250; b) an open crack, 1)+2) large trunks of second phase; 3) second-phase sticking out and fixing in the surface causing big scratches, ×100; c) branching crack, ×100.

4.1.3 Compression tests

Figure 4.9 shows the compression flow curves in the range of 830~1050°C with the strain rate of either $0.01s^{-1}$, $0.1s^{-1}$ or $1s^{-1}$ to a maximum strain 0.5. The curves undergo strain hardening and reach a plateau, implying the effect of DRV. In all the tests, the flow stress increases with increasing $\dot{\varepsilon}$ and T. In compression specimens machined from the shoulder parts of torsion specimens, some hoop cracks appear on opposite ends of one

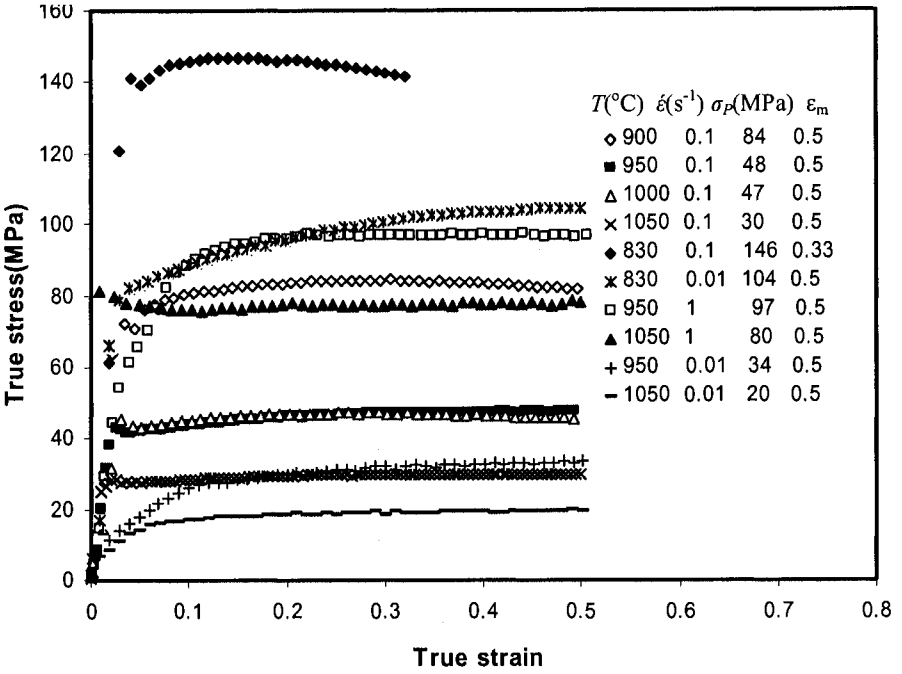

Fig. 4.9 Stress-strain curve of Fe_3Al in compression tests with ε_m= 0.5.

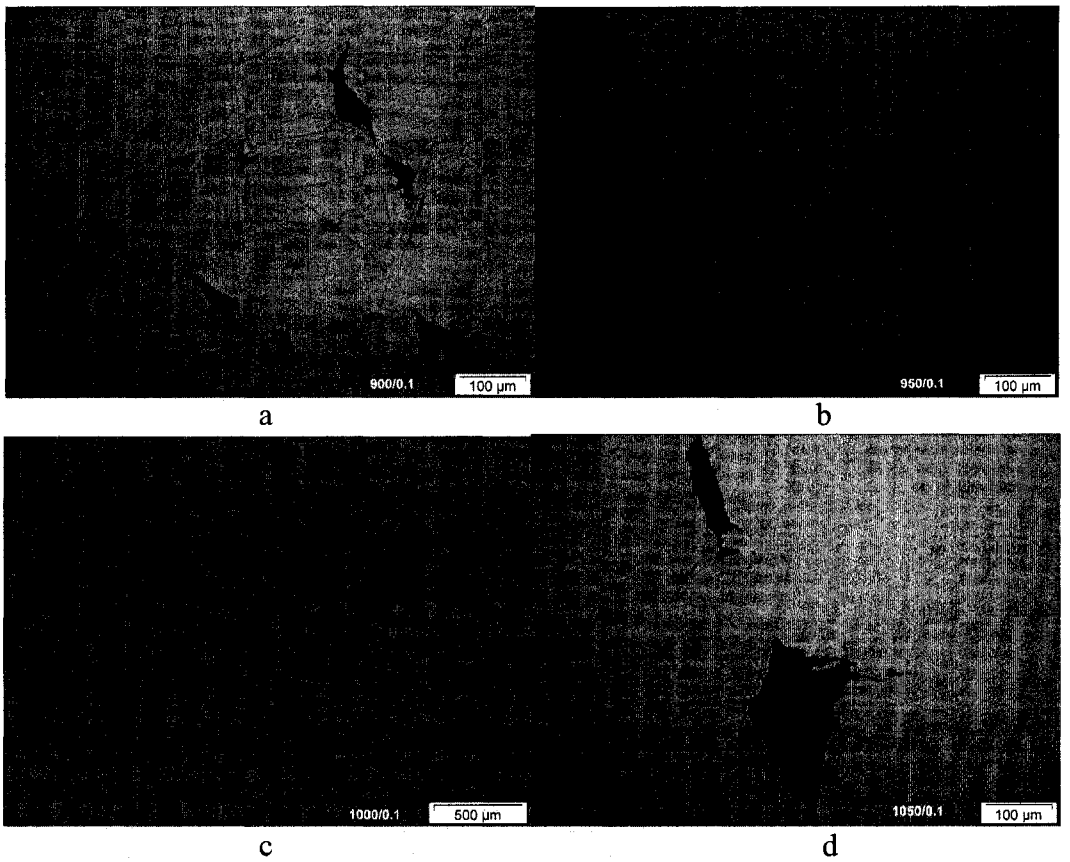

a b

c d

Fig. 4.10 Compression cracks of Fe_3Al. a) at 900°C, 0.1s^{-1}, ×100; b) at 950°C, 0.1s^{-1}, ×100; c) at 1000°C, 0.1s^{-1}, ×25; d) at 1050°C, 0.1s^{-1}, ×100.

diameter parallel to the axis, but composed of segments at 45° to axis. Inside the samples shown as Figure 4.10, a few cracks appear smaller than those in torsion specimens with fewer second-phase particles staying inside. Maybe compression closed up some preexisting cracks.

4.2 Fe-2.7Si ferritic steel

4.2.1 Isothermal-continuous tests

4.2.1.1 Flow curves

The torsion flow curves of Fe-2.7Si-0.06C specimens based on the data provided by M. Abdel- Rahman (T.AR.) [9] (Footnote in page 55) are shown in Figure 4.11. At 600 and 700°C (except 700°C/0.1s^{-1}), the flow stresses increase to a sharp peak because of the effect of solute drag followed by a rapid decline to fracture. At 800 and 900 °C, as dislocation mobility increases due to reduced solute drag; the flow stress increases to only a low peak followed by a gradual decrease to a plateau. Figure 4.12a exhibits the flow curves from original torque-twist data of Abdel-Rahman but calculated by the author (T.Ani.AR.). The peak stress σ_P agrees fairly well with T.AR. data except that for 700°C/1s^{-1}. Compression curves (C.Ani) with $\dot{\varepsilon}$=1s^{-1} in Figure 4.12b exhibit stresses close to those of torsion with $\dot{\varepsilon}$=1s^{-1}. Strain hardening followed by a plateau indicates that the principal restoration mechanism is DRV; the slight decline of stress at low T indicates the effect of deformation heating. Figure 4.13 exhibits the variation of peak stress σ_P with T and $\dot{\varepsilon}$ based on Figure 4.11 and 4.12. σ_P decreases with the increase of T or decrease of $\dot{\varepsilon}$. The compression stresses at 1s^{-1} agree well with those of Abdel-Rahman and almost superimpose on the recalculated torsion stresses. The σ_P values at different T when $\dot{\varepsilon}$=1s^{-1} were selected for calculating relative softening and relative reduction of stress in multi-

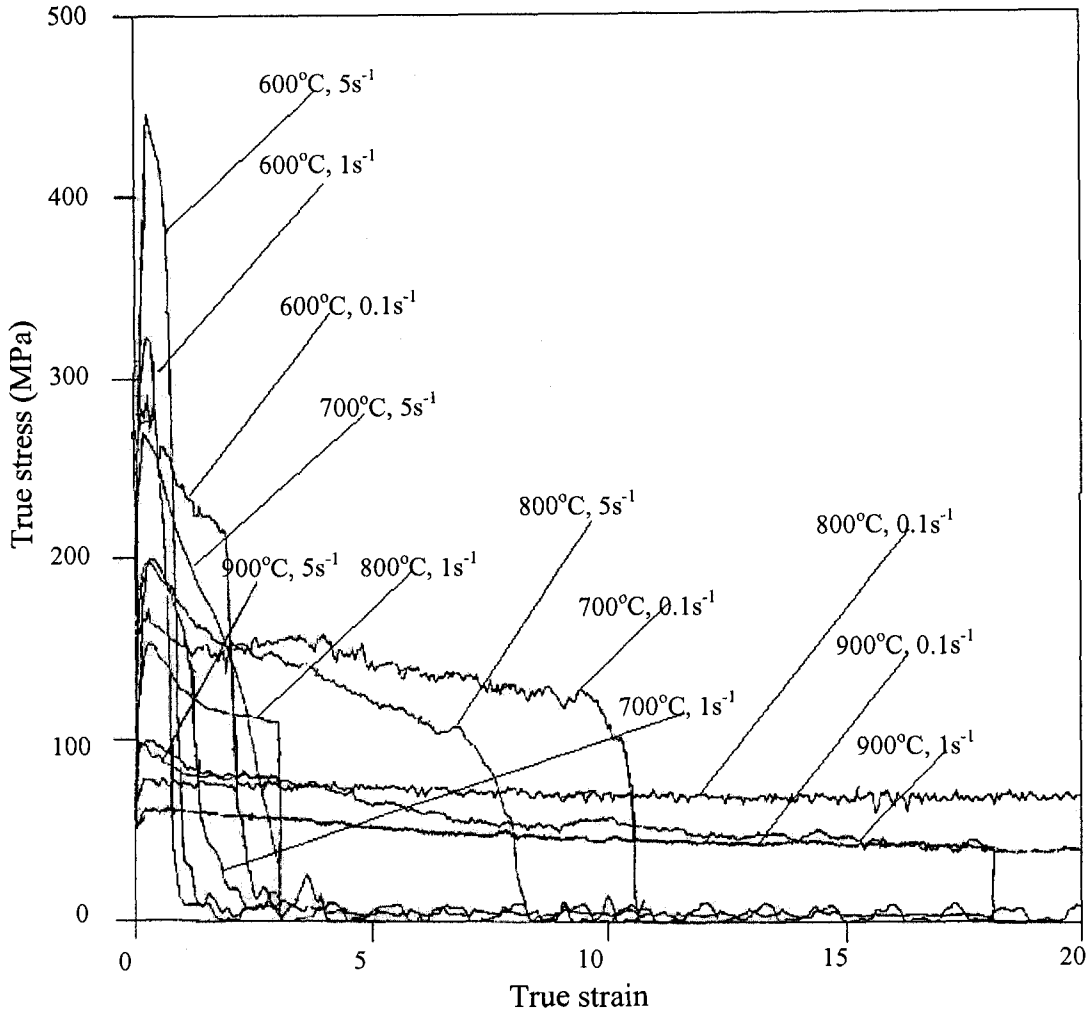

Fig. 4.11 Flow curves of Fe-2.7Si-0.06C specimens in isothermal-continuous tests of Abdel-Rahman.

stage tests.

4.2.1.2 Constitutive analysis

Constitutive analysis is always based on Equation 2.1:

$$Z = \dot{\varepsilon} \exp(Q_{HW} / RT) = A(\sinh \alpha\sigma_s)^n \qquad (2.1)$$

Figure 4.14 shows the constitutive results of current material. The value of α is taken as 0.017MPa^{-1}. Figure 4.14a shows the relationship between Log ε̇ and Log (sinhασ). At a

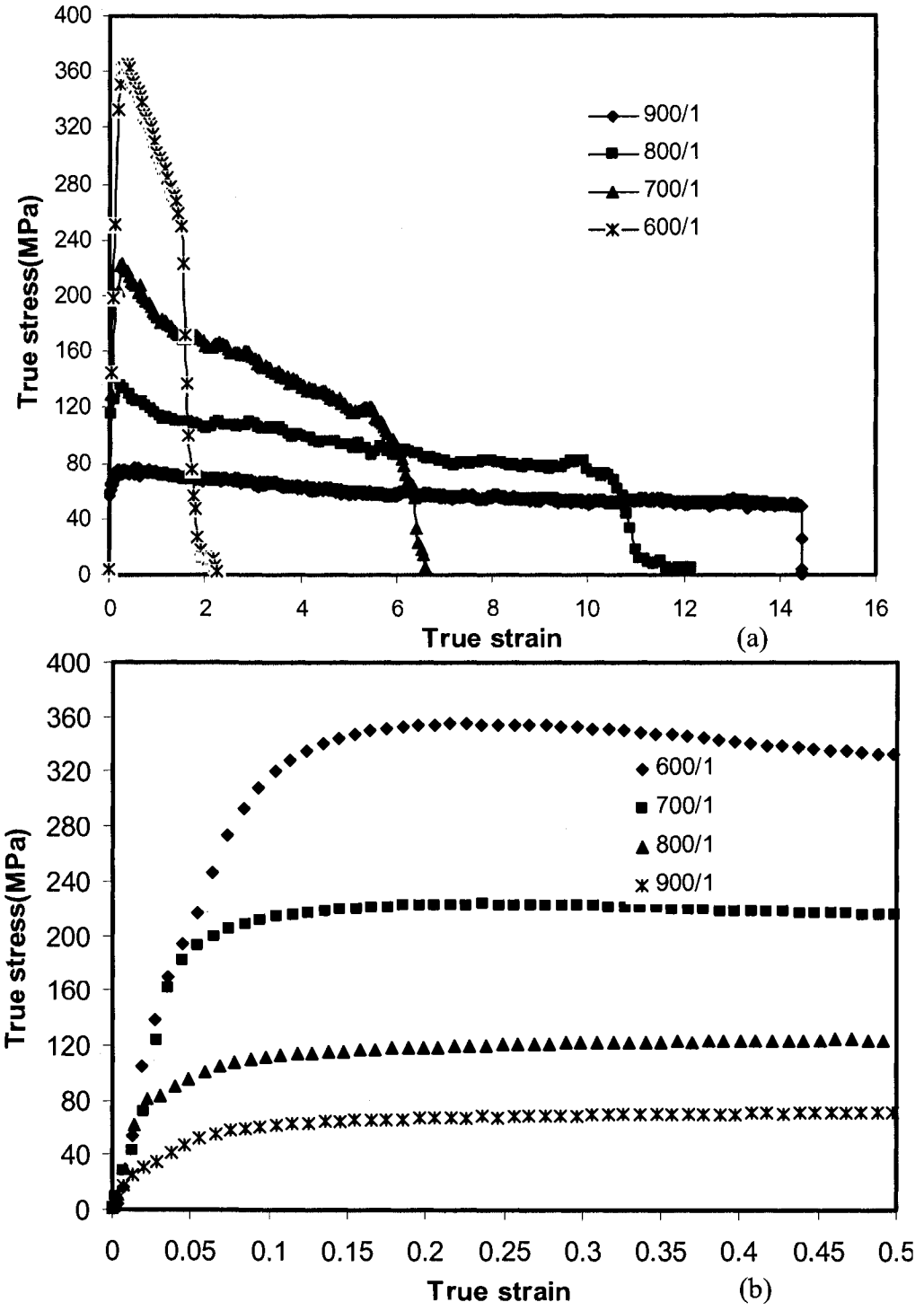

Fig. 4.12 Flow curves of Fe-2.7Si-0.06C specimens with $\dot{\varepsilon}=1s^{-1}$. a) Torsion curves calculated from the data of Abdel-Rahman; b) Current compression curves with ε strain magnified 30 times. The peaks appear broad due to the magnified strain scale. 600/1 refers to $600^{o}C/1s^{-1}$.

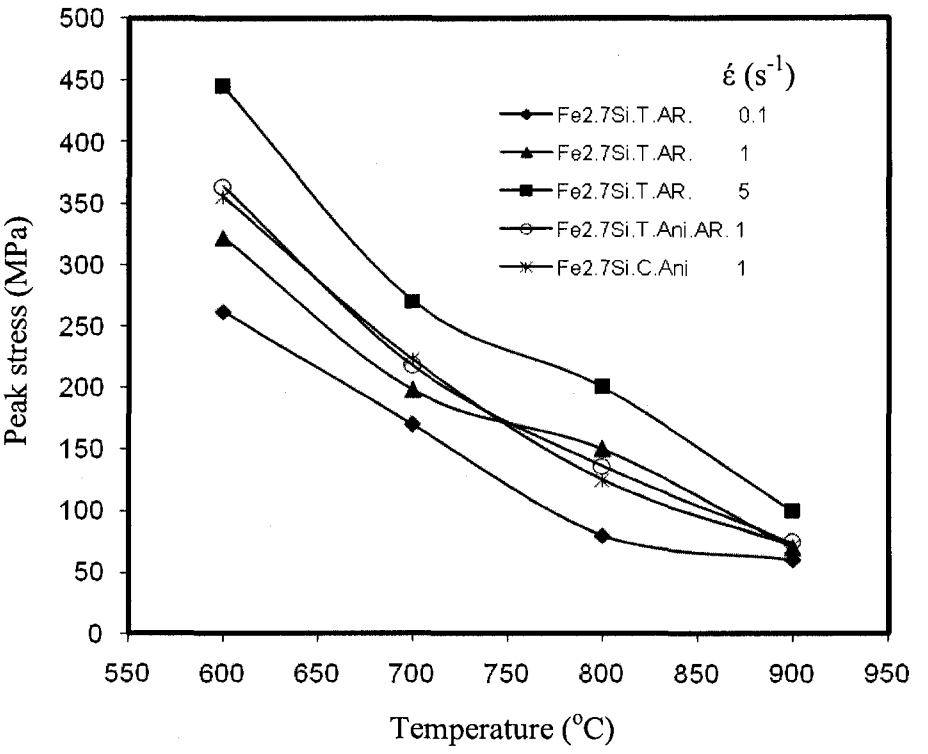

Fig. 4.13 The variation of peak stress σ_P of Fe-2.7Si-0.06C with T and έ.

constant T, the values of σ_P increase with decrease of έ, which agrees with Figure 4.11, 4.12 and 4.13. The recalculated torsion data points for $1s^{-1}$ (T.Ani.AR.) and compression points for $1s^{-1}$ (C.Ani) are located very close to the original torsion points (T.AR.) at the same T. All the constant T lines (Figure 4.14a) are almost parallel, and the average slope n is 2.0. Figure 4.14b shows the relationship between Log (sinhασ) and 1000/T. At a constant έ, the values of σ_P decrease with the increase of T, which agrees with Figure 4.11. The lines are almost parallel and the average slope s is 6.5, and Q_{HW} is calculated to be 247kJ/mol. Notably, the recalculated torsion curve and compression curve are tightly close to each other, agreeing with Figure 4.13.

Figure 4.14c shows the relationship between Log Z and Log (sinhασ). Through

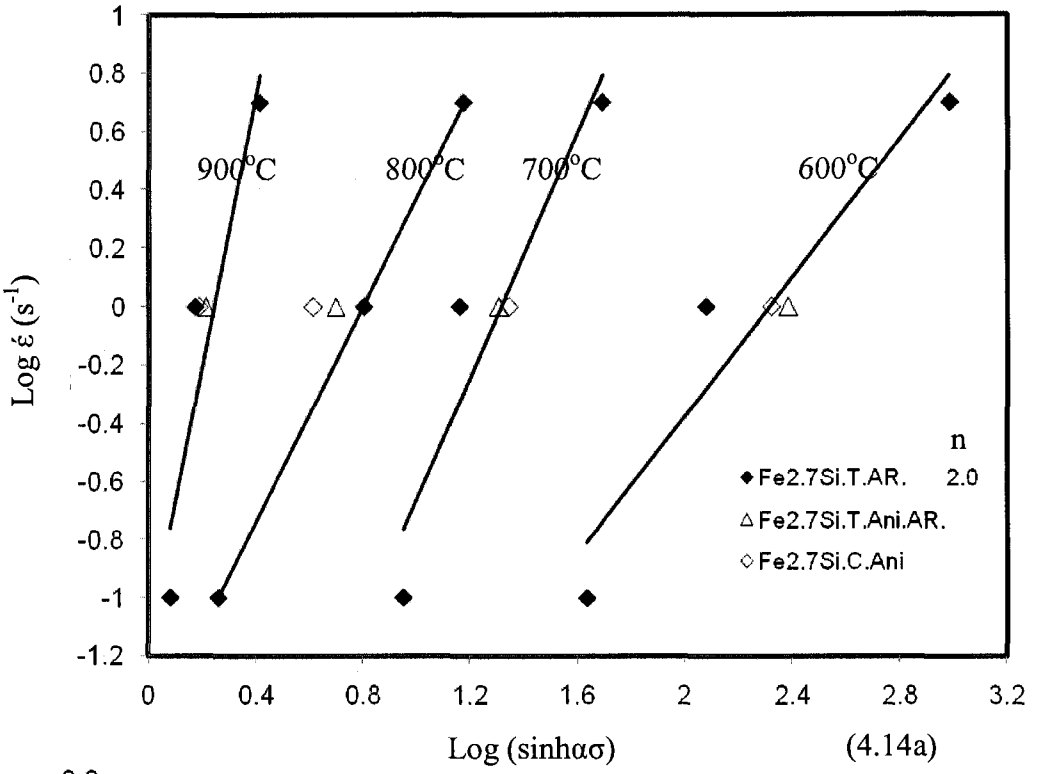
900°C
800°C
700°C
600°C
n
Fe2.7Si.T.AR. 2.0
Fe2.7Si.T.Ani.AR.
Fe2.7Si.C.Ani
Log ε̇ (s⁻¹)
Log (sinhασ)

(4.14a)

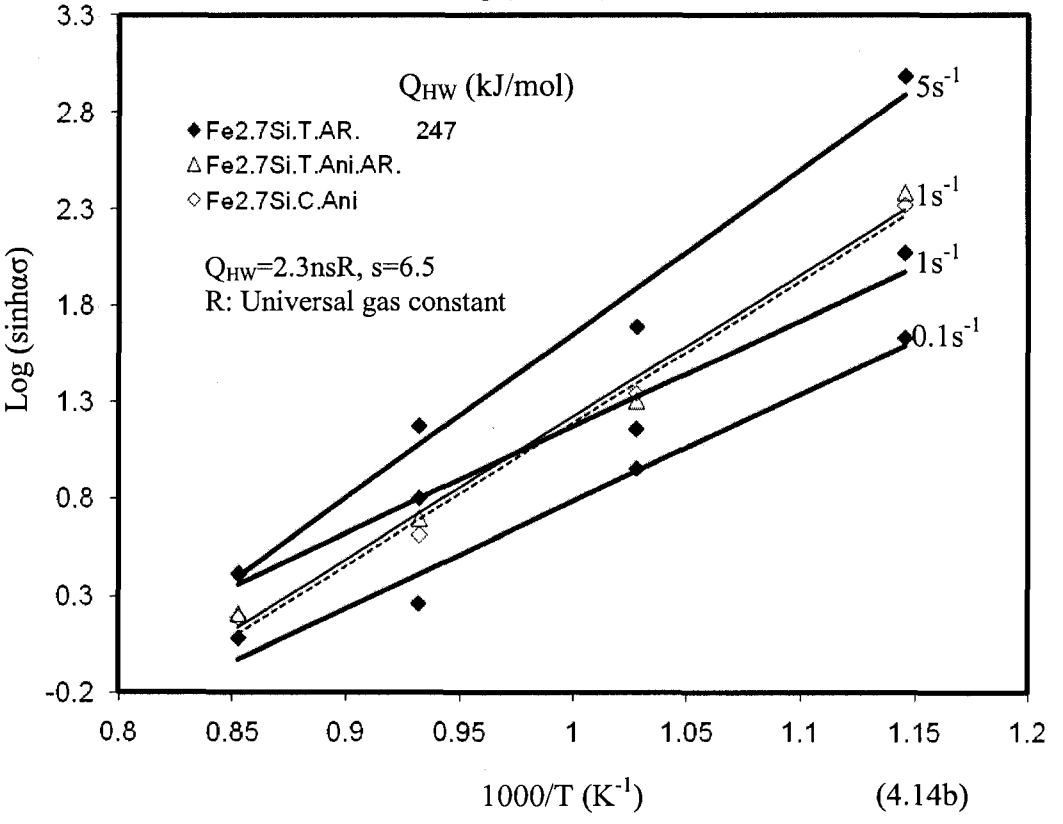
Q_HW (kJ/mol)
Fe2.7Si.T.AR. 247
Fe2.7Si.T.Ani.AR.
Fe2.7Si.C.Ani
Q_HW=2.3nsR, s=6.5
R: Universal gas constant
5s⁻¹
1s⁻¹
1s⁻¹
0.1s⁻¹
Log (sinhασ)
1000/T (K⁻¹)

(4.14b)

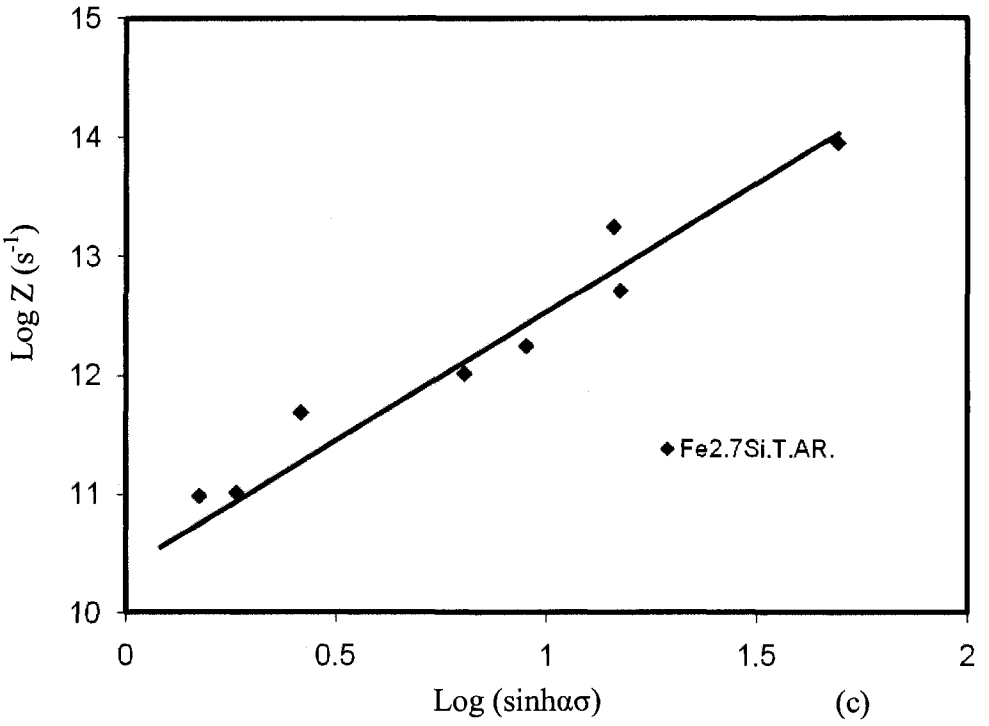

Fig. 4.14 Constitutive analysis of current material: a) Log ε̇ versus Log (sinhασ); b) Log (sinhασ) versus 1000/T; c) Log Z versus Log (sinhασ).

Equation 2.1 with the derived constitutive constants, the peak stress σ_p for any deformation condition can be calculated. Log A is 10.4.

4.2.1.3 Microstructure

After isothermal-continuous deformation of Fe-2.7Si-0.06C, the gage sections and shoulders of the specimens were cut at a depth of 0.9 R from the center of the specimens, polished and etched. Their optical micrographs are presented with torsion axes horizontal. Some published microstructures of Fe-3Si (wt%) [55] and Fe-25Cr (wt%) [56] are used to compare with current micrographs.

Figure 4.15 shows the microstructure of the specimen deformed at 600°C/1s^{-1}. In gage section in Figure 4.15a, the grains are elongated and distorted at about 60° to the axis

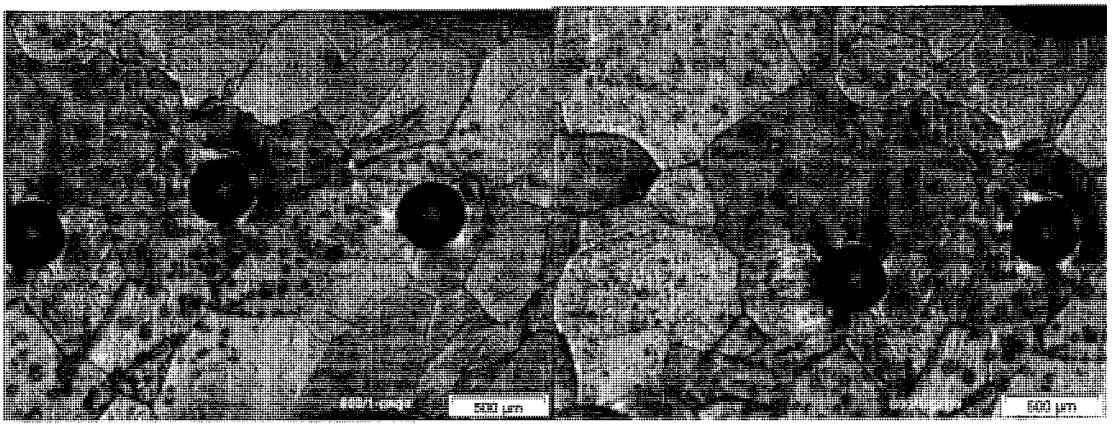

a b

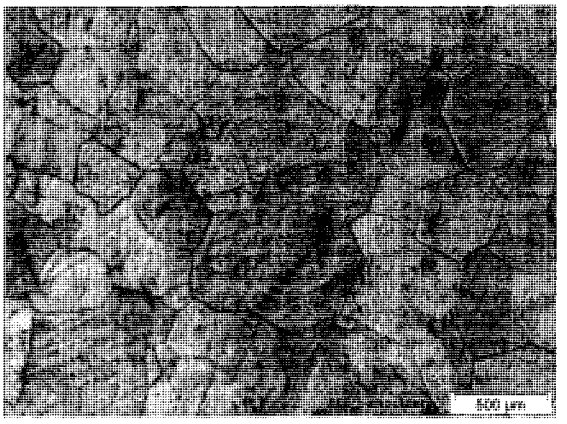

c

Fig. 4.15 Microstructure of specimen deformed at 600°C/1s^{-1} with fracture train $\varepsilon_f = 1.5$: a) + b): gage section, ×20; c): shoulder, ×20.

after a strain of about 1.5. Figure 4.15b shows that the grains in gage section (right side) are elongated but those near shoulder (left side) have little trace of elongation. However, when Figure 4.15 is compared with Figure 2.36b, 2.37b and 2.37c, substructure has formed inside the grains but its walls are not defined well enough to be etched up. The average grain diameter in the gage section as in Figure 4.15a and 4.15b is about 581μm. In shoulder as shown in Figure 4.15c, the average grain size is about 394μm.

The grains in the specimen deformed at 700°C/1s^{-1} are severely elongated at about 70° to the axis as shown in Figure 4.16a, and fine subgrains have formed inside the grains

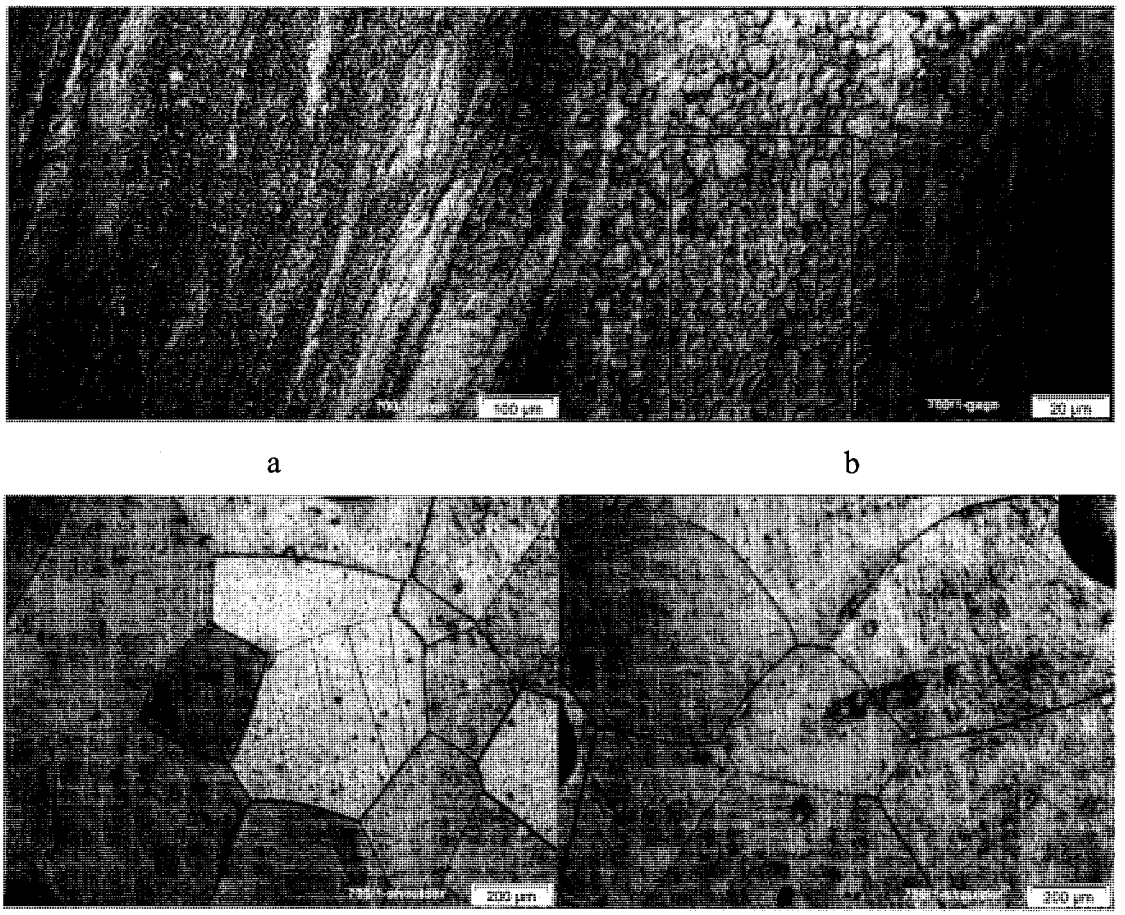

a b

c d

Fig. 4.16 Microstructure of specimen deformed at 700°C/1s^{-1} with fracture strain $\varepsilon_f = 5.5$: a): gage section, ×100; b): gage section: the area inside the frame is used to calculate subgrain size, ×500; c) + d) shoulder, ×50.

as shown in Figure 4.16b. Original GBs are recognized as the long lines sometimes severely serrated in contact with subgrain boundaries. However, it is possible that some new grains have nucleated along GBs during cooling. Notably at triple junctions, the subgrains are small and there may be some SRX nuclei of smaller size so that it is difficult to distinguish them. The area inside the frame where the subgrains are clearly outlined is chosen to calculate subgrain diameter that is about 2.9μm. According to

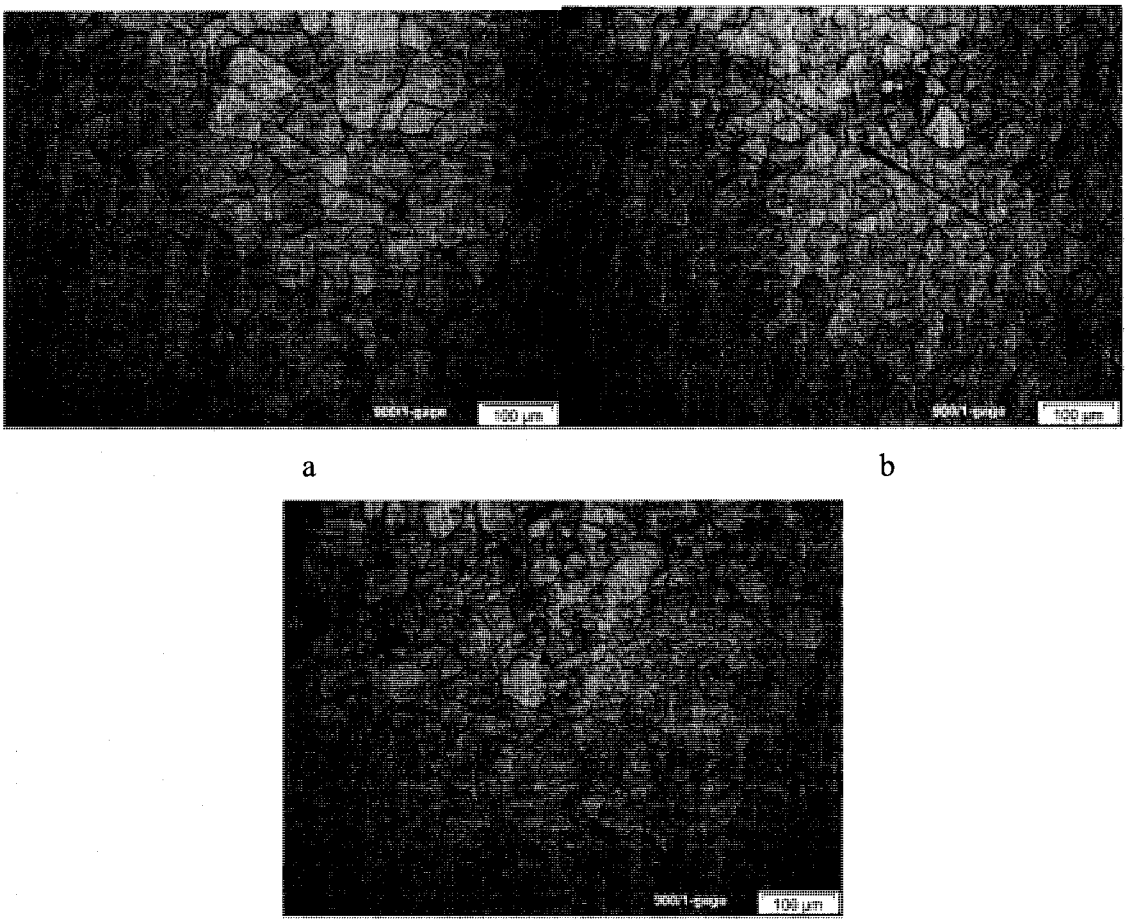

Fig. 4.17 Microstructures of gage section of the specimen deformed at 900°C/1s^{-1} with fracture strain $\varepsilon_f = 14.3$: a) average subgrain size: 60μm; b) average subgrain size: 29μm; c): subgrains with a size of 60μm coexist with those smaller than 20μm; ×100.

Equations 2.1 and 2.2, the subgrain size should increase with the increase of deformation T. Therefore, the subgrain size of the specimen at 700°C/1s^{-1} should be bigger than that at 600°C/1s^{-1}. In shoulder, the average grain diameter is about 496μm.

The specimen deformed at 800°C/1s^{-1} with $\varepsilon_f = 3.5$ apparently underwent SRX due to error in quenching; therefore, it is omitted from analysis.

The specimen deformed at 900°C/1s^{-1} has areas with noticeably different subgrain sizes. Some areas typical of Figure 4.17a have an average size of 60μm. Big subgrains with a diameter of approximately 90μm might cause gDRX. If cooling after deformation is slow, SRX may also nucleate new grains which grow bigger than the subgrains. There are some regions with subgrains of about 20μm in diameter and other areas with subgrains of intermediate size 29μm as shown in Figure 4.17b. Bimodal structures are also found in considerably big areas as shown in Figure 4.17c. Big subgrains coexist with fine subgrains smaller than 20μm.

4.2.2 Multi-stage tests

4.2.2.1 Flow curves and stress comparison

As simulations of rolling schedules, 17-pass torsion schedules for Fe-2.7Si-0.06C are simulated with pass strain ε_i varying from 0.2 to 0.3 and 0.4, pass interval t_i from 20s to 40s and strain rate $\dot{\varepsilon}$ =1s^{-1} for all schedules. T_i declines from 900 to 600°C for schedules in Figures 4.18 and 4.19. For any schedule with fixed pass strain ε_i and interval t_i between two successive passes, the maximum stress σ_{mi} in pass i varies due to the effect of DRV during deformation as well as SRV and SRX during interval between passes $i-1$ and i. Reloading stress σ_{ri} relative to $\sigma_{m(i-1)}$ also varies indicating the effect of SRV and SRX after pass $i-1$. Figure 4.20 shows the schedule with $\varepsilon_i = 0.2$, $t_i = 40$ s and T_i declining from 1000 to 700°C. For the same pass number, σ_{mi} and σ_{ri} are much lower than those of the test with the same ε_i and t_i but T_i declining from 900 to 600°C as shown in Figure 4.21d, because higher T_i results in more restoration. Because of insufficient time for Si solute atoms

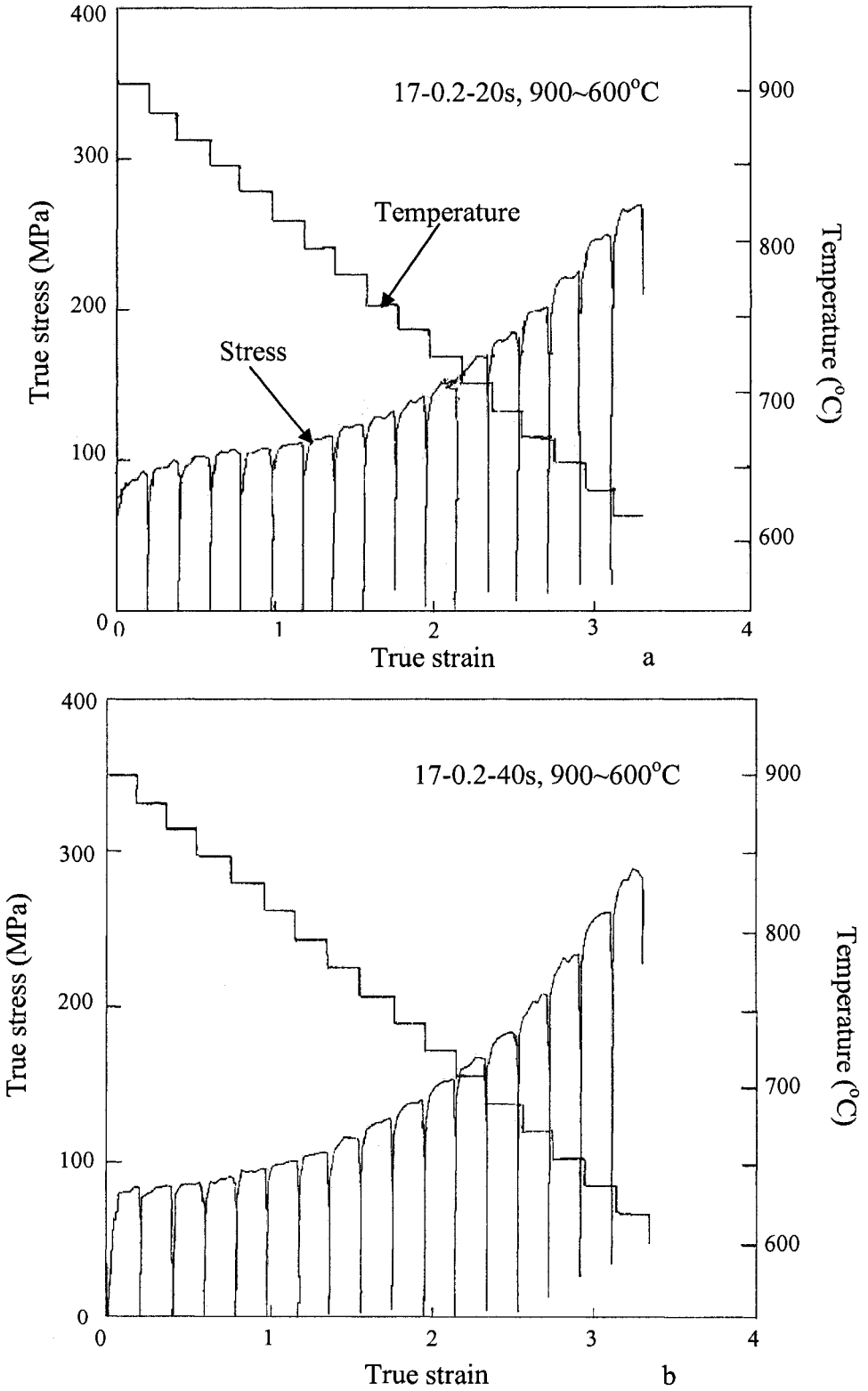

Fig. 4.18 17-stage torsion schedules for Fe-2.7Si-0.06C when $\dot{\varepsilon}$=1s^{-1} and T_i decreases from 900°C to 600°C: a) $\varepsilon_i = 0.2$, $t_i = 20$ s; b) $\varepsilon_i = 0.2$, $t_i = 40$ s.

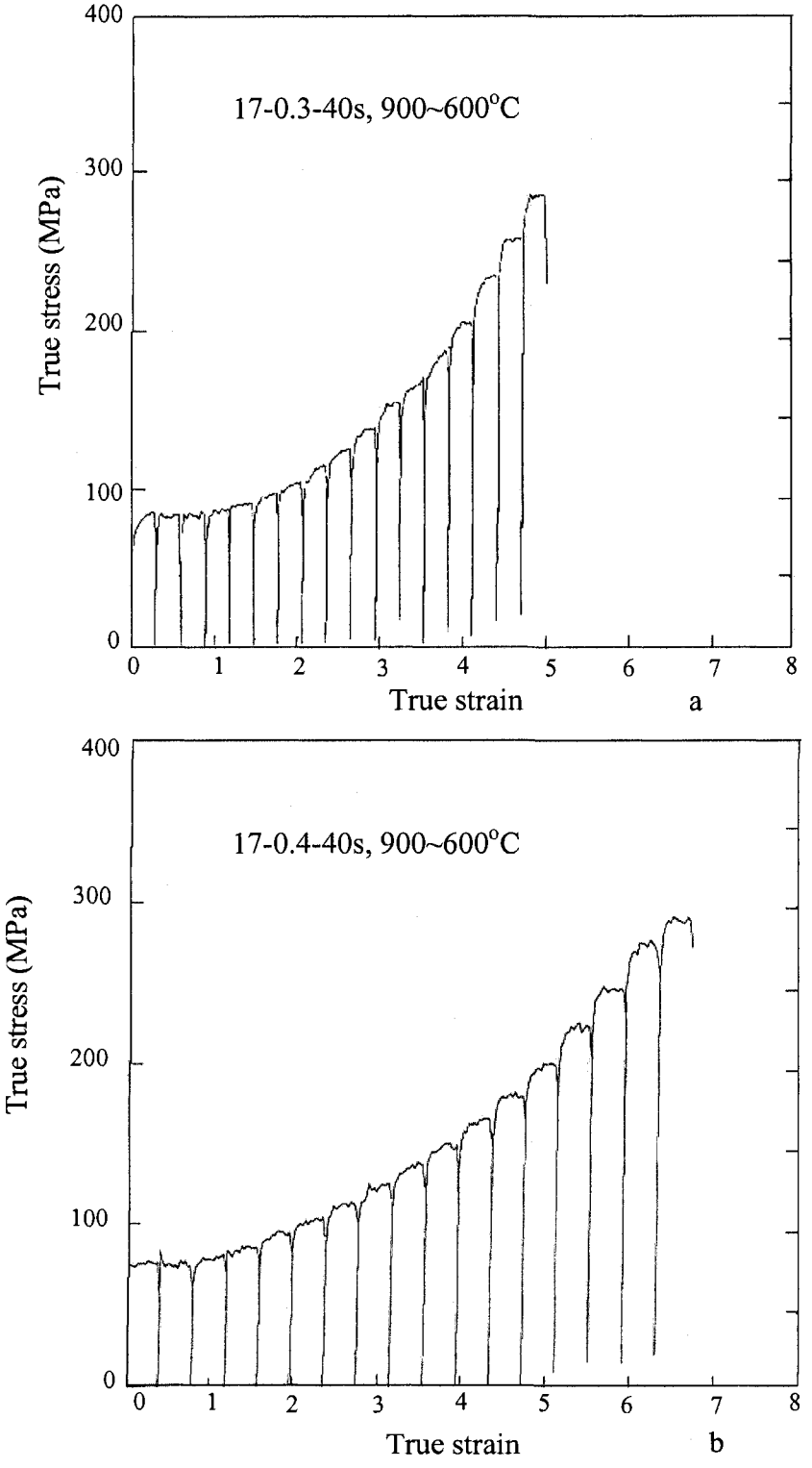

Fig. 4.19 17-stage torsion schedules for Fe-2.7Si-0.06C when $\dot{\varepsilon}$=1s^{-1} and T_i decreases from 900°C to 600°C: a) $\varepsilon_i = 0.3$, $t_i = 40$ s; b) $\varepsilon_i = 0.4$, $t_i = 40$ s.

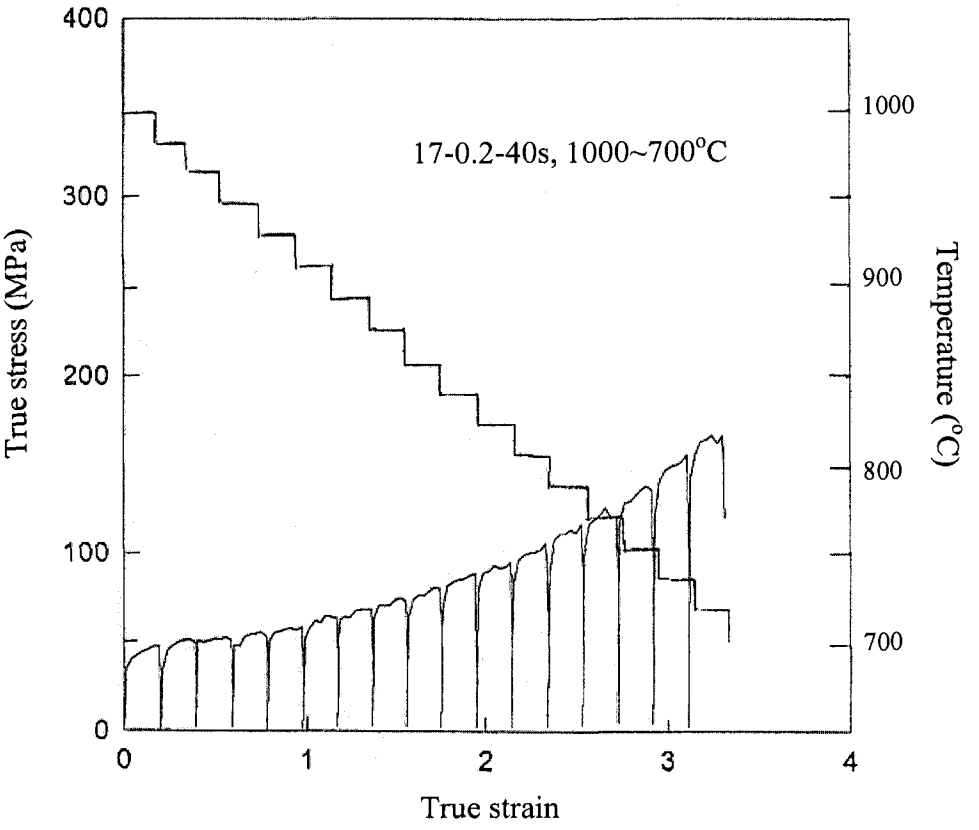

Fig. 4.20 17-stage torsion schedule for Fe-2.7Si-0.06C when $\dot{\varepsilon}=1s^{-1}$ and T_i decreases from 1000°C to 700°C, $\varepsilon_i = 0.2$, $t_i = 40$ s.

to segregate to dislocations, the pass curves do not exhibit the yielding seen in isothermal tests. In Figure 4.21, σ_{mi} is always lower than σ_{Pi} because in every pass, the specimen only undergoes strain hardening but never reaches the steady state of the isothermal-continuous test defined by T_i, ε_i and $\dot{\varepsilon}$. The variations of σ_{mi}, $\sigma_{r(i+1)}$ and $\sigma_{mi} - \sigma_{r(i+1)}$ with ε_i, t_i and the range of T_i are shown in Table 4.1.

All the other schedules are compared to the one with $\varepsilon_i = 0.2$, $t_i = 40$ s and T_i declining from 900 to 600°C. The schedule 0.2-20, 900~600°C is expected to have higher σ_{mi} and $\sigma_{r(i+1)}$ values but lower $\sigma_{mi} - \sigma_{r(i+1)}$ values than those of 0.2-40, 900~600°C

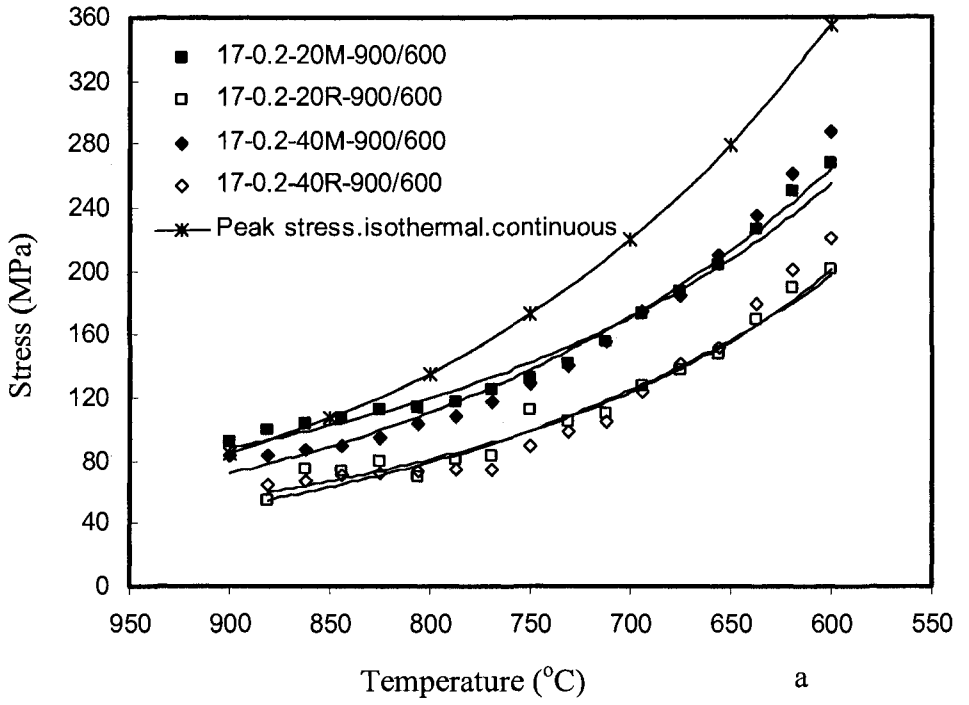

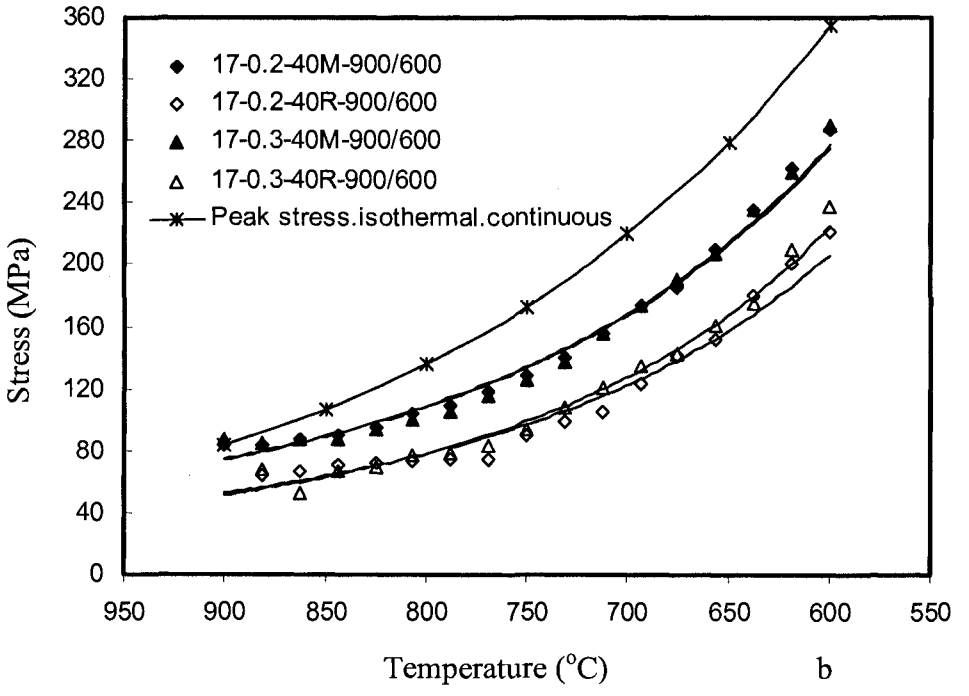

Fig.4.21 Comparison between σ_{Pi} in isothermal-continuous tests and σ_{mi} (M) as well as σ_{ri} (R) in multi-stage tests: a) effect of t_i when $\varepsilon_i = 0.2$; b) effect of ε_i when $t_i = 40$ s. T_i declines from 900 to 600°C in all tests.

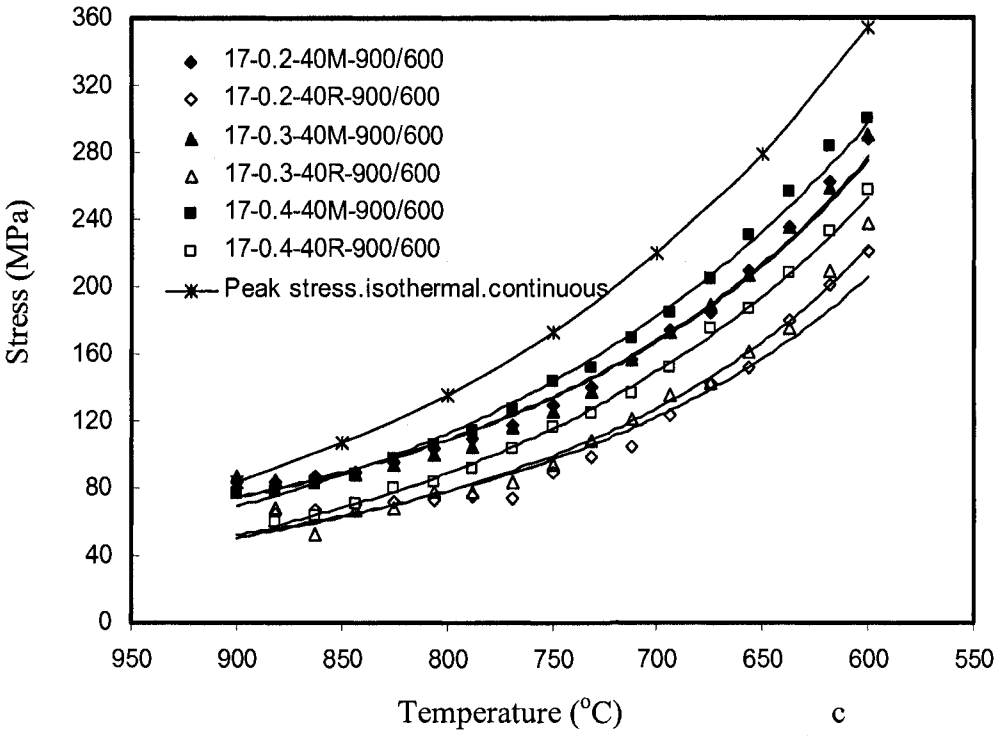

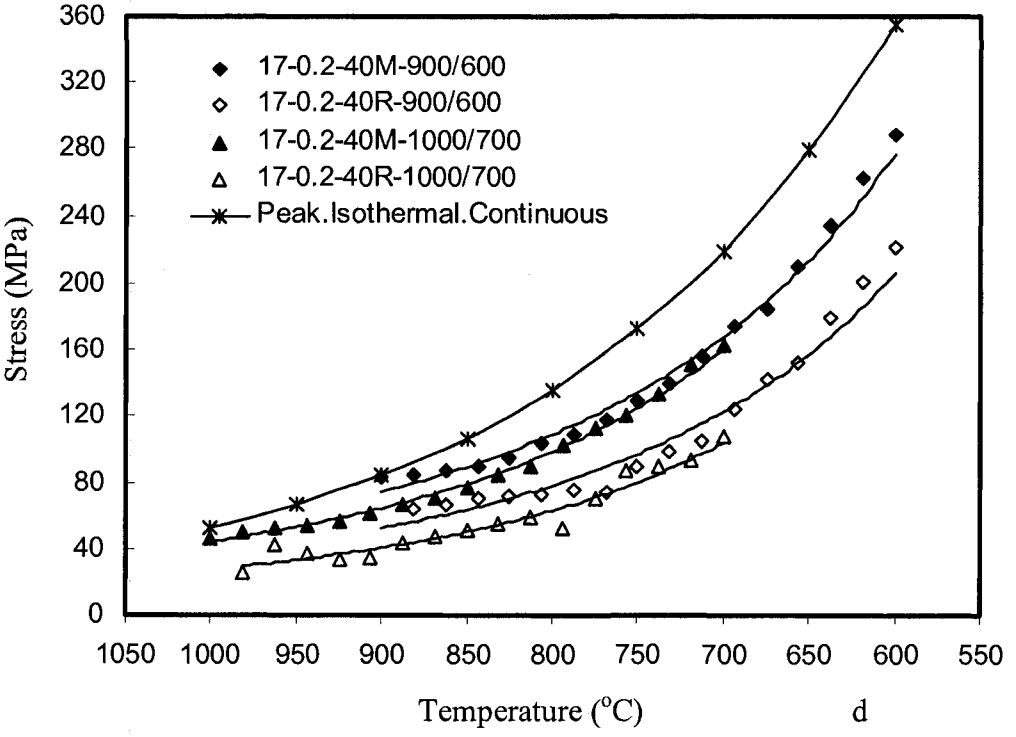

Fig.4.21 Continued: c) effect of ε_i when $t_i = 40$ s. T_i declines from 900 to 600°C in all tests; d) effect of T_i when $\varepsilon_i = 0.2$ and $t_i = 40$ s.

Table 4.1 The variations of σ_{mi}, $\sigma_{r(i+1)}$ and $\sigma_{mi} - \sigma_{r(i+1)}$ with ε_i, t_i and the range of T_i

Figure	Comparison	σ_{mi}		$\sigma_{r(i+1)}$		$\sigma_{mi} - \sigma_{r(i+1)}$	
	900~600°C	Expected	Observed	Expected	Observed	Expected	Observed
4.21a	0.2-20/0.2-40	Higher(1a)	Higher>700°C	Higher(2a)	Equal	Less(2a)	More
4.21b	0.3-40/0.2-40	Higher(1b)	Equal	N/A	Higher<750°C	More(2b)	Less
4.21c	0.4-40/0.2-40	Higher(1b)	Higher	N/A	Higher	More(2b)	Much less
	0.2-40 for the same pass number i						
4.21d	1000~700°C / 900~600°C	Lower Higher T	Lower Higher T	Lower Higher T	Lower Higher T	Less (3) Higher T	More (4) Higher T

1a: Less SRV/SRX due to shorter t_i; 1b: Higher strain hence more strain hardening;

2a: Less SRV/SRX due to shorter t_i ; 2b: More SRV/SRX due to higher strain energy from higher strain;

3: Stress drop limited by low strain hardening rise in σ;

4: More SRV/SRX due to higher thermal energy from higher T; N/A: Not applicable

because of less SRX and SRV owing to shorter t_i .The schedule 0.3-40, 900~600°C is expected to have higher σ_{mi} values because of more strain hardening from a higher strain, but $\sigma_{r(i+1)}$ values cannot be qualitatively estimated because a higher strain causes both more strain hardening and more SRV and SRX. Higher $\sigma_{mi} - \sigma_{r(i+1)}$ values are expected for this schedule because of more SRV and SRX. The schedule 0.4-40, 900~600°C is expected to have higher σ_{mi} and $\sigma_{mi} - \sigma_{r(i+1)}$ values, but $\sigma_{r(i+1)}$ values cannot be qualitatively estimated. The extremely low values of $\sigma_{mi} - \sigma_{r(i+1)}$ for 0.4-40 schedule indicates that t_i is likely incorrect in this schedule. σ_{mi} values are expected to increase in the order of ε_i 0.2, 0.3 and 0.4 with a fixed t_i due to rising strain hardening or in the order of t_i 40s, 20s with a fixed ε_i because of less SRV and SRX. $\sigma_{mi} - \sigma_{r(i+1)}$ values are expected to increase with rising ε_i at a fixed t_i because higher strain energy leads to more SRV and SRX or with longer t_i at a fixed ε_i because of more SRV and SRX.

The schedule 0.2-40, 1000~700°C is expected to have lower σ_{mi} and $\sigma_{r(i+1)}$ values than those of 0.2-40, 900~600°C because higher T_i leads to more restoration. Moreover, its $\sigma_{mi} - \sigma_{r(i+1)}$ values should be higher because, although higher T_i reduces strain energy from deformation, the much higher thermal energy during the intervals surpasses the reduction and leads to a much faster restoration that reduces $\sigma_{r(i+1)}$ considerably hence causes an increase in $\sigma_{mi} - \sigma_{r(i+1)}$ values.

The comparison between yielding stress σ_{yi} from compression [57], σ_{Pi} in

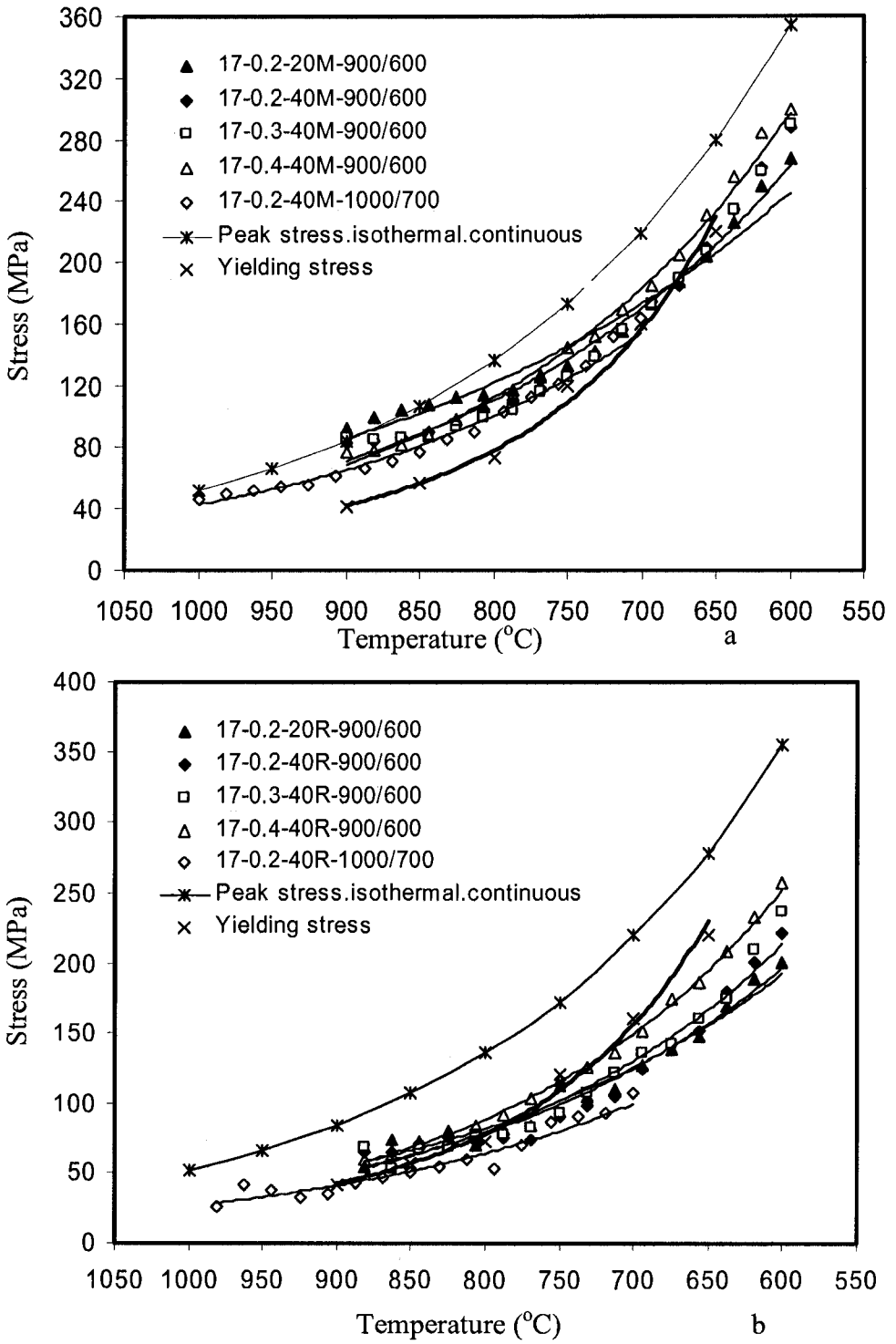

Fig.4.22 Comparison between yielding stress σ_{yi} in compression [57], σ_{Pi} in isothermal-continuous torsion tests and a): σ_{mi}; b): σ_{ri} in different multi-stage torsion schedules with T_i declining.

current isothermal-continuous torsion tests and σ_{mi} as well as σ_{ri} in different multi-stage torsion schedules with T_i declining is exhibited in Figure 4.22. σ_{yi} values are always lower than σ_{Pi} values at the same T_i and $\dot{\varepsilon}_i$ but not always lower than those of σ_{mi} and σ_{ri} so that it is not feasible to calculate FS_i of multi-stage tests; therefore, RS_i and RRS_i are calculated instead.

4.2.2.2 Relative softening RS_i and relative reduction of stress RRS_i

As presented in Figure 4.23, $\sigma_{mi} - \sigma_{r(i+1)}$ increases with declining T_i although very irregular but RS_i ($=(\sigma_{mi} - \sigma_{r(i+1)})/\sigma_{mi}$) generally decreases regardless of the increase of $\sigma_{mi} - \sigma_{r(i+1)}$, indicating that softening during the intervals decreases with declining T_i as shown by σ_{mi} increasing faster than $\sigma_{r(i+1)}$. The 1000~700°C schedule has higher $\sigma_{mi} - \sigma_{r(i+1)}$ and RS_i values than those of 900~600°C schedules as shown in Figures 4.23a, 4.23b and 4.23c and 4.23d. At a fixed T_i in the range 900~600°C, $\sigma_{mi} - \sigma_{r(i+1)}$ values decrease in the order of 0.2-20, 0.2-40, 0.3-40 and 0.4-40, which is contradictory to what has been expected. RS_i decreases in the same order, and its rates of decrease are relatively high for 0.2-20 and 0.3-40 schedules but low for 0.2-40, 0.4-40, 900~600°C schedule as well as 0.2-40, 1000~700°C schedule. At 800°C, RS_i value is 30% for 0.2-40, 1000~700°C schedule and decrease from 26 to 20% in the order 0.2-20, 0.2-40, 0.3-40 for 900~600°C schedules. It is only 12% for the schedule 0.4-40, 900~600°C, and this is further indication that the actual t_i for 0.4-40 schedule is much less than 40s; the real time is likely to be 10s. The decrease as T_i declines is related to the rapid

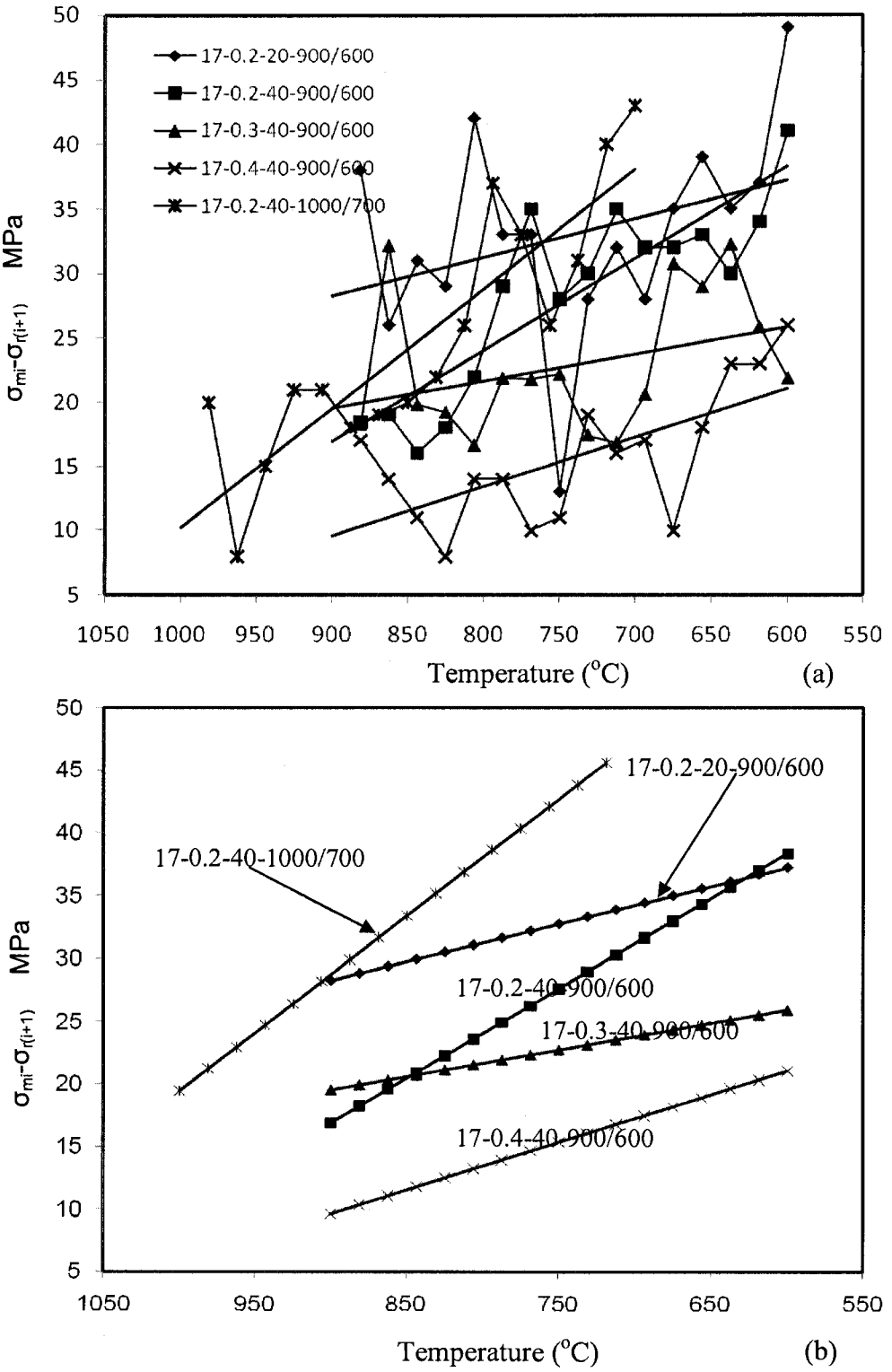

Fig.4.23 The variation of $\sigma_{mi} - \sigma_{r(i+1)}$ with T_i : a) original data points fluctuating around the calculated points shown as trendline; b) Calculated trendline.

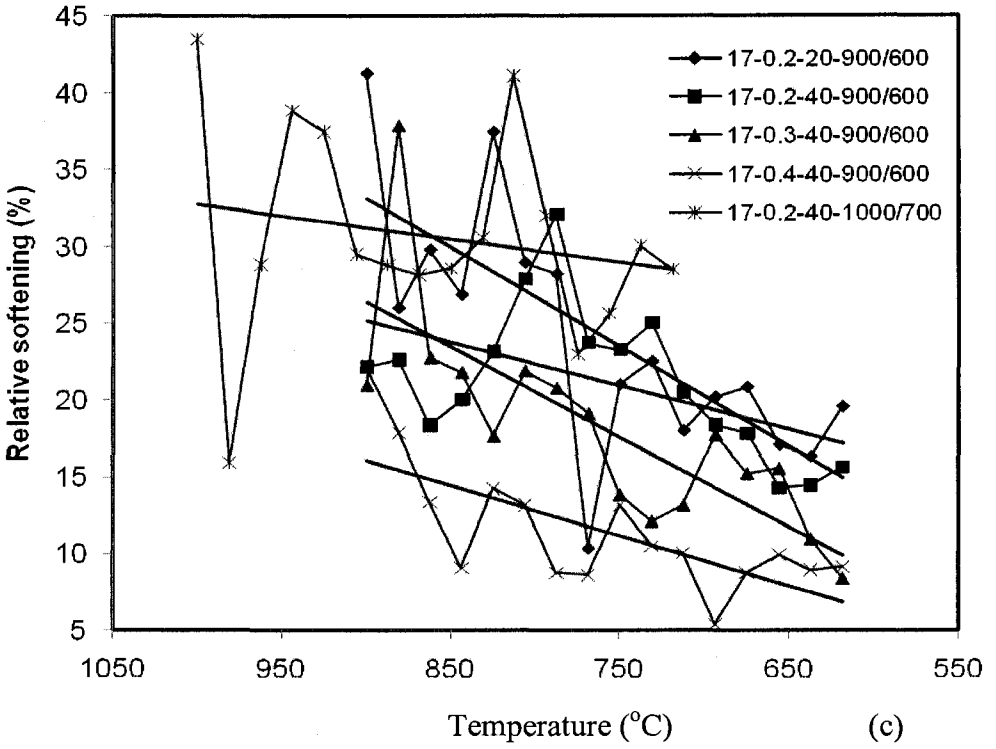

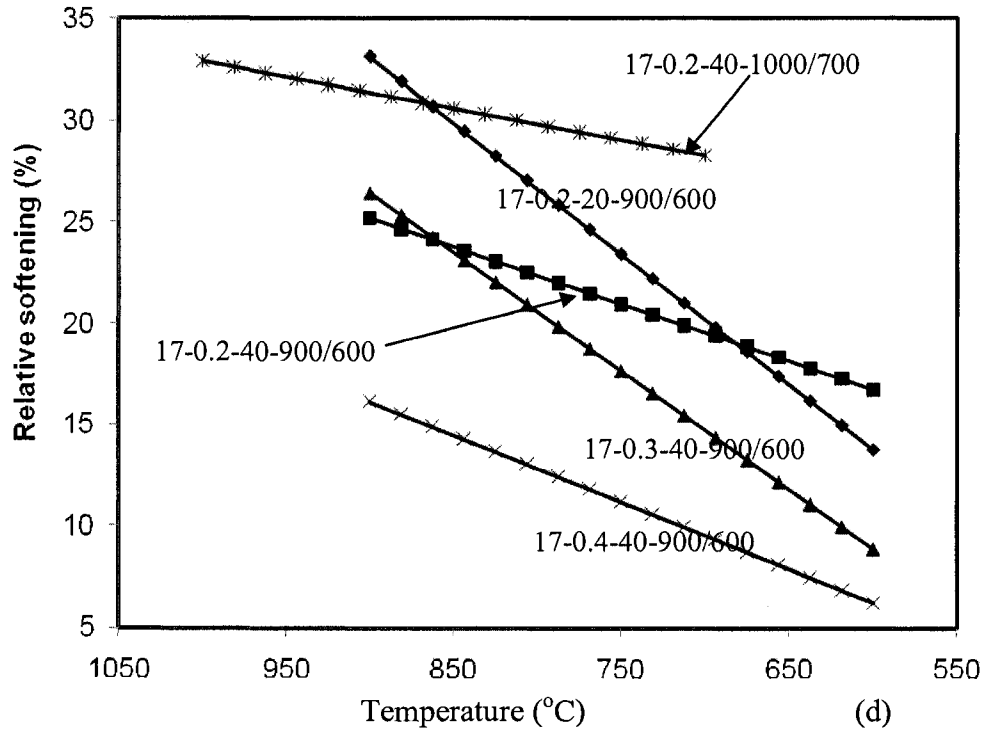

Fig.4.23 Continued: The variation of relative softening (RS_i) with T_i : c) original data points fluctuating around the calculated points shown as trendline; d) Calculated trendline.

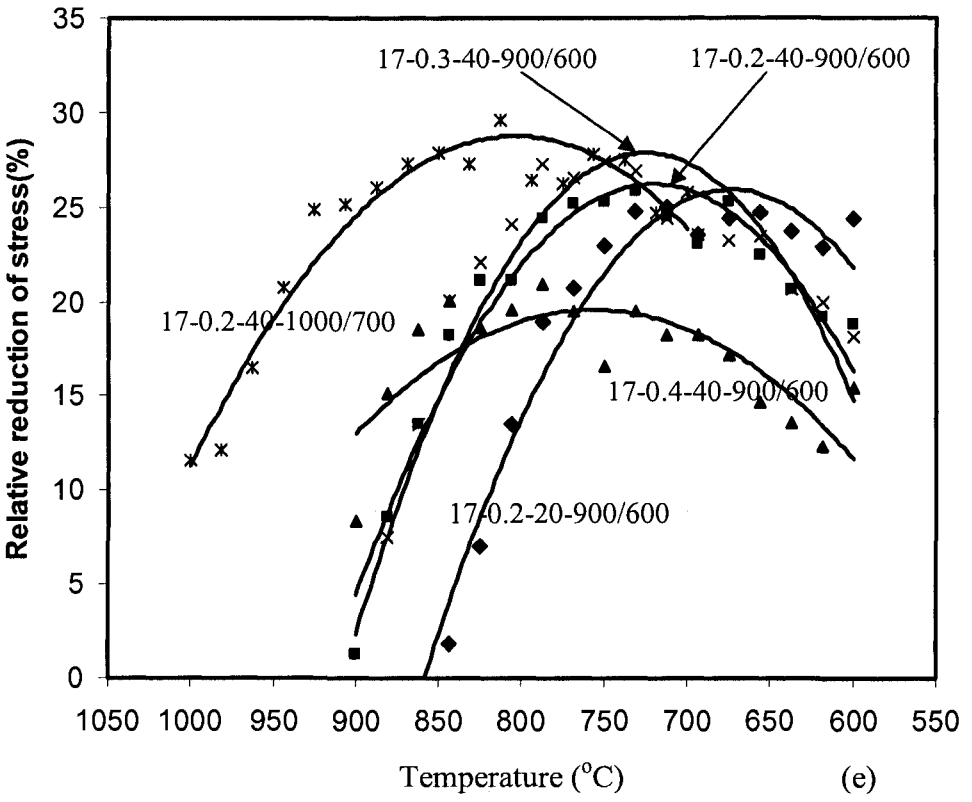

Fig.4.23 Continued: e) The variation of relative reduction of stress (RRS_i) with T_i.

rise of σ_{mi} for relatively little change of $\sigma_{mi} - \sigma_{r(i+1)}$ (Figure 4.21 and 4.23).

The actual RS_i values fluctuate along the trendlines as shown in Figure 4.23c, which is related to the change of SRX. At high T_i, although strain energy is low, the high thermal energy drives the specimen to statically recrystallize during the following interval. Consequently, the high level of SRX leads to a high RS_i. If after the next pass, the strain energy is low, there will be little SRX and hence a low value of SRX and RS_i. However, after several intervals of low RS_i, the strain energy has accumulated and is once more high, SRX will be nucleated and causes a relatively high RS_i. With the decrease of T_i and reduction in thermal energy, the fluctuations of the level of SRX and

RS_i become more widely spaced. However, the new SRX grains keep deforming and elongating, and they are difficult to see at the end of the schedules as will be clarified in section 4.2.2.3.

In all schedules, the RRS_i ($=(\sigma_{Pi}-\sigma_{mi})/\sigma_{Pi}$) values show a similar pattern: rising from low values at high T_i to maxima in the range 850~670°C followed by a decrease at low T_i. The benefit of interpass softening rises from high to intermediate T_i, because at high T_i, σ_{Pi} increases more rapidly than σ_{mi} (Figure 4.21), which results in a rise of RRS_i values; but at low T_i, σ_{Pi} increases more slowly than σ_{mi}, which leads to the small decrease of RRS_i values. The maxima, almost 29 for the 1000~700°C schedule, are 28~26 for 0.2-20, 0.2-40 and 0.3-40, 900~600°C schedules but only 20 for the $\varepsilon_i = 0.4$ schedule. On the basis of higher ε_i raising the amount of SRV and SRX, one would expect a rise of RS_i and RRS_i values for 0.4-40 schedule. However, in contrast to the expectation, the distance between σ_{mi} and $\sigma_{r(i+1)}$ in Figure 4.21c is much smaller for 0.4-40 than the 0.2-40 and 0.3-40 schedules. One can only speculate that the actual t_i of the test was much shorter than 40s due to an error in programming.

4.2.2.3 Microstructure

The microstructure of the nondeformed specimen is shown in Figure 4.24. From these, the recrystallized grains are estimated to have an average size of about 250μm and have some trace of impurity alignment from rolling. The microstructures of 0.2-20, 0.2-40, 0.3-40 and 0.4-40, 900~600°C specimens are individually shown in Figure 4.25, 4.26, 4.27 and 4.28. Because of the low finishing T_i, all specimens exhibit grains with

deformation bands often with severely serrated GBs with fine substructure inside grains. The specimen with $\varepsilon_i = 0.3$, $t_i = 40$ s clearly exhibits subgrains inside the severely serrated grain boundaries.

The specimen deformed through 1000 to 700°C as shown in Figure 4.29 has more clearly serrated grains and better outlined larger subgrains than in specimens with lower finishing T_i. The etching is certainly different possibly because dislocation density is less within subgrains.

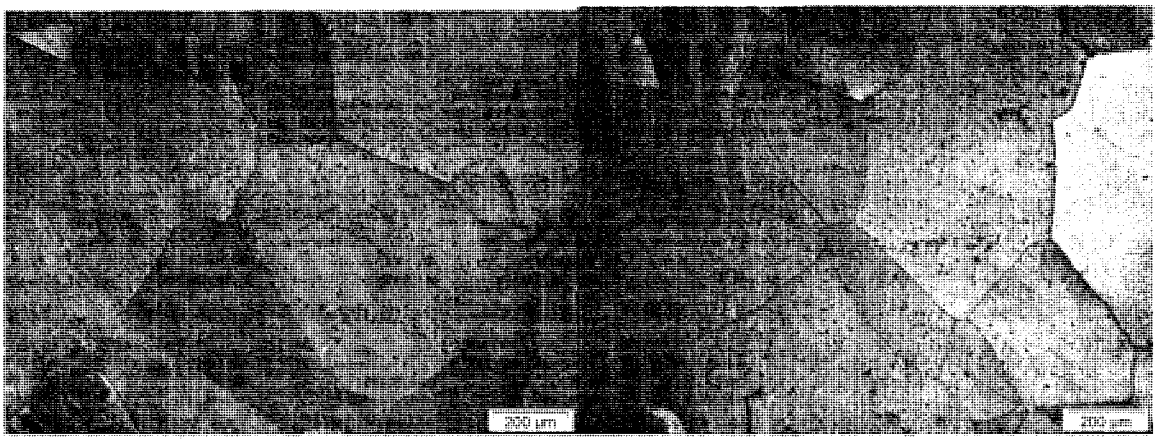

a b

Fig. 4.24 Microstructure of nondeformed specimen with average grain size 250μm, ×50.

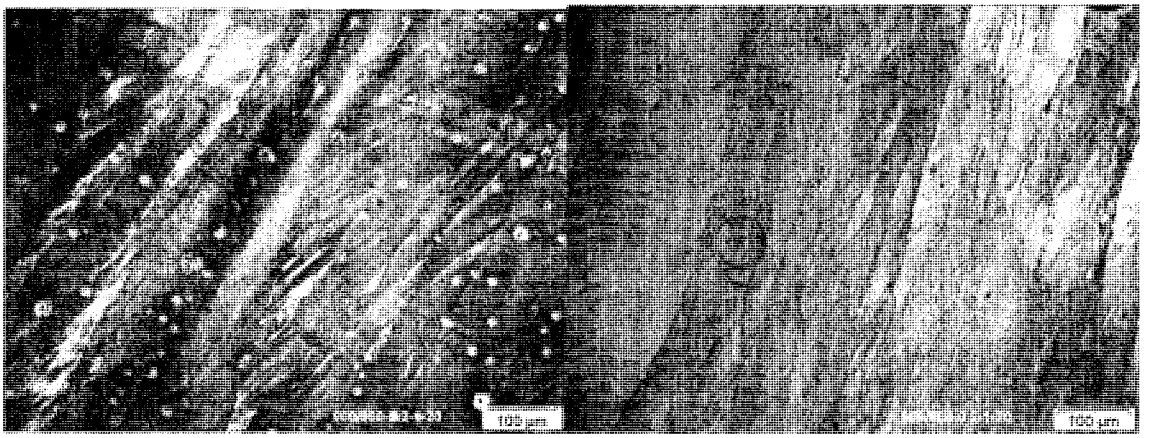

a b

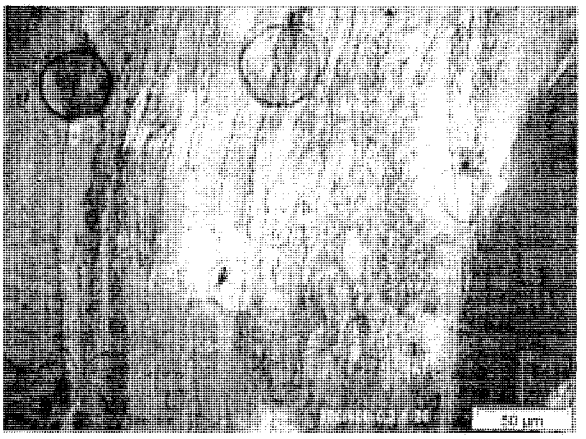

c

Fig. 4.25 Microstructure of specimen deformed with 17 passes when $\dot{\varepsilon}$=1s^{-1}and T_i decreases from 900°C to 600°C, $\varepsilon_i = 0.2$, $t_i = 20$ s. a) +b): ×100; c): ×200.

a b

Fig. 4.26 Microstructure of specimen deformed with 17 passes when $\dot{\varepsilon}$=1s^{-1} and T_i decreases from 900°C to 600°C, $\varepsilon_i = 0.2$, $t_i = 40$ s. a) +b) +c): ×100; d): ×200.

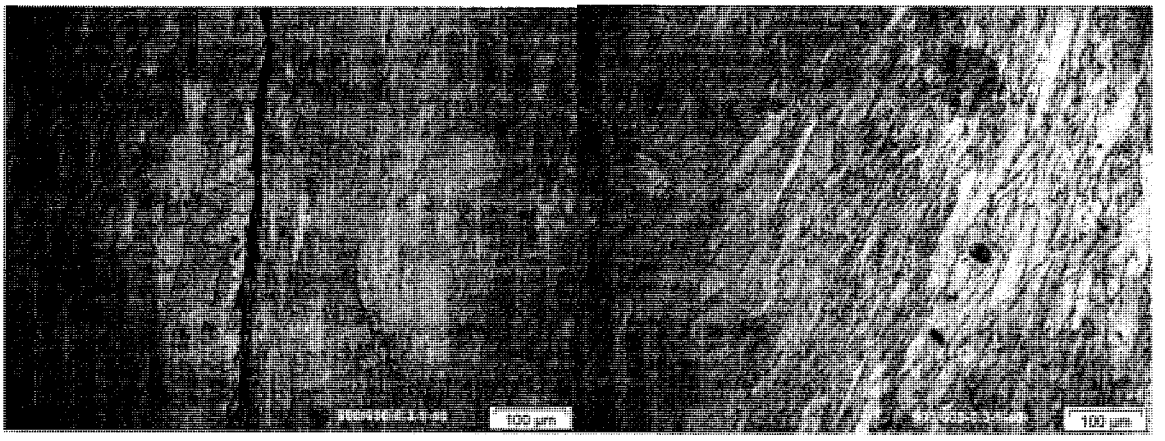

a b

Fig. 4.27 Microstructure of specimen deformed with 17 passes when $\dot{\varepsilon}$=1s^{-1} and T_i decreases from 900°C to 600°C, $\varepsilon_i = 0.3$, $t_i = 40$ s. a) +b) +c): ×100.

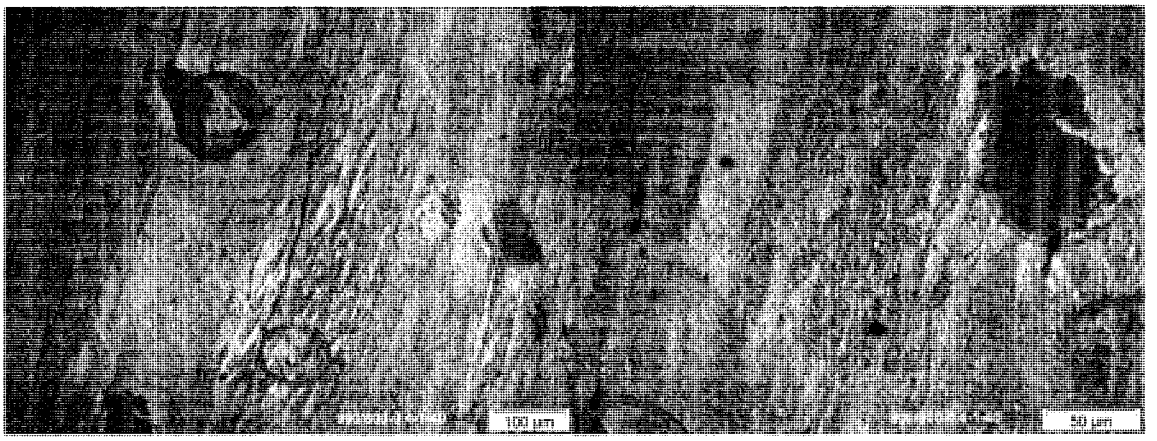

a b

Fig. 4.28 Microstructure of specimen deformed with 17 passes when $\dot{\varepsilon}$=1s^{-1} and T_i decreases from 900°C to 600°C, $\varepsilon_i = 0.4$, $t_i = 40$ s. a): ×100; b): ×250.

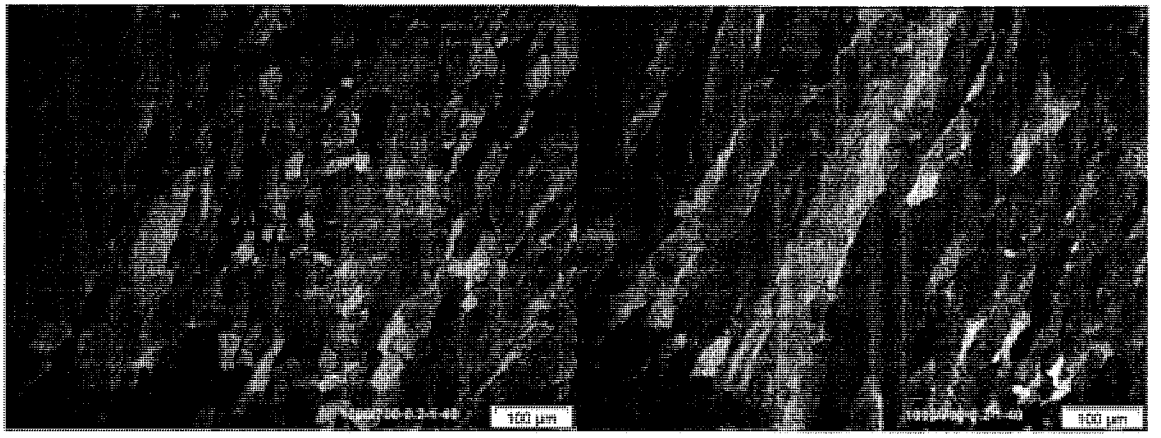

a b

Fig. 4.29 Microstructure of specimen deformed with 17 passes when $\dot{\varepsilon}$=1s^{-1} and T_i decreases from 1000°C to 700°C, $\varepsilon_i = 0.2$, $t_i = 40$ s. a) +b): ×100.

CHAPTER FIVE

DISCUSSION

5.1 Fe_3Al

5.1.1 Ductility and flow stress

In contrast to ferritic stainless steels, the current intermetallic Fe_3Al, exhibits quite different dependence of hot workability on deformation T and $\dot{\varepsilon}$ although it is body-centered cubic in the experimental range. The Zener-Holloman parameter Z, which correlates the effect of T and $\dot{\varepsilon}$, has a major effect on fracture. When $Z \leq 16$, crack nucleation and growth are very difficult even when non-deformable second-phase particles exist inside the specimens. During heavy deformation, the specimens develop severe protrusions and deep indentations at the surface along GBs where cracks start to nucleate. In some sites, the big cavities inside the samples may connect with surface cracks accelerating the propagation of the cracks, causing failure eventually. The cracks sustain the heavy torsion with high ductility at reduced stress [64, 65].

In Figure 5.1a at $830^{\circ}C/0.01s^{-1}$, the original grains were severely elongated at an angle about 60° to the axis. Some subgrains appeared in the matrix possibly the result of static recrystallization (SRX). At $950^{\circ}C/0.01s^{-1}$ and $950^{\circ}C/0.1s^{-1}$, the samples are full of equiaxed subgrains in original grains whose boundaries have been partially or totally masked by the serrations associated with subgrain boundaries. Moreover, the fracture strains of both specimens are so high that the grains may bear segments or pinchoff by geometric dynamic recrystallization (gDRX). The sizes are almost ten times magnitude of those at $830^{\circ}C/0.01s^{-1}$, which led to the lower steady state flow stresses than the latter as

explained by equations 2.2 ($d_S^{-1} = G + H \log Z$) and 2.3 ($\sigma_S = a + b d_S^{-q}$) [14]: at steady state, flow stress is reciprocally proportional to the subgrain size, which may explain why the sample deformed at 830°C/0.01s^{-1} could sustain higher flow stress than those at 950°C/0.01s^{-1} and 950°C/0.1s^{-1}. In long term creep, Nb addition forms Fe_2Nb precipitates that strengthen up to 600°C [26]. It is possible that at 830°C/0.01s^{-1}, some precipitates still pin the subgrain boundaries, refining subgrains. When deformation T increases to 950°C, the precipitates are likely to dissolve so that the subgrains become bigger and

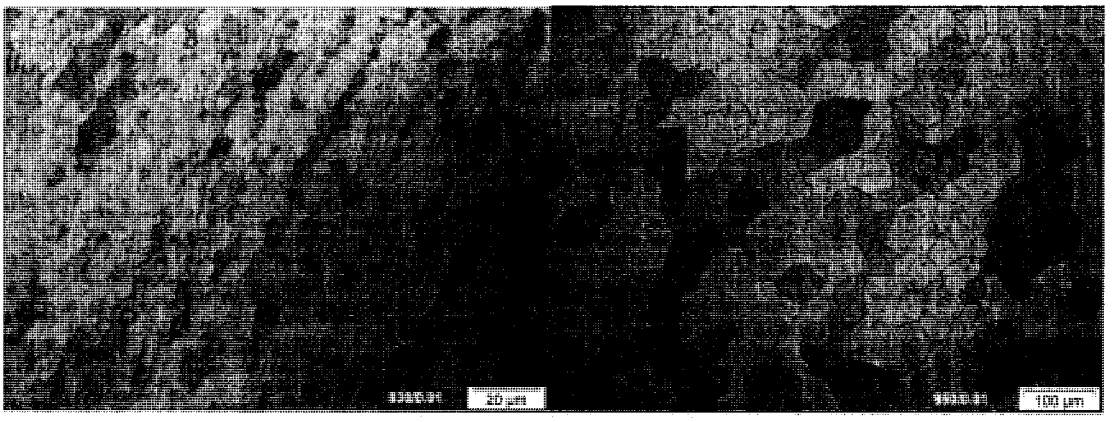

a b

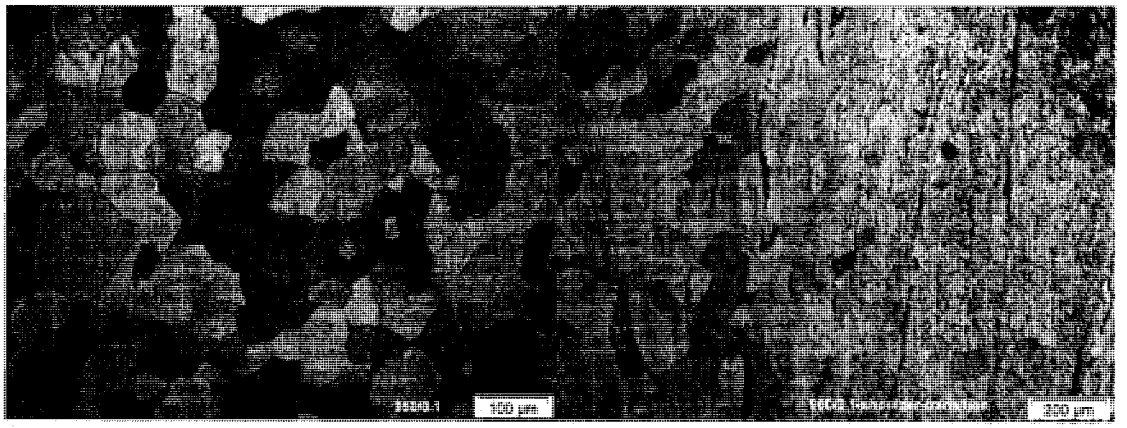

c d

Fig. 5.1 Microstructure of torsion samples of Fe_3Al: a) 830°C, 0.01s^{-1}, $\varepsilon_f > 20$, ×500; b) 950°C, 0.01s^{-1}, $\varepsilon_f = 15.4$, ×100; c) 950°C, 0.1s^{-1}, $\varepsilon_f = 6$, ×100; d) as in (c) the transition area from shoulder to gage (left to right), ×100.

strengthening decreases.

Figure 5.1d shows the transition area from shoulder to gage of the sample deformed at $950^{\circ}C/0.1s^{-1}$. The grains are big with various sizes in the shoulder section. Fine equiaxed subgrains are observed in the gage section. A narrow transition band lies between shoulder and gage sections, and some elongated grains appear with intermediate thickness.

When $Z > 16$, a few small subgrains appeared in some big grains in most of the surface, which implies that DRV does not proceed so fast in these specimens as in the three mentioned above. Meanwhile, the materials do not have many big cavities because of low deformation.

Compression tests do not extend the cracks so that the samples can sustain higher stress. Figure 5.2a shows current results. The flow stress increases when deformation T decreases and $\dot{\varepsilon}$ rises, because the mobility of dislocations decreases and their annihilation slows down. Consequently, dislocations are accumulated and a higher stress is required for deformation. Compression stress is always higher than that of torsion under the same deformation condition. At $830^{\circ}C/0.01s^{-1}$, the decrease of stress from compression to torsion is approximately 64%; this high difference suggests that the torsion stress is low because of the cavities and cracks discussed above. At $950^{\circ}C$, the decrease of flow stress from compression to torsion is approximately 24% at $0.01s^{-1}$ and 44% at $0.1s^{-1}$, indicating that the point for $950^{\circ}C/0.1s^{-1}$ is not sufficiently good. A trendline linking torsion points at $750^{\circ}C/0.01s^{-1}$ and $950^{\circ}C/0.01s^{-1}$ shows that the flow stress has similar trend to that at $0.1s^{-1}$; obviously, the point of $830^{\circ}C/0.01s^{-1}$ is out of the reasonable trend and should be omitted from analysis.

Comparison is made between current data and those from Voyzelle (Figure 5.2b)

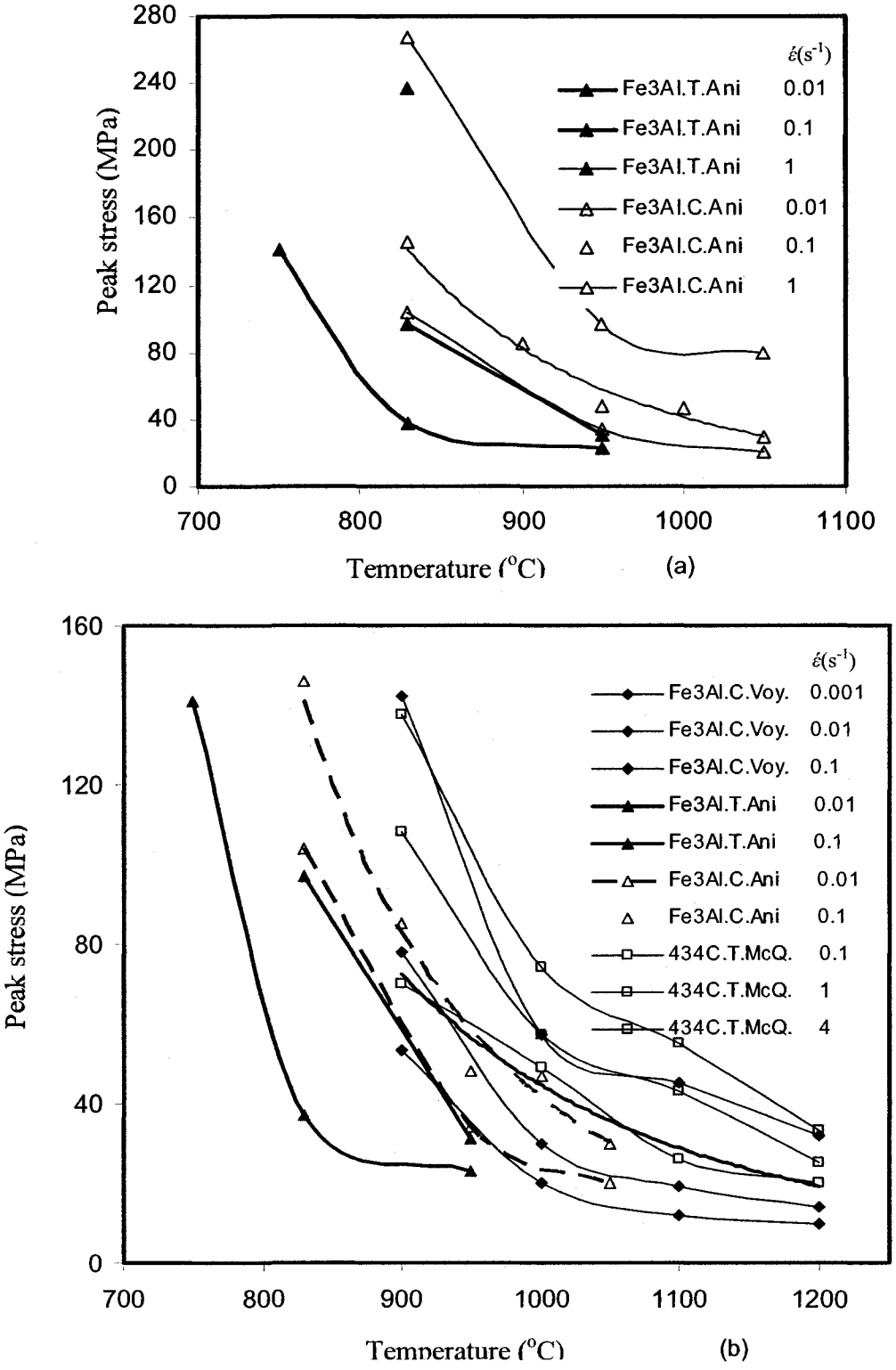

Fig.5.2 Comparison of peak stress σ_p : a) present results of Fe_3Al,

b) dependence of σ_p of Fe_3Al and 434C on T and $\dot{\varepsilon}$.

[4, 5]. Under the same deformation condition, the sample from Voyzelle has higher stress than current material although they have the same composition, possibly because the improper rolling of current material caused preexisting cracks in contrast with the material of Voyzelle that was well-rolled. Figure 5.2b also exhibits the flow stress of ferritic stainless steel 434C. At $0.1s^{-1}$, its flow stress is close to the current compression stress. However, at 1 and $4s^{-1}$, 434C has lower stresses than current compression stresses at $1s^{-1}$. Solutes may account for the difference; Fe_3Al has a higher solute content (wt%) than 434C, which represents a much higher concentration of Al atoms (at%). In tests at higher strain rates, possibly some remaining particles of Fe_2Nb add to the strengthening.

5.1.2 Constitutive comparison between Fe_3Al and 434C

The sinh Arrhenuis equation 2.1 ($A(\sinh \alpha\sigma)^n = \dot{\varepsilon} \exp(Q_{HW} / RT) = Z$) was used to provide the dependence on strain rate $\dot{\varepsilon}$ and temperature T of the flow stress σ [14]. Because σ diminishes after a peak, the peak stress σ_p is used in this equation. The stress multiplier α is selected to achieve a product that makes $\sinh(\alpha\sigma)$ linear over the range studied. Figure 5.3 shows the relationship between $Log\ \dot{\varepsilon}$ and $Log(\sinh \alpha\sigma)$. From the comparison of current torsion and compression lines in Figure 5.3a, the torsion point for $830^{\circ}C/0.01s^{-1}$ is not good, and the one at $950^{\circ}C/0.1s^{-1}$ is not valuable as expected. Figure 5.3b exhibits the comparison between current results and the compression results from Voyzelle [4, 5] as well as torsion results of 434C. For the same material (except Fe_3Al torsion), the distance between two neighboring σ - $\dot{\varepsilon}$ lines decreases with increasing T, indicating that the hot deformation is thermally activated. The lines of each material are almost parallel to each other (except Fe_3Al torsion), and the value of stress exponent n is calculated as the average of the slopes of the lines. In agreement with Figure 5.2, at the

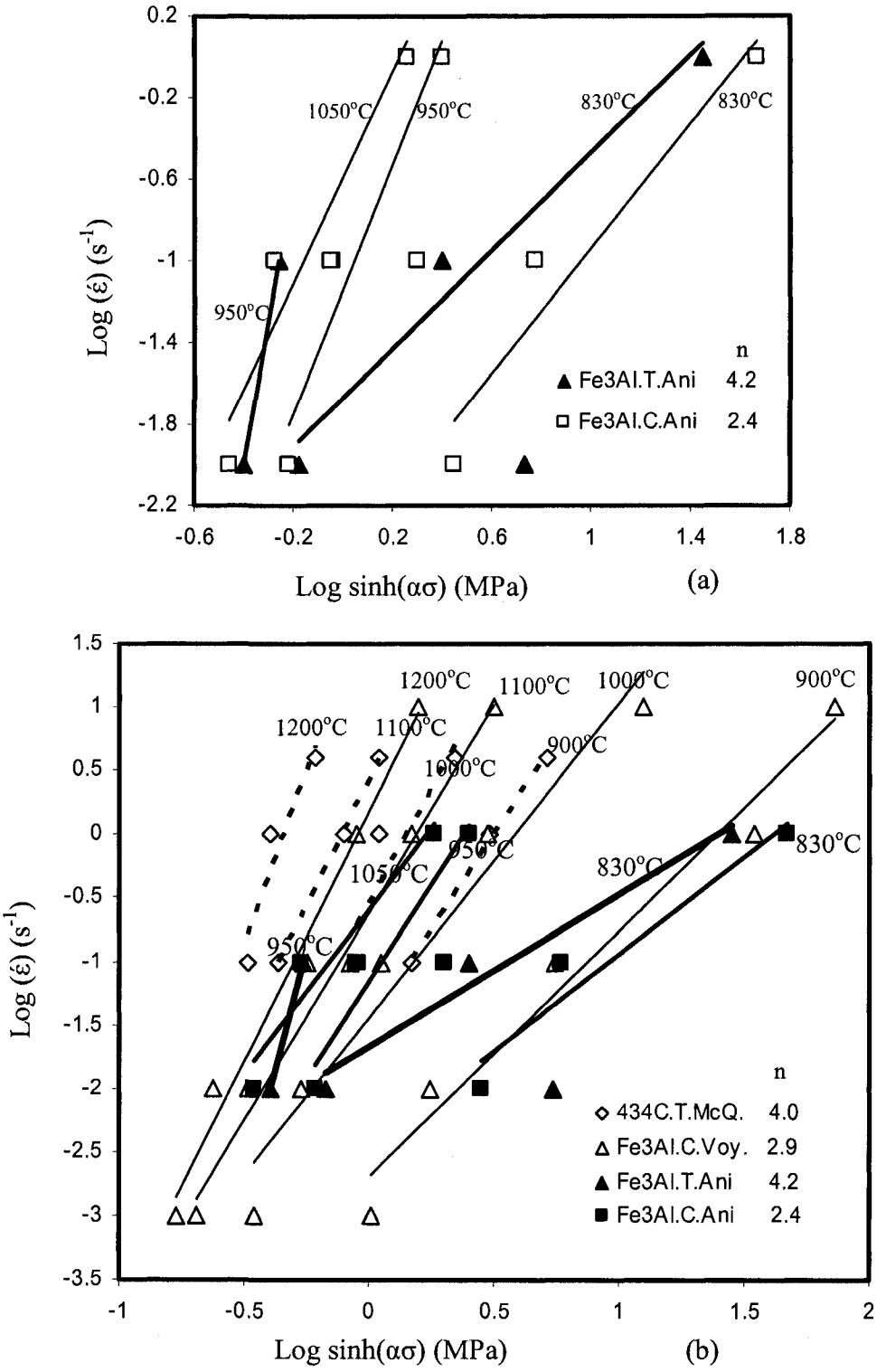

Fig.5.3 Log ε̇ versus Log (sinhασ): a) present results of Fe_3Al,

b) various sources of data for Fe_3Al and 434C.

same ε, the lines of 434C are located at lower σ than those of Fe_3Al. Moreover, the compression lines of current Fe_3Al at 950 and 1050°C lie at lower σ than that of Voyzelle at 1000°C and 1100°C respectively, but the line at 830°C lies partially at higher σ than that of Voyzelle at 900°C.

Figure5.4 shows the relationship between $Log(\sinh \alpha\sigma)$ and $1000/T$ for the alloys. For each material (except current Fe_3Al torsion), the lines are almost parallel to each other and the slope s is taken as the average of the slopes. Q_{HW} is calculated and the values for different materials are listed in Table 5.1. For Fe_3Al (torsion + compression, ~370kJ/mol), the values are in agreement with that of Voyzelle. The high values of n and Q_{HW} for the present torsion are probably associated with the randomness of the fractures. The 434C values are in remarkable agreement and indicate similarity of DRV level arising from the shared BCC crystal structure. The relationship between $LogZ$ and $Log(\sinh \alpha\sigma)$ are presented in Figure 5.5. The current compression line lies close to that of Voyzelle; the latter does not show such a good fit, as indicated by the curvature of the points. The present torsion line is shifted due to both the higher Q_{HW} and lower stresses (leftward). The 434C has a higher slope because of the relative change in comparative stresses with T and ε as pointed out in Figure 5.2.

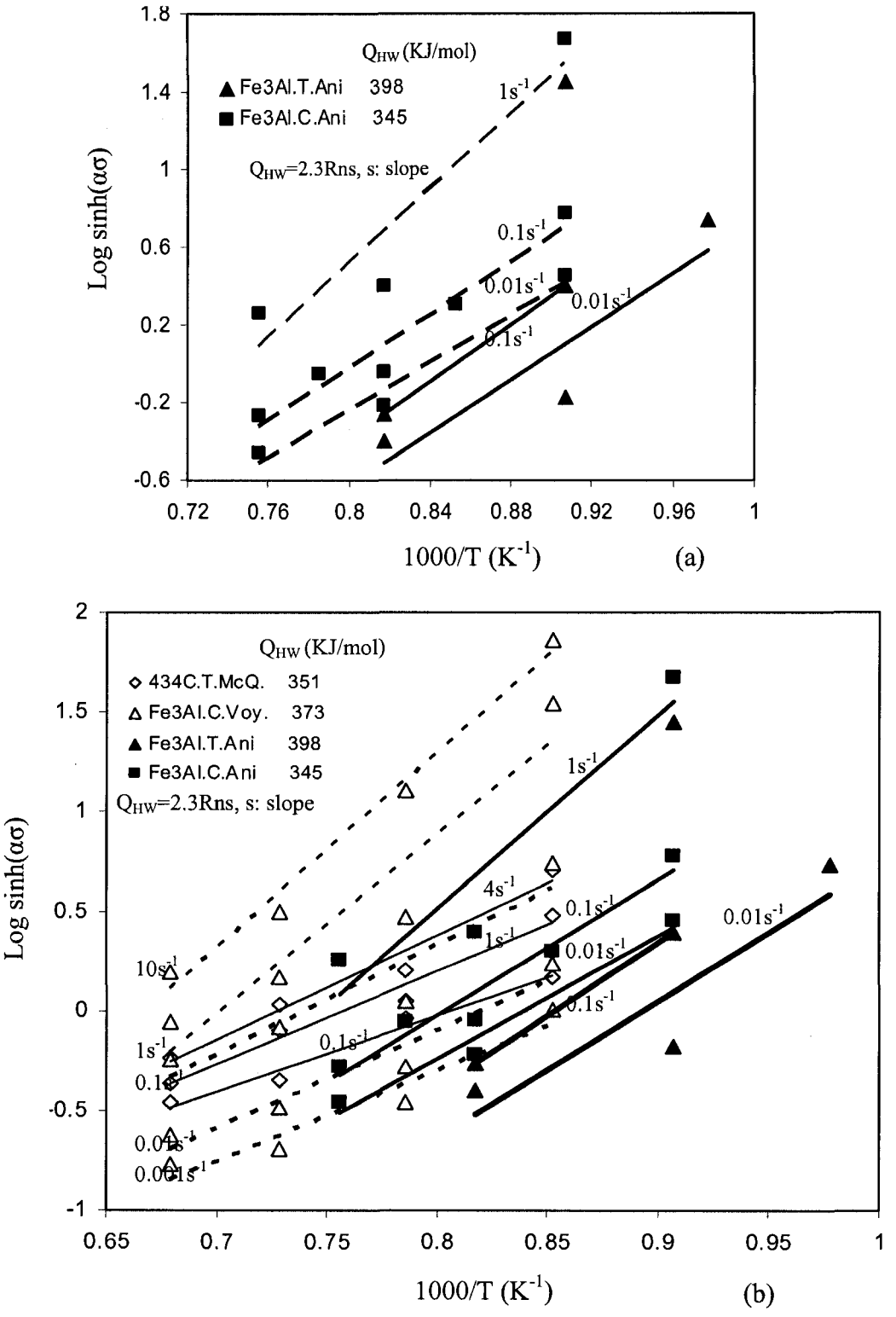

Fig. 5.4 Log (sinhασ) and 1000/T: a) present results of Fe_3Al.

b).various sources of data for Fe_3Al and 434C

Table5.1 Comparison between Fe_3Al and 434C

	Previous values			Current values		
	$\alpha(MPa^{-1})$	n_{ave}	Q_{HW} (kJ/mol)	$\alpha(MPa^{-1})$	n_{ave}	Q_{HW} (kJ/mol)
434C.T.McQ.	0.0172	3.8	397	0.017	4.0	351
Fe_3Al.C.Voy.	0.0070	3.8	352		2.9	373
Fe_3Al.T.Ani					4.2	398
Fe_3Al.C.Ani					2.4	345

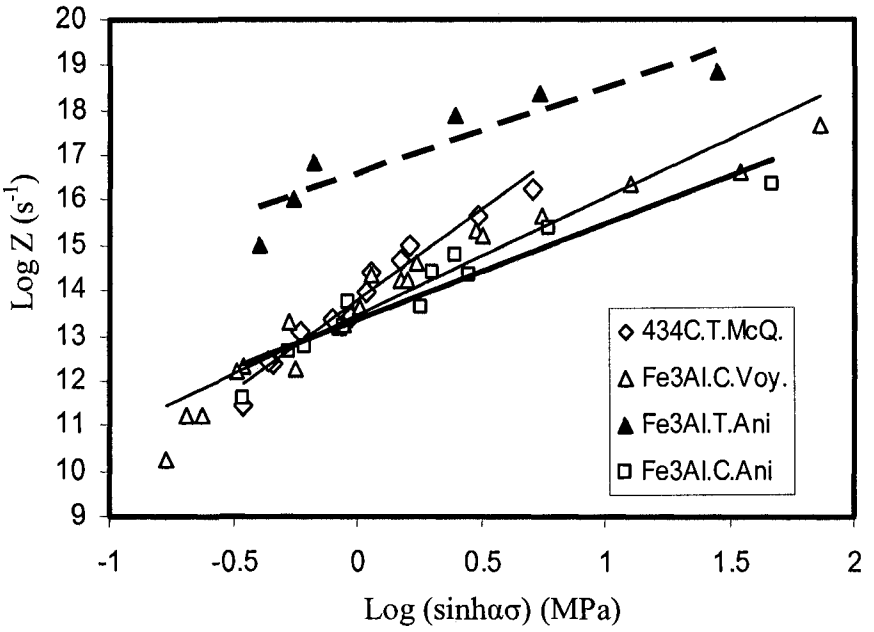

Fig. 5.5 The relationship between LogZ and Log (sinhασ) for Fe_3Al and 434C.

5.2 Fe-2.7Si-0.06C

5.2.1 Isothermal-continuous tests

5.2.1.1 Microstructure analysis

The relationship between subgrain size and flow stress at high T determined by Uvira [60] was shown in Figure 2.42. The current limited data are compared to published data. In Table 5.2, the subgrain size 2.9μm, $\sigma = 198MPa$ for 700°C/1s^{-1} (Figure 4.16) is reasonable when compared to those of Uvira [60] for Fe-2.8Si-0.03C-0.45Mn: 3.0μm from

optical at 650°C/0.5s^{-1}, ε=1.6; 4.0μm from TEM at 750°C/0.25s^{-1}, ε=0.4; It is also reasonable when compared to that of Kosic et al [58, 59]: 2.0μm from TEM at 600°C/1.11s^{-1}, ε=0.4. However, it is more than double values from J-P. A. Immarigeon and Jonas for Fe-2.7Si-0.03C-0.39Mn [57]: 1.26μm from optical at 675°C/0.1s^{-1}, ε=0.53; 1.48μm when ε=0.63. Moreover, compared with the creep subgrain size of Barrett et al [55] 2.0μm at 643°C/8.3×$10^{-6}s^{-1}$, $\sigma = 100MPa$, ε=0.2 as shown in Figure 2.41, this subgrain size is also reasonable. Subgrain size 10μm of some areas, $\sigma = 70MPa$ for the specimen deformed at 900°C/1s^{-1} is close to the data of Uvira at 900°C/0.24s^{-1} [60]: 6.3μm from optical or 10.0μm from TEM, ε=0.5.

5.2.1.2 Stress comparison

The peak stresses σ_P of various Fe-Si alloys and Fe-Cr alloys are compared in Figure 5.6 for increasing T at various $\dot{\varepsilon}$. For current material Fe-2.7Si-0.06C, σ_P decreases with the increase of T and the decrease of $\dot{\varepsilon}$ as shown in Figure 5.6a. At 1s^{-1}, the recalculated torsion values (Ani.AR.) agree very well with those of compression (C. Ani) but have slight variation from the original torsion curve (AR.). The curve of Uvira (Fe-2.8Si) [12] at 0.1s^{-1} that has been interpolated for tests at 0.25 and 0.075s^{-1} lies close to the AR. line at 0.1s^{-1}.

The stress values of current material are compared with Fe-3.0Si (C.Akta) [10], Fe-2.0Si (T.Calv.M.) [11] and Fe-2.8Si (C.Uvira) [12] in Figure 5.6b. Current σ_P values connect with compression ones of Fe-3.0Si (C.Akta) at 900°C regardless of slightly different Si content. Furthermore, current σ_P values and the compression values of Fe-3.0Si (C.Akta) [10] at 1s^{-1} are much higher than those of Fe-2.0Si (T.Calv.M.) [11] at 2s^{-1} partially because of the difference of Si content. At all strain rates, the mean flow stresses (MFS) of Fe-

Table 5.2 Subgrain size of Fe-Si alloys from different sources [60, 63, 64, 65, 66] compared with current data

Authors	Material	Deformation	T (°C)	ε	$\dot{\varepsilon}$ (s^{-1})	Method to get d	Subgrain size d	Ref.
Uvira, Jonas	Fe-2.8Si-0.03C-0.45Mn	Com.	650	1.6	0.5	TEM	2.2	60
						Optical	3.0	
			750	0.4	0.25	TEM	4.0	
			800	0.4	0.15	TEM	4.2	
						Optical	5.6	
			900	0.5	0.24	TEM	6.3	
						Optical	10.0	
			1000	0.1	0.15	TEM	8.7	
						Optical	15.3	
Kosic, Abson, Jonas	Fe-2.8Si	Com.	600	0.4	1.11	TEM	2.0	58, 59
			850	0.2	3.7×10^{-3}	Optical	4.8	
				0.15	7.4×10^{-5}	Optical	10.2	
Barrett, Nix, Sherby	Fe-3Si	Creep	643	0.2	8.3×10^{-6}	TEM	2.0, 18.0	55
J-P.A.Immarigeon, Jonas	Fe-2.7Si-0.03C-0.39Mn	Com.	675	0.53	0.1	Optical	1.26	57
				0.63			1.48	
Ani .AR	Fe-2.7Si-0.06C	Tor.	600	1.5	1	Optical	581(Grain)	
			700	5.5			2.9	
			800	3.5			725(Grain)	
			900	14.3			10, 29, 60	

Com.: Compression; Tor.: Torsion.

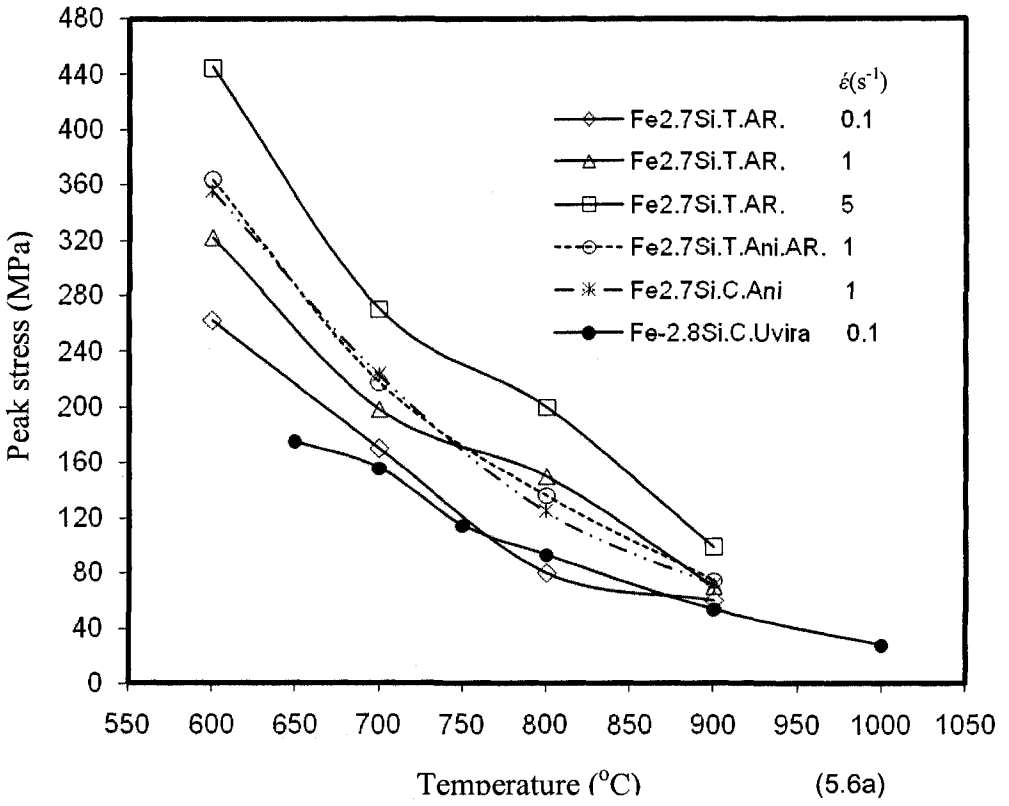

Fig. 5.6 Comparison of stress: a) σ_P of current material; b) between Fe-Si alloys within 600~1100°C; c) between Fe-Si alloys within 800~1100°C; d) between Fe-Si alloys, 409C and 434C.

2.0Si (T.Calv.M.) [11] are always much lower than the σ_P values of Fe-2.7Si (T.AR.) and Fe-3.0Si (C.Akta) [10], at the same T and $\dot{\varepsilon}$ partially because MFS is always less than σ_P. Figure 5.6c demonstrates the relatively good agreement of stress dependence on T for all Fe-Si alloys.

Fe-Si alloys have the same BCC crystal structure as many Fe-Cr alloys, so they are compared with 434C (Fe- 16.55Cr-0.96Mo-0.21Ni) [6] and 409C (Fe-11.0Cr-0.01Mo-0.16Ni-0.19Ti) [13]. 409C with 11% Cr and low content of Mo has lower σ_P values than

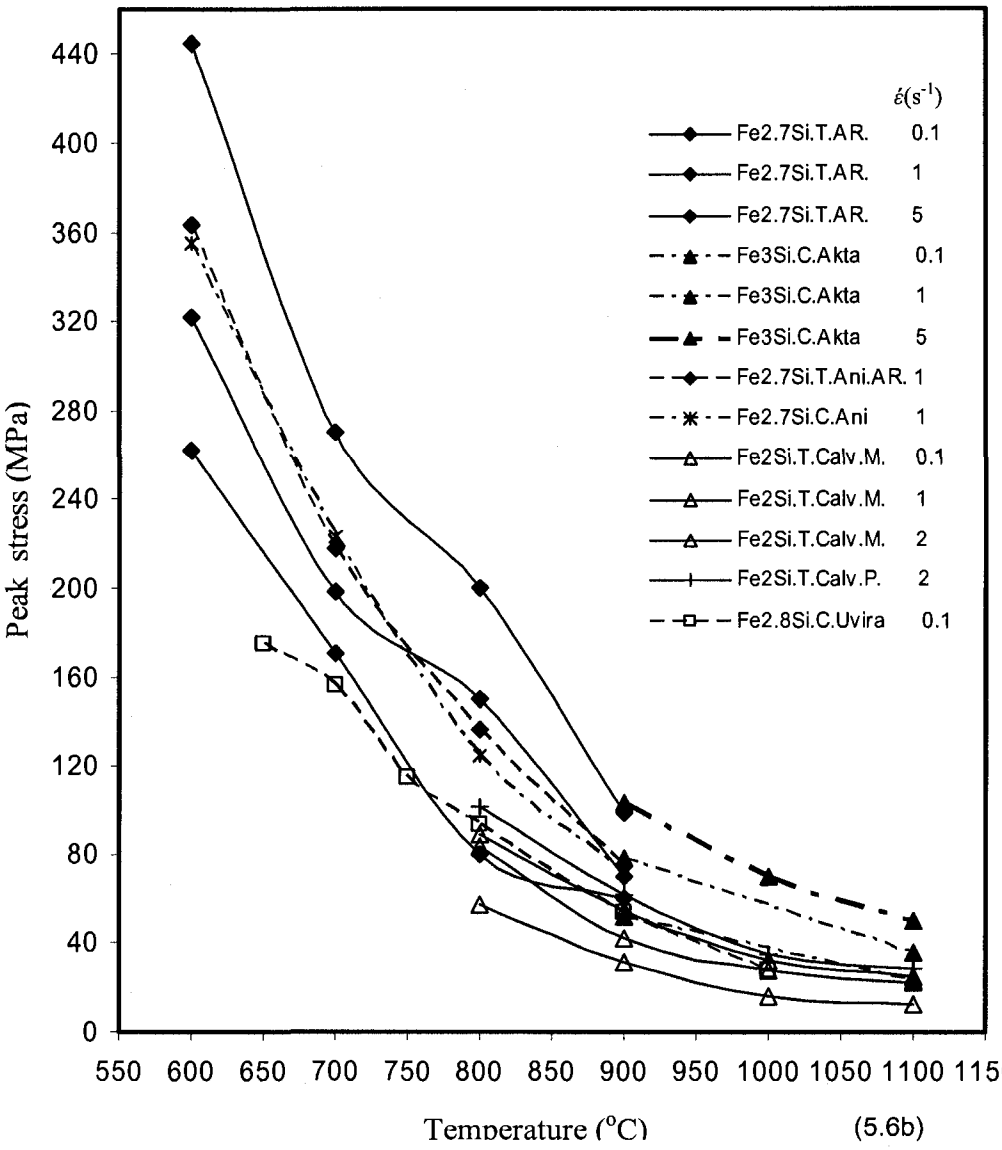

(5.6b)

those of Fe-2.7Si (T.AR.) and Fe-3.0Si (C. Akta) and at $1s^{-1}$ close to those at $2s^{-1}$ for Fe-2Si (T.Calv.M.) Moreover, the σ_p curve of Fe-2.0Si at $2s^{-1}$ (T.Calv.P.) lies between the lines of 1 and $4s^{-1}$ but closer to the curve $1s^{-1}$ of 409C. This roughly indicates that ~12% Cr has about the same effect as ~3% of Si. 434C with 16.6% Cr and more important 1% Mo

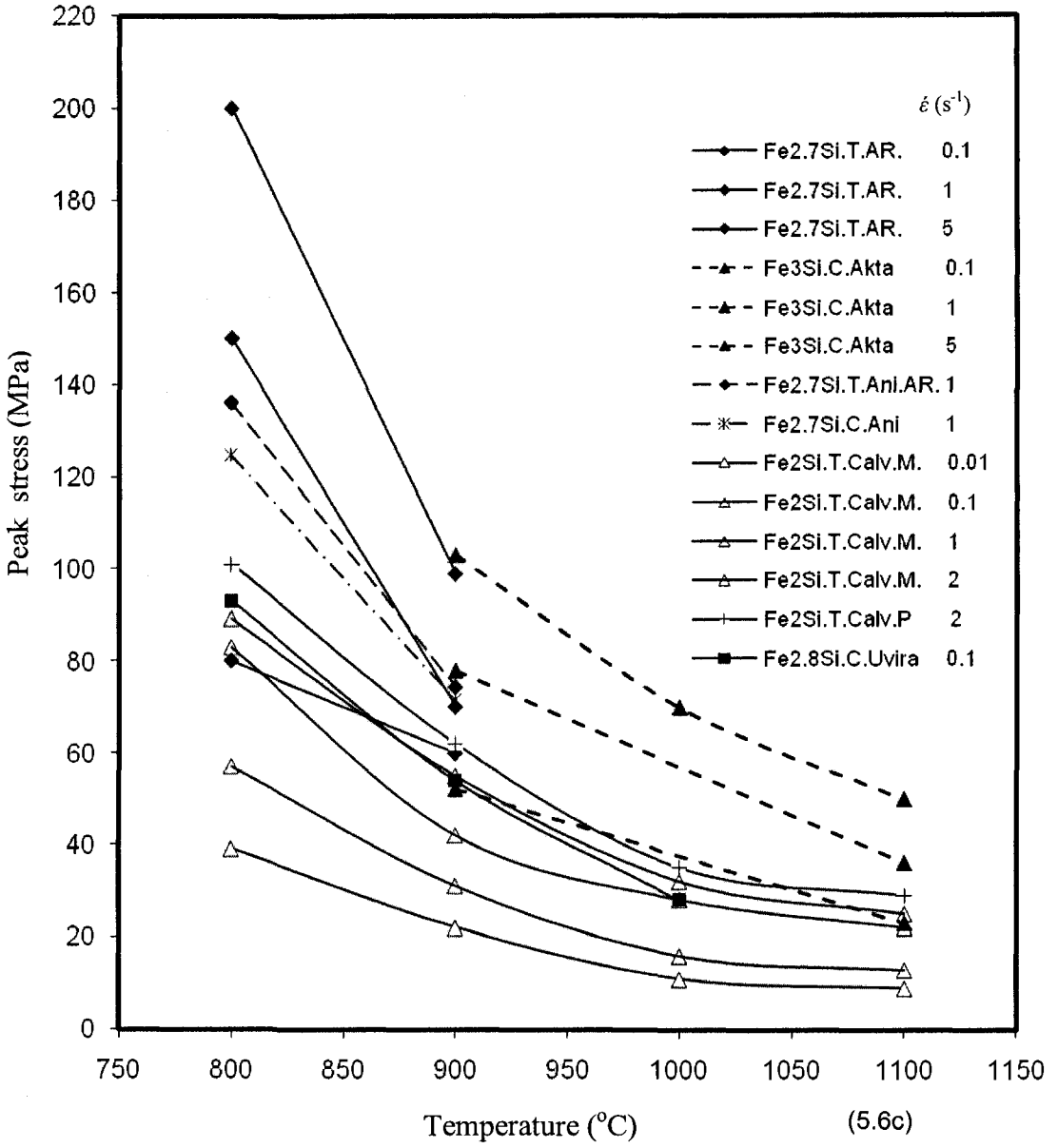

(5.6c)

is the strongest among all alloys. Although Cr is a powerful ferritizer, it has low interaction with dislocations but Mo has strong interaction with dislocations and hence considerable strengthening of the matrix.

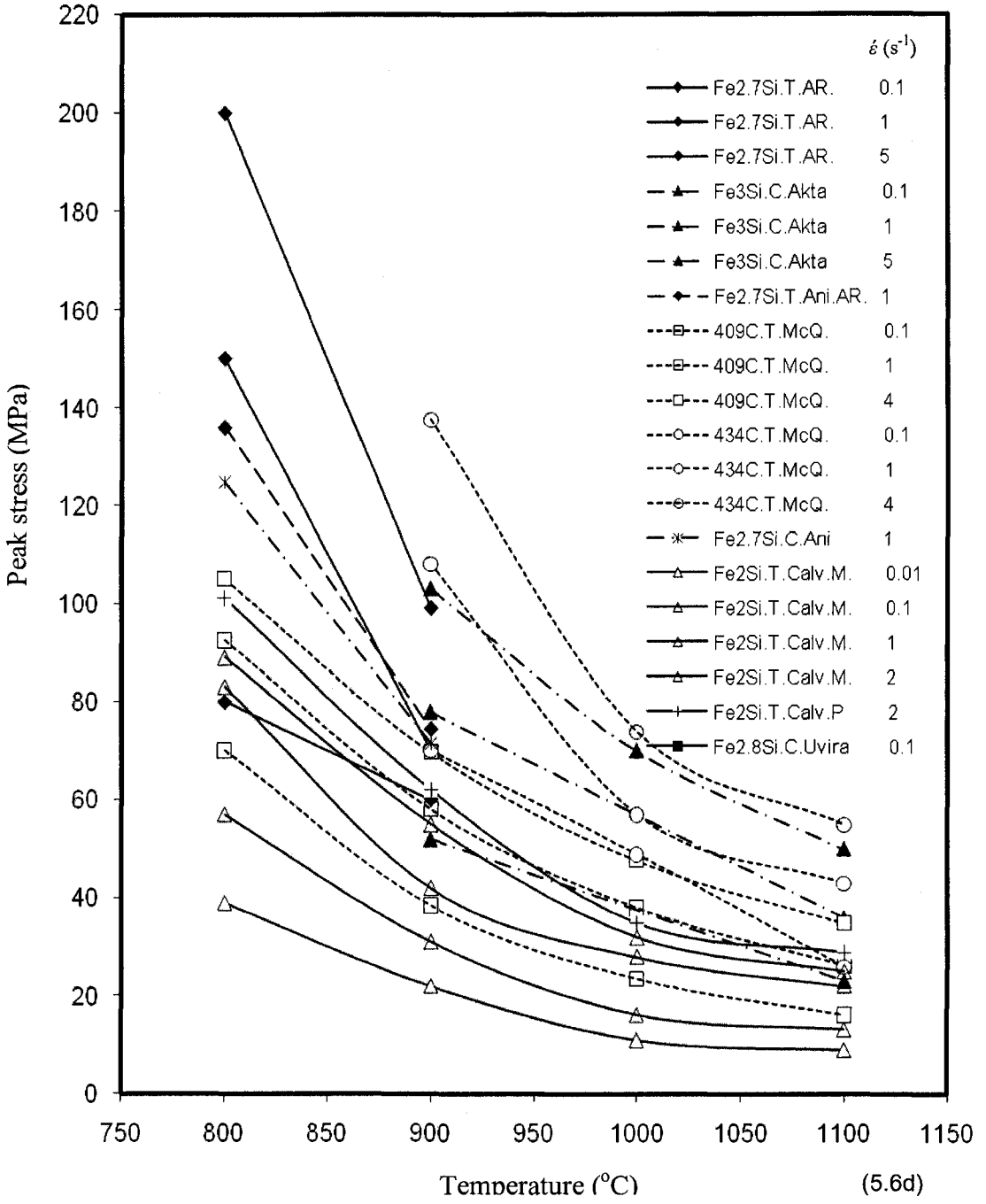
Peak stress (MPa)
Temperature (°C)
ε̇ (s⁻¹)
Fe2.7Si.T.AR. 0.1
Fe2.7Si.T.AR. 1
Fe2.7Si.T.AR. 5
Fe3Si.C.Akta 0.1
Fe3Si.C.Akta 1
Fe3Si.C.Akta 5
Fe2.7Si.T.Ani.AR. 1
409C.T.McQ. 0.1
409C.T.McQ. 1
409C.T.McQ. 4
434C.T.McQ. 0.1
434C.T.McQ. 1
434C.T.McQ. 4
Fe2.7Si.C.Ani 1
Fe2Si.T.Calv.M. 0.01
Fe2Si.T.Calv.M. 0.1
Fe2Si.T.Calv.M. 1
Fe2Si.T.Calv.M. 2
Fe2Si.T.Calv.P 2
Fe2.8Si.C.Uvira 0.1

(5.6d)

5.2.1.3 Constitutive analysis

Figure 5.7 shows the relationship between Log ε̇ and Log (sinh ασ) of Fe-Si and Fe-Cr alloys. It can be seen that the values of σ_P (MFS for Fe-2.0Si, Calvillo) increase with the increase of ε̇ and decrease of T, which agrees with Figure 5.6a and 5.6b. All the lines for one material are almost parallel, and the value of n is taken as the average of the slopes. In Figure 5.7a for the comparation between Fe-Si alloys, the line at 900°C for Fe-2.7Si (T.AR.) superimposes with the 900°C line of Fe-3.0Si (C.Akta). For Fe-2.8Si (C.Uvira), the points lie reasonably close to those of Fe-2.7Si and Fe-3.0Si under similar conditions. For Fe-2.0Si (T.Calv.M.), the MFS lines are always located at lower stress

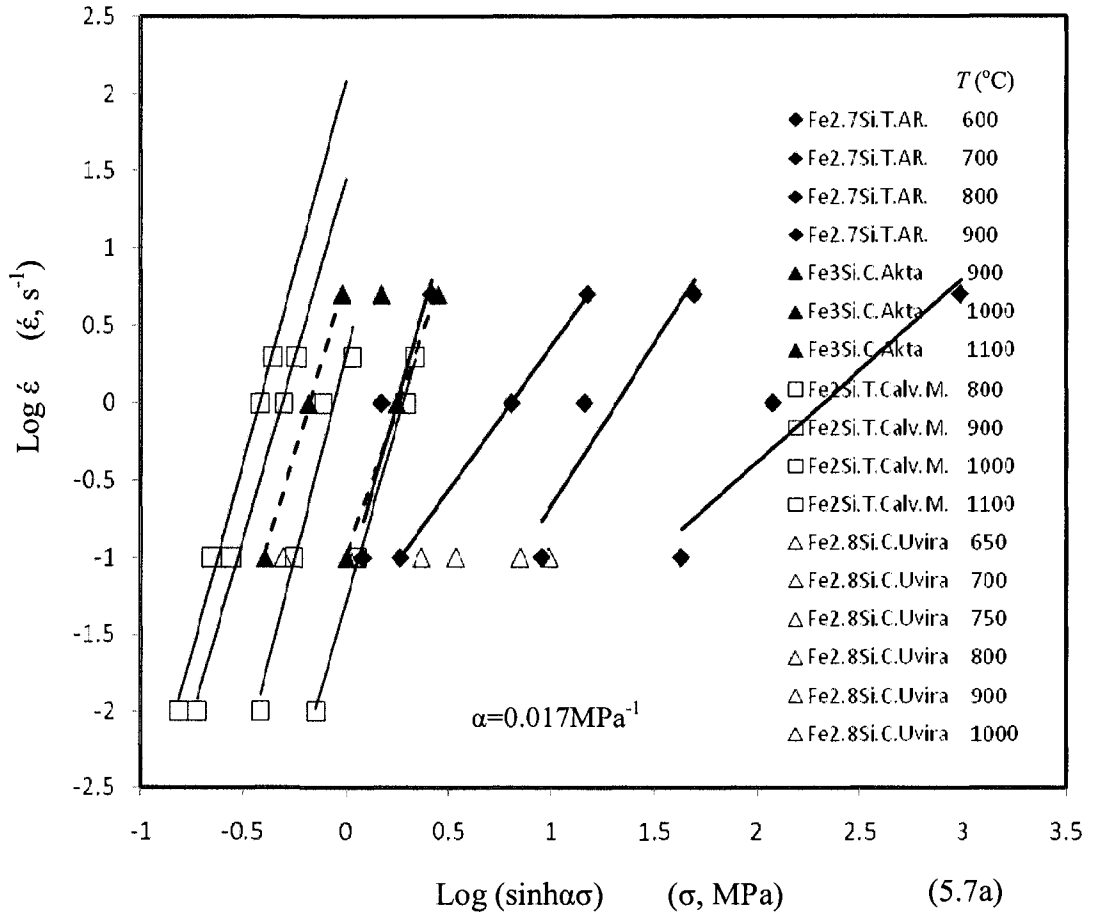

(5.7a)

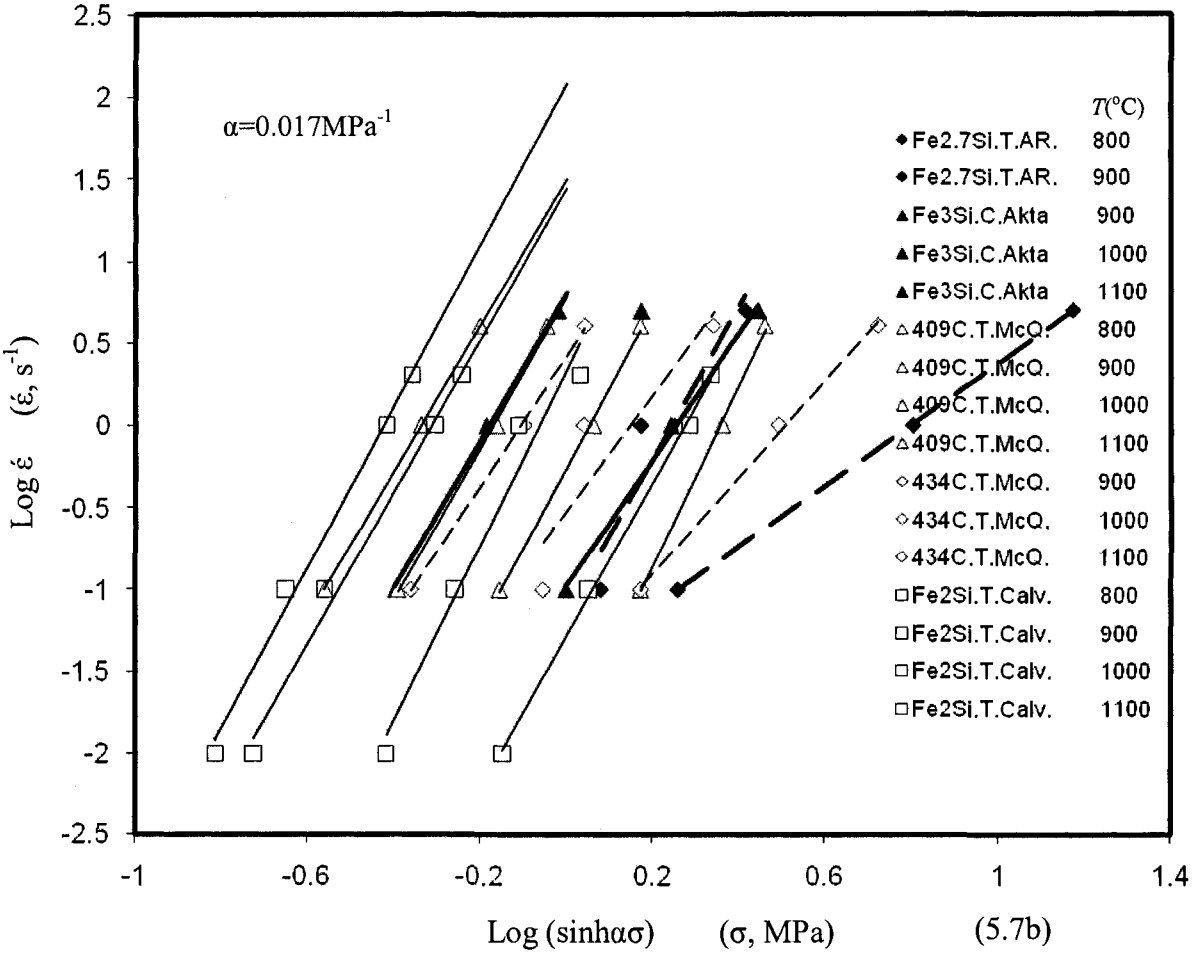

Fig. 5.7 Log ε versus Log (sinhασ) comparison between: a) Fe-Si alloys; b) Fe-Si alloys, 409C and 434C. For each material, lines are closer to right for lower temperature.

than other materials under the same conditions, which agrees with Figure 5.6. In Figure 5.7b, at the same ε, 434C is always located at the highest σ_p values among all materials mainly because of its 1% of Mo and 16%Cr; 409C with only 11%Cr is always located at lower stress than those of Fe-2.7Si (T.AR.), Fe-3.0Si (C.Akta) and 434C but higher than Fe-2.0Si (T.Calv.M.), which agrees with Figure 5.7d.

Comparison of the relationship between Log (sinh ασ) and 1000/T for Fe-Si and Fe-Cr alloys is shown in Figure 5.8. In Figure 5.8a covering all the results of Fe-Si alloys,

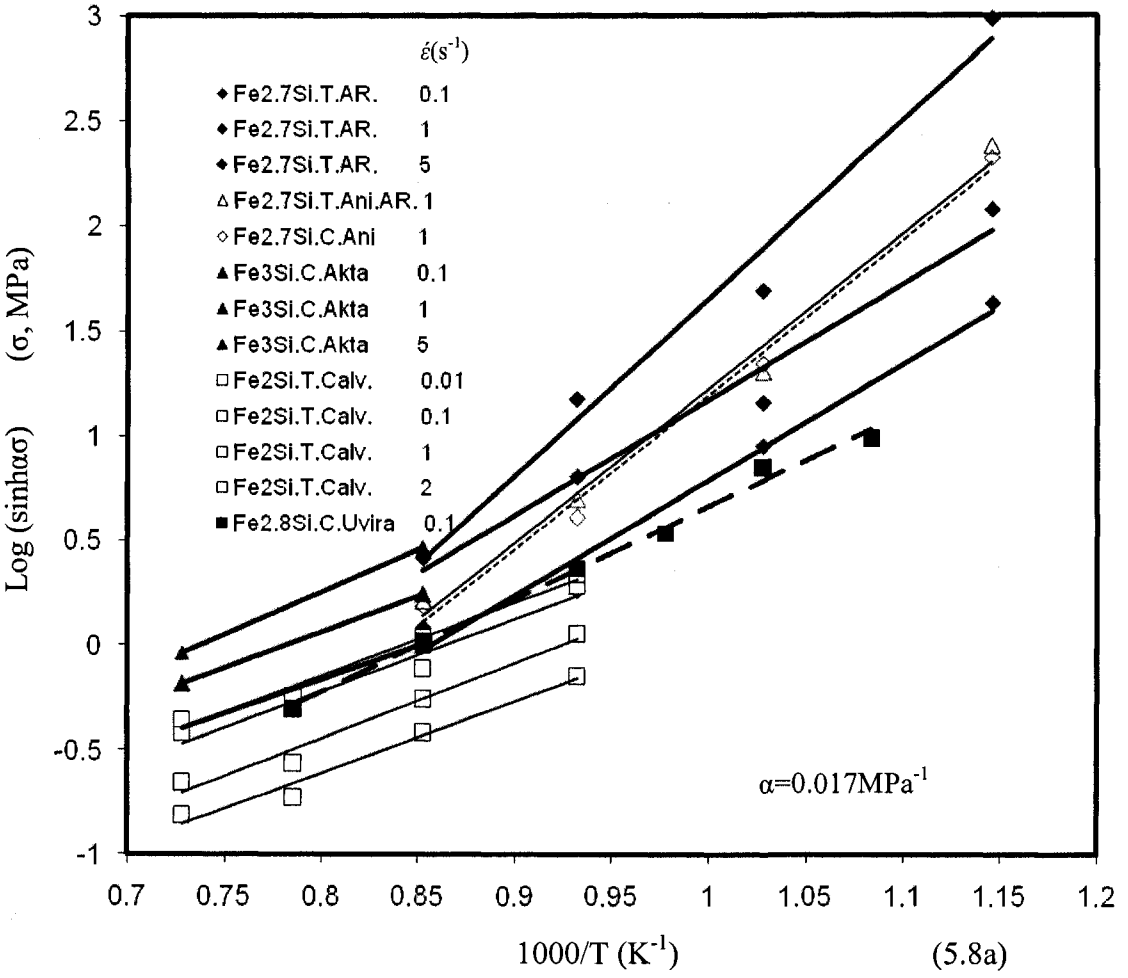

Fig. 5.8 Log (sinhασ) and 1000/T: a) Comparison between Fe-Si alloys; b) between Fe-Si alloys, 409C and 434C within 600~1100°C; c) between Fe-Si alloys, 409C and 434C within 800~1100°C. For each material, lines are closer to bottom for lower strain rate.

the lines for Fe-2.7Si (T.AR.) connect with those of Fe-3.0Si (C.Akta) at 900°C as in Figure 5.6b. The recalculated data line at $1s^{-1}$ (T.Ani.AR.) and the compression line (C.Ani) are very close to each other, and they connect with the points of Fe-3.0Si (C.Akta) at 900°C. Figure 5.8b includes all the data of Fe-Si and Fe-Cr alloys, and Figure 5.8c compares their stress variation with T within 800~1100°C. At the same T, 434C with 16.6Cr-1Mo

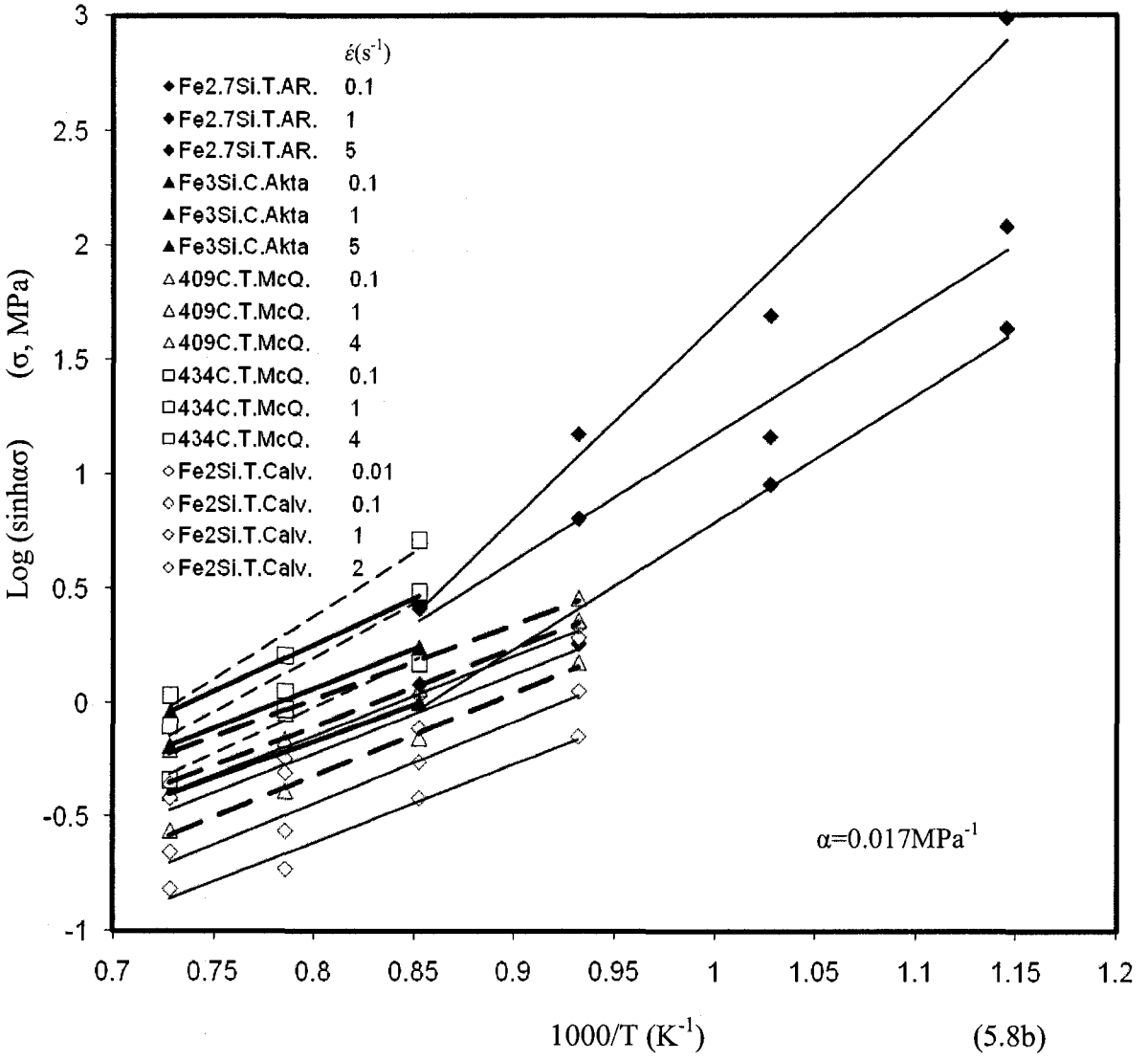

(5.8b)

always has the highest stress values among all the materials, followed by those of Fe-3.0Si (C.Akta), 409C and Fe-2.0Si (T.Calv.M.) in order, which agrees with Figure 5.6d. For each material, the slope value is taken as the average of all slopes for the material, then activation energy Q_{HW} values are calculated and listed in Table 5.3. They are all close to that of pure iron, 280kJ/mol.

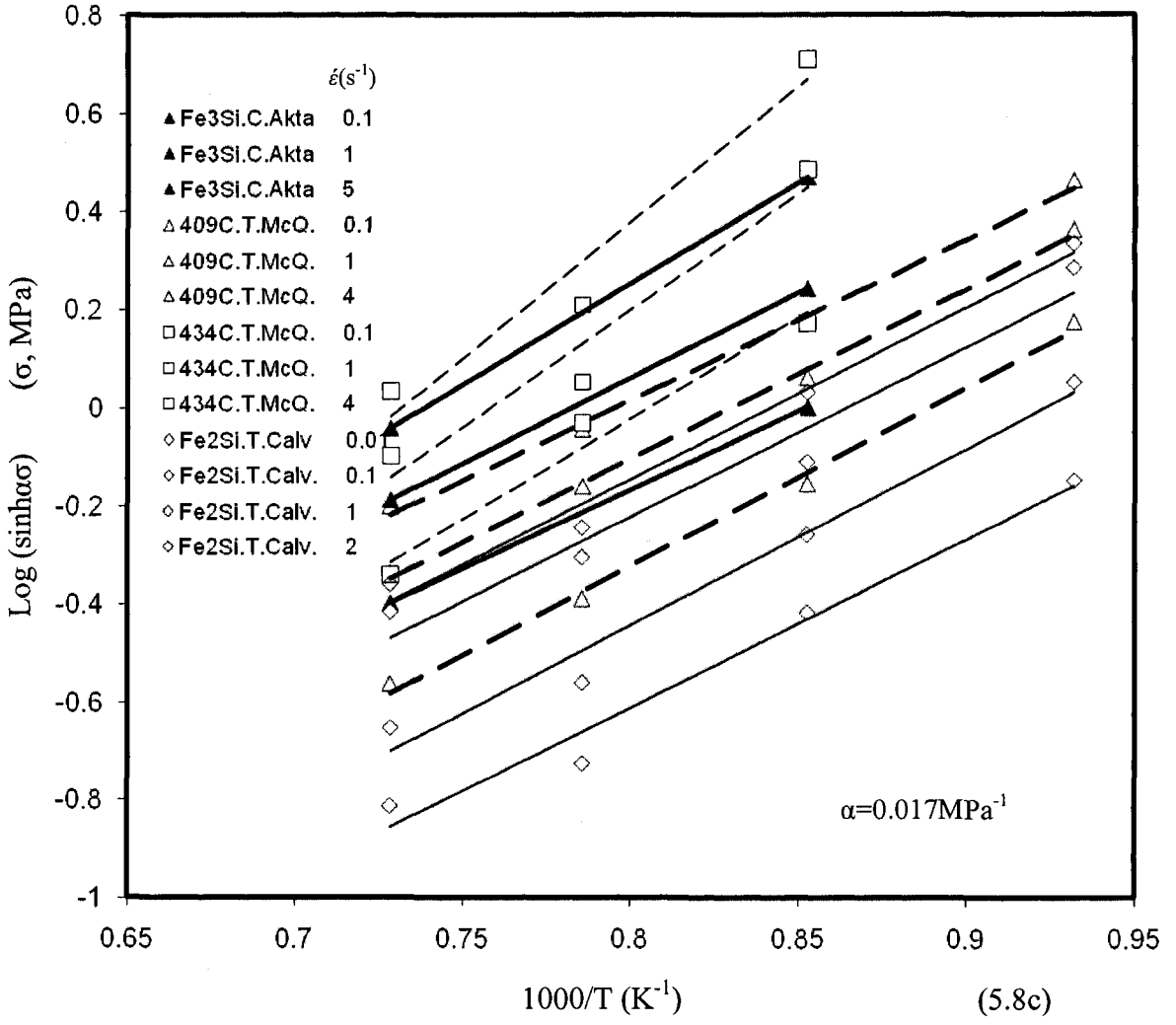

Figure 5.9 compares the relationship between Log Z and Log (sinh ασ) for Fe-Si alloys, 409C and 434C. The Q_{HW} value has major influence on the position of the lines, moving them downward in the decreasing order of Q_{HW} values: 434C, 409C, Fe-3.0Si, Fe-2.0Si and Fe-2.7Si. The lines for Fe-3.0Si and Fe-2.0Si superimpose because the higher Q_{HW} value of Fe-3.0Si moves its line upward but the higher stress values moves the line rightward toward the Fe-2.0Si line. Fe-2.7Si line lies at the right side because of its very high σ_P values due to the very low T range.

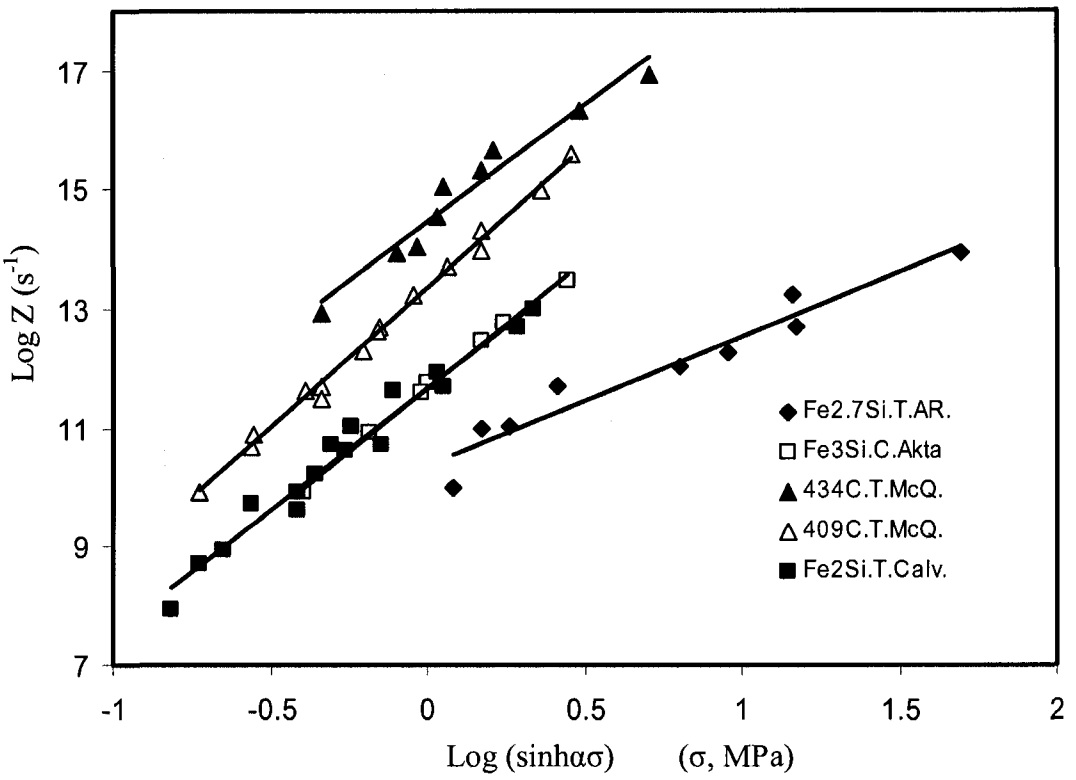

Fig. 5.9 The relationship between LogZ and Log (sinhασ) for Fe-2.7Si [9], Fe-3.0Si [10], Fe-2.0Si [11], 409C [13] and 434C [6].

Table 5.3 α, n and Q_{HW} values for Fe-Si and Fe-Cr alloys [9, 10, 11, 12, 13]

Material (wt%)	α (MPa^{-1})	n	Q_{HW} (kJ/mol)	Reference
Fe-2.7Si-0.06C	0.017	2.0	247	Current
	0.0166	1.1	178	9
Fe-3.0Si-0.036C-0.089Mn	0.017	4.2	287	10(Recal.)
Fe-2.0Si-0.003C-0.02Mn	0.017	3.9	261	11(Recal.)
	0.0129	4.6	299	11
Fe- 16.55Cr-0.96Mo-0.21Ni (434C)	0.017	4.0	367	6(Recal.)
	0.0172	3.8	397	6
Fe-11.0Cr-0.01Mo-0.16Ni-0.19Ti (409C)	0.017	4.9	320	13(Recal.)
	0.0254	4.3	270	13
Fe			280	40

5.2.2 Multi-stage tests

Multi-stage tests with Fe-2.7Si-0.03C were carried out with different pass strains ε_i, pass intervals between two neighboring passes t_i, strain rate $\dot{\varepsilon}$=1s^{-1} for all schedules. Deformation temperature T_i declines from 900 to 600°C in most of the schedules but from 1000 to 700°C in one schedule.

The micrographs show that the subgrains are larger when the T_i range is raised (Figure 4. 26 and 4.29) and the grains are more elongated when the total strain is larger (Figure 4.25 -- 4.28). Table 5.4 developed from Figure 2.34 [54] provides some explanation. With the increase of T_i, ε_i and t_i, the fraction of SRX increases. Accordingly, if relative softening RS were calculated, it would have increased with the increase of T_i, ε_i and t_i. Moreover, from this table, the temperature below which SRX stops and only SRV occurs during the intervals becomes lower with the increase of ε_i and t_i; this T is defined as T_{SRV}. For schedule with $\varepsilon_i = 0.2$, $t_i = 20$ s, T_{SRV} is about 900°C; for the two schedules with $\varepsilon_i = 0.2$, $t_i = 40$ s and $\varepsilon_i = 0.3$, $t_i = 40$ s the values of T_{SRV} are about 750°C, the one with $\varepsilon_i = 0.4$, $t_i = 40$ s about 700°C.

For current material, the variation of RS_i with T_i, ε_i and t_i when $\dot{\varepsilon}$=1s^{-1} is shown in Table 5.5. The decrease of T_i leads to a decrease of RS_i, which agrees with results of Table 5.4. In the 900~600°C schedules, the increase of ε_i and t_i causes a decrease of RS_i; such behavior is contradictory to the results in Table 5.4. Noticeably, RS_i values for the schedule with $\varepsilon_i = 0.4$, $t_i = 40$ s are much lower than those of other ones, so as stated in section 4.2.2.2, this may be due to error in programming and should be omitted

Table 5.4 The fraction of SRX with deformation and holding T as well as holding time [54]

Fe-3.2Si-0.11Mn-0.03C (wt%)										Al [53]
	ε =0.2				ε =0.3	ε =0.4				ε =0.46
T (°C)	10s	20s	40s	100s	40s	10s	20s	40s	100s	Below 350 °C ($0.67T_M$), only SRV occurs, $FS_i \leq 30\%$.
910($0.67T_M$)	0	***2%***	***10%***	25%	***20%***	10%	20%	***35%***	60%	
810($0.60T_M$)	0	T_{SRV}	***2%***	5%	***5%***	T_S	5%	***10%***	15%	
750($0.55T_M$)	0	0	T_{SRV}	T_{SRV}	T_{SRV}	0	T_{SRV}	***2%***	5%	
710	0	0	0	0	0	0	0	T_{SRV}	T_{SRV}	

Table 5.5 The variation of RS_i* with finishing temperature of each pass T_i, ε_i and t_i when $\dot{\varepsilon}$=1s^{-1}

900~600(°C)					1000~700(°C)	
	ε =0.2		ε =0.3	ε =0.4	ε =0.2	
T_i (°C)	20s	40s	40s	40s	T_i (°C)	40s
1000					1000	33
900	***32.5***	***24.5***	***25.7***	***15***	900	31
800	26	***22***	***20***	***12***	800	30
700	23	21	17	11	700	28
650	20	19	14	9		
600	13	17	8	6		

*: Values taken from trendline.

Table 5.6 The variation of RRS_i with finishing temperature of each pass T_i, ε_i and t_i when $\dot{\varepsilon}$=1s^{-1}

900~600(°C)					1000~700(°C)	
	ε =0.2		ε =0.3	ε =0.4	ε =0.2	
T_i (°C)	20s	40s	40s	40s	T_i (°C)	40s
1000					1000	11.3
					950	16.5
900	N/A	4.6	2.2	12.9	900	24
800	13.5	21.3	22.5	19	800	***28.7***
750	22	25.3	27	***20.2***	750	27.2
700	24.2	***26.2***	***27.9***	18.7	700	24.3
650	***26***	23.5	22.5	15.6		
600	22	16.2	15.5	12.3		

from analysis. The variation of RRS_i with finishing temperature of each pass T_i, ε_i and t_i for current material is listed in Table 5.6. In higher T_i range, the softening effect of the interpass anneal increases with the decline of T_i; σ_{mi} increases more slowly than σ_{pi} so that RRS_i value increases until a peak. In the low T_i range, σ_{pi} increases more slowly than σ_{mi} with the decline of T_i so that RRS_i value decreases.

For the specimen deformed with 1000~700°C schedule, it hardens less in a given pass but softens more quickly during the following interval because of the high thermal activation energy. Its RS_i and RRS_i values are generally higher than those deformed within 900~600°C. For 900~600°C schedules, RRS_i values rise across the schedules in the order of 0.2-20, 0.2-40 and 0.3-40 in contrast to the decrease of RS_i values. RRS_i appears to be a more reasonable parameter than RS_i.

To clarify that RS_i and RRS_i are related to the traditional FS_i, one may turn to the torsion simulation of Al that has a high tendency to SRV (resistance to SRX) as do ferritic steels. Moreover, for pure Al [53], in multi-stage declining-T_i torsion schedules, the measured FS_i has been related to microstructural development during the passes and the intervals.

In the 17-stage schedule (ε_i=0.23, t_i=94s), SRX declined from 100 to 70% between 500 ($0.83\,T_M$) and 460°C ($0.79\,T_M$) and was related to a rapid decline of RS_i from 28% to 12% (Figure 2.33). From 460 to 400°C ($0.72\,T_M$), SRX declined further reaching zero so that RS_i declined to a plateau which continued at about 10% from 400 to 300°C ($0.61\,T_M$) related to SRV declining from 35% to 22%. These 3 stages of decline

in RS_i were related respectively to a rapid rise, a slight rise and a plateau in RRS_i (Figure 2.34). While SRX at high T_i (500~460°C, 0.83~0.79 T_M) provides high FS_i and RS_i, it gives little RRS_i. In contrast, declining SRV at low T_i (400~300°C, 0.72~0.61 T_M) provides little FS_i and RS_i but high RRS_i, which is industrially significant.

For current material, the 1000~700°C schedule has high RS_i values declining from 43.5% at 1000°C (0.72 T_M) to 37.5% at 925°C (0.68 T_M) followed by a slight decrease from 30% at 900°C (0.67 T_M) to about 28% at 700°C (0.55 T_M) except for some fluctuation related to the amount of SRX as stated in section 4.2.2.2. For 900 (0.67 T_M) ~600°C (0.49 T_M) schedules, RS_i values decline slowly from about 30% to 18% for 0.2-20 schedule, from about 23% to 16% for 0.2-40 schedule, from about 23% to 11% for 0.3-40 schedule except for some fluctuation. The values calculated from the equations of their trendlines are listed in Table 5.5.

There is more work to be done: the determination of yielding stress σ_{yi} and the fraction of SRX for each pass of different schedules; the determination of T_{nr} for each schedule; the equivalent between FS_i and RS_i. However, such work would require 5 to 10 times as many torsion tests and microstructure examinations so that is beyond the possibilities of current project.

CHAPTER SIX

CONCLUSION

For all body-centered cubic ferritic iron alloys, the peak stress in the flow curves declined as temperature increased according to an Arrhenius relationship and as strain rate decreased according to a hyperbolic sine law. The strength can be correlated by the Zener-Holloman parameter Z ($Z = \dot{\varepsilon}\exp(Q_{HW}/RT) = A\sinh\alpha\sigma^n$. At high temperatures ($\geq$900°C for Fe_3Al and $\geq$800°C for Fe-2.7Si), the flow curves gradually declined towards a plateau. However, microscopy indicated that this was not due to dynamic recrystallization.

In comparison to published results on the same material from Voyzelle, Fe_3Al (Fe-15.5Al-5.8Cr-1.0Nb) in this project has lower strength in torsion and compression. The activation energy of 373 ±25 kJ/mol brackets the published value 358kJ/mol. Moreover, Fe-15.5Al-5.8Cr-1.0Nb is stronger and has higher activation energy than 434 (Fe- 16.55Cr-0.96Mo-0.21Ni) stainless steel that is generally stronger than Fe-Si steels with 2 - 3% Si.

The peak stresses in torsion and compression of Fe-2.7Si steel are in good agreement with those of published results for steels with 2 - 3%Si. For Fe-2.7Si, peak stresses of torsion agree very well with those of compression at $1s^{-1}$. All the Fe-Si steels are generally similar in strength to 409 (Fe-11.0Cr-0.16Ni-0.19Ti) but weaker than 434. The activation energy of the Fe-Si steels and 409 lie closely together but less than that of 434 and Fe_3Al.

The ductility of all the steel torsion specimens increases as deformation temperature rises and strain rate decreases reaching a true strain as high as 14.3 at 900°C/$1s^{-1}$ for Fe-

2.7Si. Optical microscopy confirms that the angle between the elongated grains and axes increases with the increase of fracture strain. Ductility of Fe_3Al was irregular because of cracks in the as-received material. With LogZ > $16s^{-1}$ ($\sigma_P > 90MPa$), brittle fracture occurs at randomly low strains because of cracks. Optical microscopy exhibited original elongated grains and many GB cracks associated with segregation. With LogZ $\leq 16s^{-1}$ ($\sigma_P \leq 40MPa$), specimens are very ductile ($\varepsilon_f > 6$); they have low random peak stress due to cracks. Ductility of compression specimens is difficult to observe because the cracks are generally closed up.

Optical microscopy revealed that in most of the high strain specimens ($\varepsilon_f > 3$) of Fe-2.7Si, the grains are clearly elongated. This is also true of the multi-stage tests for which the finishing temperatures are 600 or 700°C. In many grains, subgrains are observed with sizes reasonably consistent with published TEM results. After high-temperature isothermal tests, the subgrains are of the same scale as the grain thickness expected from the elongation and thus give an equiaxed appearance related to geometric dynamic recrystallization. It is possible that there are small SRX grains along the grain boundaries. For 17-stage tests of Fe-2.7Si, specimens show elongated grains with serrated boundaries. Some static recrystallization possibly occurred during the high temperature intervals, but such grains became elongated in the remaining process at lower temperatures.

In simulations of multi-stage rolling schedules, relative softening decreased with the decrease of pass temperature at fixed pass strain and interval. However, the decreases with increasing pass strain at fixed interval and with increasing interval at fixed pass strain are contradictory to the results generally accepted. Relative softening, being

normalized by the maximum pass stress, follows the same trend with low values as the fractional softening that is relative to the stress rise due to strain hardening. Relative reduction of stress relative to the isothermal peak stress increased to a maxima followed by a slight decrease as pass temperature declined. It is a reasonably useful parameter that shows the valuable softening in multi-stage industrial rolling.

Reference:

1. H. J. McQueen, H. Mecking, Creep and Fracture of Engineering Materials and Structures, B. Wilshier and D. R. J. Owen, eds., Pineridge Press, Swansea, UK (1984), pp 169–184
2. P. R. Swann, W. R.Duff and R. M. Fisher, Met. Trans., 3 (1972) 409
3. V. K. Sikka, B. G. Gleseke, R. H. Baldwin, Heat-Resistant Materials, Materials Park, Ohio 44073-0002, K. Natesan and D. J. Tillack eds., ASM Intl. Pub., (1991), pp 363-371
4. B. Voyzelle and J. D. Boyd, Mat. Sci. Eng., A258 (1998) 243-248
5. B. Voyzelle and J. D. Boyd, Metal Weld. Appl., J. P. Boillot, M. Evrard, A. Galibois and M. R. Krishnadev, eds., Met Soc, CIM Montreal (1999) pp 491-503
6. H. J. McQueen and N. D. Ryan, Mat. Sci. Eng. A322 (2002) 43-63
7. J. H. Yu, J, S. Shin, J. S. Bae, Z.-H. Lee, T. D. Lee, H. M. Lee, E. J. Lavernia, Mat. Sci. Eng. A 307 (2001) 29-34
8. J, S. Shin, J. S. Bae, H. J. Kim, H. M. Lee, T. D. Lee, E. J. Lavernia, Z.-H. Lee, Mat. Sci. Eng. A 407 (2005) 282-290
9. M. Abdel-Rahman and H. J. McQueen, Metal Weld. Appl., Evrard, A. Galibois and M. R. Krishnadev, eds., Met Soc, CIM Montreal (1999) pp 505- 516
10. S. Akta, G. J. Richardson and C. M. Sellars, ISIJ Int., 45 (2005) 1665-1675
11. P. R. Calvillo, R. Colas and Y. Houbaert, Adv. Mat. Res., 15-27 (2007) 708-713
12. J. L. Uvira and J. J. Jonas, Trans. Met. Soc. AIME, 242 (1968), 1619-1626

13. H. J. McQueen, N. D. Ryan, E. Evaangelista and X. Xia, 34th Mechanical working & Steel Processing Conference (Oct., 1992, Montreal), Iron and Steel Soc., AIME Warrendale, PA, 30 (1993), pp 101-107

14. H. J. McQueen, Metalurgia Odlewnictwo, 5 [3] (1979) 421-451

15. H. J. McQueen, J. Mat. Proc. Tech., 37 (1993) 3-36

16. R. E. Reed-Hill, Phys. Metall. Prin., D. Van Nostrand Company, pub. (1973), pp 282-294

17. M. E. Kassner and S. R. Barrabes, Mat. Sci. Eng. A 410-411 (2005) 152-155

18. A. J. Bradley and A. H. Jay, Proc. R. SOC. Lond. A136 (1932) 210

19. M. Hansen and K. Anderko, Constitution of Binary Alloys, McGraw-Hill, New York (1958), pp 90, 118

20. R.W.Cahn, Nickel and Iron Aluminides: Processing, Properties, and Applications, S. C. Deevi, P. J. Maziasz, V. K. Sikka, R. W. Chan, eds., ASM Intl., Materials Park, OH (1996), pp 3-20

21. R. A. Varin, Encylopedia of Materials: Sci. Tech., K. H. Jurgen Buschow, R. W. Cahn, N. C. Flemings, B. Ilschner, E. J. Kramer, S. Mahajan, eds., Elsevier Science Ltd. (2001), pp 4177-4181

22. S. P. Chakraborty, I. G. Sharma, A. K. Suri and D. K. Bose, Mat. Proc. Tech. 115 (2001) 413-422

23. D. H. Sasry and R. S. Sundar, Nickel and Iron Aluminides: Processing, Properties, and Applications, S. C. Deevi, P. J. Maziasz, V. K. Sikka, R. W. Chan, eds., ASM Intl., Materials Park, OH (1996), pp 123-144

24. H. J. McQueen and G. C. Kuczynski, Trans. Met. Soc. AIME, 215 (1959) 619-622

25. N. S. Stoloff and D. A. Alven, Nickel and Iron Aluminides: Processing, Properties, and Applications, S. C. Deevi, P. j. Maziasz, V. K. Sikka, R. W. Chan, eds., ASM Intl. (1996), pp 65-72

26. Sun Chao and Guo Jianting, Acta. Metall. Sinica, 28A, 11 (1992) 481

27. Zhang Zhonghua, Sun Yangshan and Guo Jun, Scripta Metall. et Mater., 33, 12 (1995) 2013-2017

28. C. G. McKamey, J. H. DeVan, P. F. Tortorellie and V. K. Sikka, J. Mater. Res. 6 (1991) 1779-1805

29. C. G. McKamey, P. J. Maziasz and J. W. Jonas, J. Mate. Res. 7(1992) 2089-2106

30. R. G. Davies, Trans. Met. Soc. TMS-AIME, 1, 227 (1963) 22-25

31. G. Ludkovski and P. D. Southwick, Metal. Trans. A, 17A (1986) 1267

32. W. C. Leslie, R. L. Rickett, C. P. Strobel and G. Knoval, Trans. ASM, 53 (1961) 715

33. C. Rossard and P. Blain, Publication IRSID-Serie A, 174, Institute de Recherches de la Sidérurgie Française, Saint-Germain-en-Laye, S & O, France, 1957

34. R. G. Stang, W. D. Nix and C. R. Barrett, Metall. Trans., 4 (1973)

35. J. L. Lytton: PhD Dissertation, Stanford University, 1962

36. C. R. Barrett, Trans. TMS-AIME, 239 (1967) 1726

37. R. G. Davies, Trans. TMS-AIME, 227 (1963) 665-668

38. S. F. Medina and C. A. Hernandez, Acta Mater., 44 (1996) 137-148

39. S. Karashima, H. Oikawa and T. Watanabe, Trans. TMS-AIME, 242 (1968) 1703-1708

40. G. Glover and C. M. Sellars, Met. Trans., 4A (1973) 765-775

41. T. Matuszewski, P. M. Machmeier and H. J. McQueen, Metall. Mat. Trans., 25A (1994) 827-837

42. J. Sankar, D. Hawkins and H. J. McQueen, Metall. Tech., 6 (1979) 325-331

43. N. D. Ryan, C. Imbert and H. J. McQueen, Strip Casting, Hot and Cold Working of Stainless Steel, N. D. Ryan et al. eds., Met. Soc. CIMM Pub., Montreal, 1993, pp 165-180

44. R. G. Zaripova, O. A. Kaibyshev and G. A. Salischev, Phys. Met. Metallog., 73 (1992) 415-421

45. N. D. Ryan, H. J. McQueen, Canad. Metall. Q., 30 (1991) 113-124

46. N. D. Ryan, E. Evangelista and H. J. McQueen, (Recrystallization '92, M. Fuentes, J. Gil Sevillano, eds., TransTech Pub., Switzerland) Mat. Sci. Forum, 113-115, (1993) 515-520

47. H. J. McQueen, N. D. Ryan and E. Fry, Mathematical Modelling of Hot Rolling of Steel, S. Yue ed., Met. Soc. CIM, Montreal (1990), pp 269-280

48. N. D. Ryan and H. J. McQueen, J. Mat. Proc. Tech., (1991) 1-22

49. N. D. Ryan and H. J. McQueen, Mat. Sci. Tech., 7 (1991) 818-826

50. N. D. Ryan and H. J. McQueen, High Temp. Tech., 8 (1990) 185-199

51. N. D. Ryan and H. J. McQueen, Mat. Forum, 14(1990) 283-295

52. I. Poschmann and H. J. McQueen, Phys. Stat. Sol. (a) 149 (1995) 341

53. I. Poschmann and H. J. McQueen, Z. Metallkd. 87 (1996) 5, 349-356

54. A. T. English and W. A. Backofen, Trans. TMS-AIME, 230 (1964) 396-406

55. C. R. Barrett, W. D. Nix and O. D. Sherby, Trans. ASM 59 (1966) 3-15

56. C. Rossard, Metaux, Corrosion, Industries, 35 (1960) 190-205

57. J-P. A. Immarigeon and J. J. Jonas, Acta Metall., 19 (1971) 1053-1061

58. O. Kosic, D. J. Abson and J. J. Jonas, JISI, 209 (1971) 624-629

59. O. Kosic, Thesis of Master of Applied Science, 1970, McGill University

60. J. L.Uvira, Thesis of PhD, 1967, McGill University

61. S. Fulop, K. C. Cadien, M. J. Luton and H. J. McQueen, J. of Test Evaluation, 5 (1977) 419-426

62. Metals Handbook, Nineth Edition. Vol. 9, Metallography and Microstructure, ASM, Metals Park, Ohio 44073 Pub., (1985) pp 532, 542-544, 690-691

63. J-P. A. Immarigeon and J. J. Jonas, Acta Metall., 22 (1974) 1235-1247

64. M. D. Coward, G. J. Richardson and D. M. Sellars, Met. Tech., 4 (1977) 75-80

65. M. D. Coward, G. J. Richardson and D. M. Sellars, Met. Tech., 3 (1976) 550-555